INFLUENCE OF HEAT TREATMENT CONDITION ON THE STRESS CORROSION CRACKING PROPERTIES OF LOW PRESSURE TURBINE BLADE STEEL FV520B

Leebashen Naicker

A dissertation submitted to the Faculty of Engineering and
the Built Environment in fulfilment of the degree of
Master of Science in Engineering

Centre for Materials Engineering, University of Cape Town

July 2016

Declaration

I know the meaning of plagiarism and declare that this dissertation is my own, unaided work save for those instances where others' work has been cited and referenced. It is being submitted for the Degree of Master of Science at the University of Cape Town, South Africa. It has not been submitted before for any degree or examination in any other university.

Signed by candidate

(Signature)

Abstract

Stress corrosion cracking (SCC) is a corrosion phenomenon which continues to plague the power generating industry especially in low pressure (LP) steam turbine blades operating in the phase transition zone. An investigation has therefore been conducted to examine the effect of heat treatment condition on the microstructure, mechanical properties and SCC properties of one such LP turbine blade material, FV520B, used in the steam turbines of coal-fired power stations in South Africa. The three stage heat treatment cycle of the FV520B turbine blades consists of homogenisation at 1020°C for 30 minutes, solution treatment at 790°C for two hours and precipitation hardening at 545°C for six hours. In this study, the precipitation hardening temperature was varied in the range 430-600°C to investigate how this variation would affect the material and SCC properties. Hardness and tensile testing were performed to obtain mechanical properties while the investigative techniques used to characterise the microstructures were light microscopy, dilatometry, X-Ray Diffraction (XRD), Scanning Electron Microscopy (SEM) and Transmission Electron Microscopy (TEM). Stress corrosion susceptibility for the different heat treatment conditions was quantified using U-bend specimens while crack growth rates and threshold stress intensities for SCC (K_{ISCC}) were measured using fatigue precracked wedge open loaded (WOL) specimens. Both SCC tests were conducted in a 3.5% NaCl environment maintained at 90°C. XRD results revealed the presence of reverted austenite in the higher tempered specimens due to the precipitation hardening temperature being close to the Ac_1 temperature for the material. The presence of reverted austenite was shown to adversely affect mechanical strength and hardness which decreased with increasing precipitation hardening temperature. Light and electron microscopy (SEM and TEM) revealed the presence of Cr-rich precipitates along the prior austenite grain boundaries in all tested heat treatment conditions. The propensity, quantity and size of the Cr-rich precipitates increased as the specimen temper temperature increased. SCC susceptibility was shown to be dependent upon yield strength and decreased as precipitation hardening temperature increased with specimens in the overaged condition showing no cracking after more than 5000 hours in the test environment. WOL testing only produced cracking in the three highest strength specimens after 2000 hours. Crack growth rates and threshold stress intensities were found to be dependent on yield strength and decreased with increasing precipitation hardening temperature. Analysis of fracture surfaces revealed crack propagation along prior austenite grain boundaries in all test heat treatment conditions indicating intergranular stress corrosion cracking (IGSCC) as the dominant cracking mechanism.

Acknowledgements

I would like to gratefully thank the following people whose support and inspiration enabled me to achieve the goal of completing this research project:

My industrial sponsor, Eskom, for affording me the opportunity to conduct this research through the Eskom Power Plant Engineering Institute (EPPEI) programme.

My supervisors, Professor Robert Knutsen and Professor Bernhard Sonderegger, for their continuous guidance, support and encouragement throughout the project.

Mrs. Penny Louw, the academic and laboratory staff at the Centre for Materials Engineering (CME) at the University of Cape Town for their valuable assistance with the laboratory work.

Mr Pierre Smith, Mr Tyrone Newins and the rest of the staff at the University of Cape Town Mechanical Engineering workshop for their valued assistance in the manufacture of specimens and other equipment required during the project.

Dr. J. Westraadt and the staff at the Centre for High Resolution TEM (CHRTEM) at the Nelson Mandela Metropolitan University for their much appreciated assistance with the specimen preparation and TEM microstructural analysis.

Miranda Waldron for her assistance with the SEM imaging at the UCT Centre for Imaging Analysis.

Dr. Thorsten Becker for his input and discussions into the fracture mechanics aspects of the project.

Fellow students at the Centre for Materials Engineering (CME) at the University of Cape Town for making the experience an enjoyable and memorable one.

My family for their constant encouragement and support.

Contents

Nomenclature

a	Crack length
a_f	Final crack length
a_0	Initial crack length
ASTM	American Society for Testing and Materials
CGR	Crack growth rate
CF	Corrosion fatigue
CLL	Crack line loaded
CMOD	Crack mouth opening distance
da/dt	Crack growth rate
E	Young’s modulus
EAC	Environmentally assisted cracking
EDM	Electric discharge machining
EDS	Energy dispersive X-ray spectroscopy
EFTEM	Energy-filtered transmission electron microscopy
EPRI	Electric Power and Research Institute
FIB	Focused iron beam
FCC	Face centered cubic
K_1	Stress intensity factor for mode I loading
K_{10}	Initial stress intensity
K_{ISCC}	Threshold stress intensity for stress corrosion cracking
HAADF	High angle annular dark-field
HE	Hydrogen embrittlement
HRTEM	High resolution transmission electron microscopy
HV	Hardness value
IGSCC	Intergranular stress corrosion cracking
LEFM	Linear elastic fracture mechanics
LP	Low pressure

mm	Millimetres
M_f	Martensite finish temperature
M_s	Martensite start temperature
NaCl	Sodium chloride
N	Newton
P	Load
Pa	Pascal
PH	Precipitation hardening
SEM	Scanning electron microscope
SCC	Stress corrosion cracking
STEM	Scanning transmission electron microscopy
TEM	Transmission electron microscope
WOL	Wedge open loading
XRD	X-ray diffraction

List of Figures

List of Tables

1 Introduction

1.1 Background

Steam turbines are one of the major components in electrical power generating stations. They are responsible for converting heat into mechanical energy. Steam expands through the turbine as it cools exerting force on the turbine blades, causing the rotor to turn. The turning rotor is coupled to the generator thus converting mechanical energy to electrical energy.

During the final stages of energy extraction, which occurs in the last rows of the low pressure (LP) turbine, the steam pressure and temperature drop so that the steam becomes wet. This region, referred to as the phase transition zone (also known as the Wilson line) is where the moisture present is known to contribute to corrosion phenomena which are not applicable to other parts of the turbine (1).

Stress corrosion cracking (SCC) is one such corrosion phenomenon which continues to plague LP turbine blades and disks operating in the phase transition zone and can be defined as a cracking process caused by the conjoint action of stress and a corrodent (2). Although SCC has not been the most widely experienced form of corrosion in engineering applications, it has certain characteristics that are uniquely troublesome. Most notable among these include the frequent lack of early warning or detection by evidence of corrosion products and the fact that catastrophic failure can be the first sign of an ill-fated material/environment combination (3).

Eskom, the South African electricity utility, currently has approximately 40 gigawatts of installed electricity capacity. Approximately 90% of this installed capacity is generated by coal-fired power stations utilizing steam turbines. There have been several recorded instances of LP turbine blade failures in Eskom power plants over the years ranging in severity from minor to catastrophic. The associated costs of plant replacement, plant downtime and loss of revenue can be detrimental, not only to Eskom, but to the country as a whole due to the fact that Eskom supplies approximately 95% of South Africa’s electricity needs.

History indicates that the major causes of turbine blade failures in the Eskom fleet are as a result of either stress corrosion cracking (SCC), corrosion fatigue (CF) or fatigue (F), with 43% of the failures being corrosion related and the remainder being a combination of “true” fatigue and other failure modes such as damage by foreign objects (4). The particular failure mechanism involved would depend on a number of factors such as the material of the blades (including heat treatment), its corrosion resistance, the loads experienced and the environment in which the turbine operates. Different materials have varying susceptibility to corrosion in different environments. This is initially taken into account during the design of the turbine however changing operational conditions during the life of the turbine can lead to unanticipated issues that would require attention (1). It is, therefore, necessary to better understand corrosion-related failure mechanisms such as SCC in LP turbine blades in order to mitigate and prevent costly failures.

1.2 Research Motivation

Low pressure steam turbine blades have predominantly been constructed from 12 Cr stainless steels such as FV566. However, as turbine technology has evolved, over recent years there has been a shift towards higher alloyed materials which provide superior mechanical and corrosion properties. One of these high alloy materials is the martensitic precipitation hardened stainless steel, FV520B, with a chromium content of approximately 14%. It possesses excellent mechanical properties and its corrosion resistance is substantially better than 12 Cr stainless steels while being comparable to that of type 304 austenitic stainless steels for many environments. These attributes make FV520B a suitable material selection for LP turbine blades which operate under high fluctuating stresses in condensed steam environments.

While FV520B is widely used in many industries including the power generating and aerospace industries, the available literature on material properties has not been extensive for this material (5-9). Furthermore, there does not appear to have been much focus to date on the corrosion behaviour of FV520B especially with regards to environmentally assisted cracking (EAC). The predominance of 12 Cr stainless steel usage for LP turbine blades has led to considerable research being conducted into the mechanisms of EAC for this group of stainless steels (10-19).

Eskom's fleet of LP turbines use blades manufactured from 12 Cr stainless steels as well as FV520B. As such, the stress corrosion behaviour of these stainless steels would be of paramount interest to the utility in terms of long term turbine health as well as life management strategies. This has led Eskom to embark on research into the stress corrosion behaviour of LP turbine blade steels used in its fleet under the auspices of the Eskom Power Plant Engineering Institute (EPPEI) programme. A previous project (17) focused on stress corrosion cracking in FV566 stainless steel. It was shown that heat treatment condition played a significant role in the susceptibility of the material to SCC. This project aims to continue the research by investigating the stress corrosion behaviour of FV520B turbine blade steel with particular emphasis on the effect of heat treatment condition.

1.3 Research Objectives

The main intent of this research project is to investigate the influence of heat treatment on the microstructure, mechanical properties and stress corrosion cracking properties of FV520B turbine blade steel. As such, the specific research objectives are as follows:

- Investigate and quantify the influence of temper condition on the material microstructure through microscopy and x-ray diffraction.
- Correlate the heat treatment and microstructure with mechanical properties obtained though hardness and tensile testing.
- Investigate and quantify the influence of the heat treatment on the stress corrosion crack initiation and growth through SCC susceptibility U-bend testing.
- Investigate the relationship between stress intensity and crack growth rate for different heat treatment conditions and determine the threshold stress intensity for SCC, K_{ISCC}.
- Characterize crack morphology on SCC specimen fracture surfaces.

2 Literature Review

2.1 Introduction

The aim of this chapter is to present a concise review of the microstructural, mechanical and stress corrosion properties of stainless steels. The role of alloying elements and their influence on the microstructure and properties of stainless steels are discussed. The effect of heat treatment condition on material and corrosion behaviour is also mentioned. Stress corrosion cracking mechanisms as well as crack propagation in stainless steels are reviewed. Due to the literature in this particular field being quite extensive, a particular bias towards high-strength 12-17% Cr stainless steels has been maintained throughout this review.

2.2 An Overview of Martensitic Stainless Steels

The industrial need for corrosion resistant alloys that could be hardened through heat treatment resulted in the development of martensitic stainless steels. The elements iron, carbon, and chromium form the basic composition of martensitic stainless steels but significant amounts of various other elements are added to provide a wide range of mechanical properties. Martensitic stainless steels are designed to be fully austenitic at elevated temperatures. These steels must therefore comprise of the proper combination of elements to promote the formation of austenite at high temperatures. These austenite promoting elements, or austenite (γ) stabilizers, are carbon, nickel, manganese, nitrogen, copper and cobalt. Chromium, on the other hand, is a strong ferrite (α) stabilizer, and this limits the maximum chromium content of martensitic stainless steels to that defined by the stable austenite region on the binary Fe-Cr phase diagram, approximately 12%. The addition of austenite stabilizers such as carbon, however, expands the austenite phase field to higher chromium contents, allowing higher levels of chromium without compromising the stability of austenite at higher temperatures.

Upon rapid cooling (usually in air) of steels with less than about 0.2% C, the transformation from face centered cubic (FCC) austenite to body centered cubic (BCC) martensite takes place. To develop optimal mechanical and corrosion properties in martensitic stainless steels, complete transformation to martensite on cooling is essential. This is economically achieved by ensuring that the martensite transformation range is above room temperature. The presence of additional alloying elements, however, can affect this transformation by depressing the martensite transformation range and reducing the martensite start (M_s) and martensite finish (M_f) temperatures. If the M_f temperature is depressed to below room temperature, retained austenite may form as a result of the martensite transformation not going to completion thereby reducing the as-quenched hardness. A subsequent tempering heat treatment will soften the original martensite, making it more ductile, but also transform the retained austenite to new, more brittle, martensite, which is undesirable. A second tempering step may be needed to eliminate the brittle martensite formed from the retained austenite. It is therefore very important to design the heat treatment of martensitic stainless steels to ensure that no, or at best, minimum retained austenite is present after cooling.

2.2.1 The effect of alloying elements on the microstructure of stainless steels

Alloying elements can be divided into two groups depending on how they influence the equilibrium iron-carbon diagram. Those elements which expand the γ-field, encouraging the formation of austenite, are called γ-stabilizers. Those elements which contract the γ-field, encouraging the formation of ferrite, are called α-stabilizers. Thermodynamically, the behaviour can be described as follows (20):

$$— = \beta e^{(—)} \quad \text{i.e.} \quad — = \left(\frac{\Delta H}{RT}\right)+ \qquad \textbf{Equation-1}$$

where:

= fractional concentration of an alloying element in the α-phase,

= fractional concentration an alloying element in the γ-phase,

ΔH = enthalpy change i.e. heat absorbed per unit of solute dissolving in γ-phase minus heat absorbed per unit of solute dissolving in α-phase, ΔH=$H_\gamma - H_\alpha$, and

β is a constant.

For ferrite stabilizers $H_\alpha < H_\gamma$ therefore ΔH is positive and the γ-phase field is restricted. For austenite stabilizers $H_\gamma < H_\alpha$ therefore ΔH is negative and the γ-phase field is unlimited. ΔH will vary from element to element as can be seen in Figure 2-1 (20), illustrating the relative strengths of alloying elements in terms of ΔH.

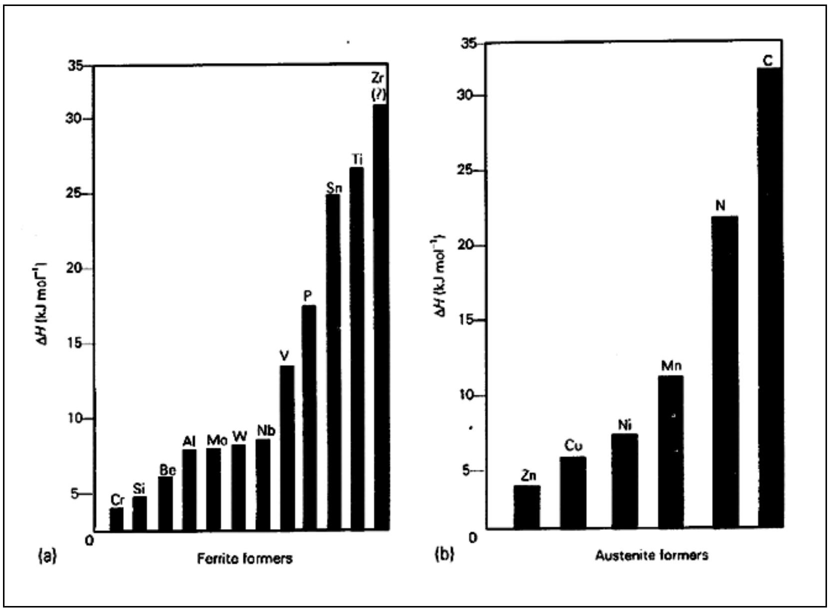

Figure 2-1: Relative strengths of alloying elements (20).

The key alloying elements of interest in FV520B are chromium, carbon, manganese, nickel, molybdenum, copper and niobium which are discussed below:

2.2.1.1 Chromium

Chromium is the primary alloying element in stainless steels. It is responsible for imparting the “stainless” property to the alloy by forming a stable, transparent, passive surface film increasing the resistance to corrosion and oxidation and is usually found in amounts greater than about 10.5% in martensitic stainless steels. It is a strong ferrite stabilizer which tends to restrict the austenite phase field and suppress the ferrite-to-austenite transformation during heating. Chromium is a carbide former and forms the hard carbides Cr_7C_3 or $Cr_{23}C_6$ which are harder than ordinary cementite. This can lead to increases in hardness and high temperature strength in the presence of sufficient carbon. Due to straight chromium steels being susceptible to temper embrittlement, steels for elevated temperature service tend to contain molybdenum to prevent this (21). This embrittlement could be as a result of the accelerated rate of grain growth caused by chromium. This effect can be retarded by the addition of other alloying elements such as vanadium, titanium, niobium and to a small extent nickel (22).

2.2.1.2 Carbon

The addition of carbon to iron constitutes steel. This addition, even in small amounts e.g. 0.1-0.2 wt%, is enough to increase the strength of iron substantially. The atomic size of carbon is sufficiently small relative to that of iron and other metallic alloying elements to allow the carbon elements to enter the iron lattice as interstitial solute atoms where they occupy the octahedral interstices which are more favourably placed for the relief of strain (20). In addition to this, the solubility of carbon in austenite is greater than in ferrite due to the larger interstitial sites available, rising as high as 9-10 at%, which is fully exploited in the heat treatment of steels to increase strength. From Figure 2-1, it can be seen that carbon is a strong austenite stabilizer, promoting the formation of austenite at higher temperatures thereby enabling the increase in chromium content in martensitic stainless steels above the thermodynamically stable limit in the binary Fe-Cr phase diagram. Carbon also plays a role in the high hardness of martensite. An increase in carbon content increases the hardness of martensite in iron-carbon alloys as can be seen in Figure 2-2 (20). It can also be seen in Figure 2-2 that carbon content does not have the same effect on the hardness of austenite. Increased carbon content also increases the ductile-to-brittle transition temperature and hardenability of steels (21).

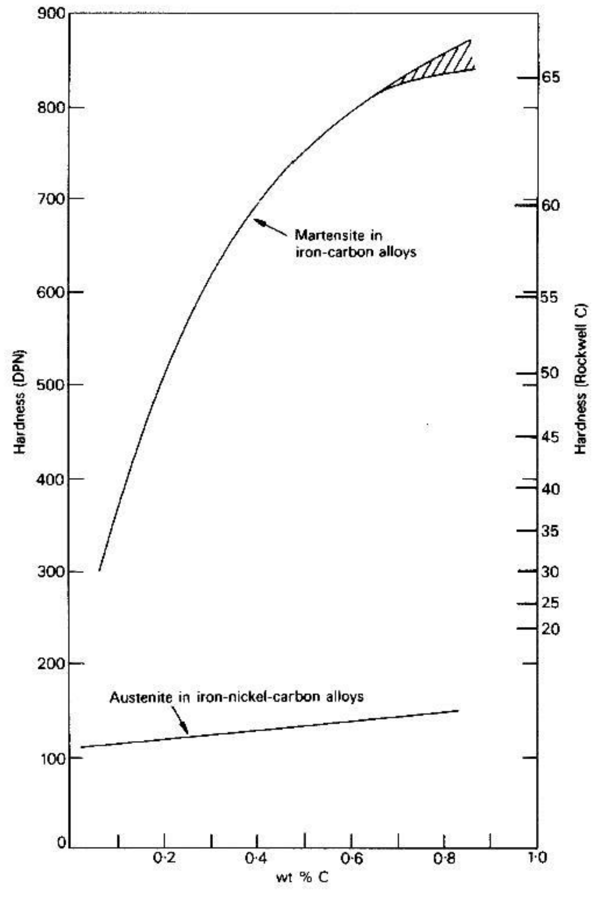

Figure 2-2: The effect of carbon content on the hardness of martensite and austenite (20).

2.2.1.3 Nickel

Nickel is a strong austenite former which stabilizes the austenite phase over an increasing temperature range. It increases the strength and toughness of the steel by substitutional solid solution and also has a grain-refining effect (22). Nickel does not form carbides and in fact makes iron carbides less stable therefore it is never added to a high-carbon steel unless it is accompanied by elements which have a strong carbide-stabilising influence such as manganese (22). It is also used in low alloy steels to reduce the sensitivity to variations in heat treatment and distortion or cracking on quenching (21).

2.2.1.4 Manganese

Manganese is a strong austenite stabilizer which expands the γ-field. It also controls the transformation kinetics on cooling from austenite (21) by depressing the eutectoid temperature and in doing so, also depresses the position of the Time-Temperature-Transformation (TTT) curve relative to the temperature axis (20). Although not a strong carbide former, manganese does have a strong stabilizing effect on carbides and readily enters into solid solution. Manganese is also important in steel production both for deoxidation and desulphurization of the molten steel (22). It combines with sulphur to form MnS inclusions which are brittle at room temperature but increasingly deformable at higher temperatures (20). As an alloying element, addition of manganese is one of the most economical ways of increasing the hardenability of the steel.

2.2.1.5 Molybdenum

Molybdenum is a ferrite stabilizer which contracts the γ-field promoting the formation of ferrite. It strengthens by solid solution strengthening and also forms stable carbides such as Mo_2C and Fe_4Mo_2C improving the hardenability of steels while increasing the high temperature tensile and creep strengths without adversely affecting ductility even when alloyed in small amounts (0.1 to 0.5 wt%). An important use of molybdenum is to reduce the effect of temper embrittlement caused by trace elements such as phosphorous (21, 22). It also enhances the pitting resistance of the surface of steels especially against corrosive attack by chloride solutions (5).

2.2.1.6 Copper

Copper has a FCC structure and is therefore an austenite stabilizer. It does not form carbides and is normally found in solid solution. Copper is usually added to precipitation hardening steels in which it forms Cu precipitates during ageing heat treatments resulting in an increase in tensile and fatigue strength while also improving corrosion resistance. The secondary hardening effect increases with increasing copper content (23).

2.2.1.7 Niobium

Niobium is a ferrite stabilizer and a strong carbide former capable of forming alloy carbides preferentially at alloying concentrations less than 0.1 wt%. It is also responsible for prior austenite grain size refinement by pinning the boundaries and impeding grain growth at the austenitization temperature (5).The formation of NbC also plays a role in lowering the fracture transition temperature (21) as well as eliminating any free carbon thus preventing the formation of other precipitates such as $Cr_{23}C_6$ which, when present at prior austenite grain boundaries, would render the steel susceptible to sensitization.

2.2.2 Heat Treatment of Martensitic Steels

Producing high strength levels in steels is traditionally done by austenitzing and quenching to form martensite. To ensure that complete transformation to martensite is achieved, the steel must be quenched at a rate sufficiently rapid to avoid the decomposition of austenite during cooling to products such as ferrite, pearlite and bainite (20). The physical shape of the specimen and the composition of the steel are two factors which control the effectiveness of the quenching operation. A larger specimen quenched in a particular medium will cool more slowly than a smaller specimen. The addition of alloying elements to the steel reduces the critical rate of cooling needed to make a steel specimen fully martensitic by moving the TTT curve to longer times thus making it easier to pass the nose of the curve during a quenching operation (20). The ability of a steel to form martensite on quenching is referred to as the hardenability.

2.2.2.1 *The martensitic reaction*

The martensitic reaction is a diffusionless shear transformation which forms a characteristic lath or lenticular microstructure without a change in chemical composition (20). In steels, it usually occurs athermally. The reaction begins at a martensite start temperature, M_s, which is dependent upon the concentration of γ-stabilizing alloying elements (nickel, manganese, copper) in the steel. The M_s can vary over a wide temperature range from as high as 500°C to well below room temperature (20). Further transformation occurs during rapid cooling until the reaction stops at the martensite finish temperature, M_f. If the M_f is well below room temperature, some highly alloyed steels do not transform completely to martensite. As a result of the martensitic transformation not going to completion, the subsequent microstructure frequently contains retained austenite. The desirability of retained austenite depends on the particular steel being used and the mechanical properties required in service. Retained austenite is effectively utilized in many steels such as transformation induced plasticity (TRIP) steel, 9%Ni steel and maraging steel.

The characteristics of the formation of martensite differ considerably from those of pearlite and bainite especially regarding the movement of carbon atoms. During the formation of pearlite and bainite, carbon atoms move over many atom distances, away for the regions converting to ferrite and towards those becoming carbide. In the formation of martensite, each carbon atom maintains nearly the same location as it had in austenite, relative to its neighbouring iron atoms. Therefore, the martensite transformation must happen rapidly in order to avoid the affinity for carbide precipitation and ferrite formation since the diffusion of carbon is relatively rapid (24). This usually involves the movement of regions or layers of atoms. In an austenite grain, a small group of atoms shears, and adjusts the lattice dimension to the tetragonal structure. This shearing continues across the grain until it reaches a boundary (24). Martensite forms with an increase in volume due to the inside of the austenite grain becoming strained during transformation to martensite. A driving force or energy difference is thus needed to overcome the induced strain energy of martensitic formation. Undercooling the austenite provides this driving force i.e. to increase the amount of martensite, the austenite must be undercooled more to increase the energy difference between the martensite and the austenite (24).

2.2.2.2 *The tempering of martensite in alloy steels*

Due to the brittle nature of martensite, it is necessary to modify the mechanical properties by reheating the as quenched structure in the range 150-700°C through the process of tempering. Martensite is a highly supersaturated solid solution of carbon in iron which, during tempering, permits sufficient carbon mobility to allow carbides to precipitate. The end result of tempering is a fine dispersion of carbides in an α-iron matrix which often bears little structural similarity to the original as-quenched martensite (20), and consequently, results in an improvement in the strength, ductility, and toughness of the material.

Due to the desirability to obtain the highest strength while still maintaining optimum ductility and toughness, the tempering resistance should be increased. Figure 2-3 (25) shows for an unalloyed 0.1C-12Cr steel a retardation of softening up to around 500°C after which there is a distinct reduction in hardness. The formation of small Cr_7C_3 and M_2X precipitates promotes the retardation of softening while at the higher temper temperatures, larger $M_{23}C_6$ precipitates replace Cr_7C_3 and M_2X resulting in lower hardness. The addition of molybdenum stabilizes the M_2X and delays the change to $M_{23}C_6$ promoting secondary hardening and increasing the temper resistance as seen in Figure 2-4 (25).

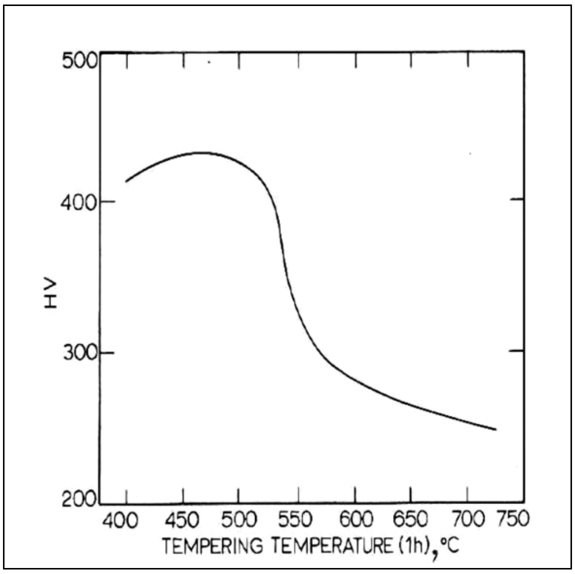

Figure 2-3: The change in hardness with temper temperature for a 0.1C-12Cr steel (25).

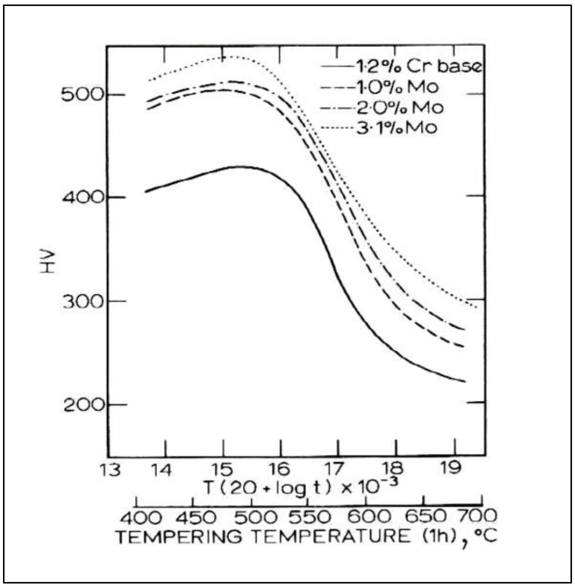

Figure 2-4: Effect of molybdenum on tempering of 0.1C-12Cr steel (25).

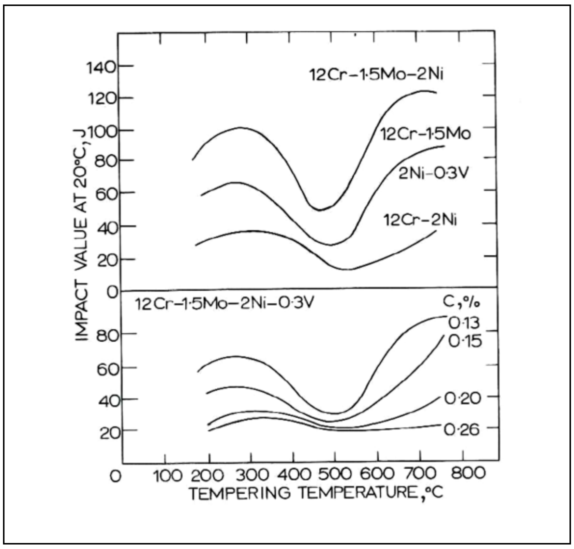

Figure 2-5: Effect of tempering on impact resistance of 12Cr steel at various C levels (25).

Although tempering at the temperature at which maximum secondary hardening occurs produces highest strength, the impact properties are inversely affected as shown in Figure 2-5 (25). The proof stress is also adversely affected due to the internal stresses associated with secondary hardening. By tempering at higher temperatures (overaging), lower strength will be achieved but the proof stress is restored to a high level in addition to a significant increase in toughness. The overaged condition is therefore preferred to provide the optimum stress corrosion resistance (25).

2.2.3 Influence of Microstructure on Mechanical Properties

Mechanical properties necessary for a particular application play a central role in the choice of steels (i.e. their chemistry) and their heat treatment. The internal microstructures thus play a key role in determining these macro-mechanical properties of steels. Of these properties, material strength is of paramount importance in most engineering applications, as is the case in power plant turbine blades. The flow stress can be defined as the stress level at which either plastic deformation or fracture starts to occur; otherwise known as the yield stress and the ultimate tensile stress respectively. It is usually achieved by the combined effect of several strengthening mechanisms and is dependent on the microstructure and its effectiveness in impeding the movement of dislocations (5).

One of the strengthening mechanisms by which dislocation motion is impeded is solid solution strengthening by interstitial atoms e.g. carbon. Carbon atoms have strain fields around them. When these atoms move into the vicinity of dislocations, which also have strain fields around them, it causes an overall reduction in the total strain energy. This leads to the formation of carbon concentrations or atmospheres in the vicinity of the dislocations. Due to the strong binding energy between the carbon atoms and the dislocations, the dislocations become "locked" in position thus increasing the stress required to cause dislocation movement (20).

Substitutional solid solution strengthening also takes place when the metallic alloying elements such as molybdenum, nickel and copper form solid solutions in the matrix. The degree of strengthening achieved by substitutional solute atoms depends on two factors. Firstly, a large difference in atomic size between the original (in the case of steels, iron) atoms and the solute atoms produces a greater disruption of the initial lattice making slip more difficult thereby increasing the strengthening effect (26). Secondly, the greater the amount of solute atoms added, the greater the strengthening effect provided that the solubility limit is not exceeded. The contribution to strength from substitutional solid solution strengthening by more than one alloying element is additive in their effect of increasing the yield strength, tensile strength and hardness of the alloy while almost always resulting in a loss in ductility (26).

Grain size refinement is one of the most effective means of increasing the yield stress of steels. The Hall-Petch equation relates the grain size to the yield stress,

$$^{1}/_{2} \qquad \textbf{Equation-2}$$

where σ_y is the yield stress and d is the grain diameter. and k_y are constants with the former being the friction stress, representing the yield stress of a single crystal ($d^{-1/2}$ = 0) and the latter the dislocation locking factor which is related to the ease of yielding from one grain to another (5). Grain boundaries act as obstacles to dislocation movement causing the dislocations to pile up at the grain boundary. This pile up causes a stress to be generated in adjacent grains and when the stress reaches a critical value, additional dislocations are generated in those grains, thereby propagating yielding from grain to grain. This localized yielding process occurs throughout the microstructure and can be observed macroscopically by the passage of a Luders band. The coarser the grain, the easier it will be to propagate the yielding process, therefore a finer grain size will result in a higher yield stress (20) making grain refinement advantageous in the microstructure. The addition of alloying elements such as niobium and nickel aid in grain refinement in alloy steels.

Impact properties are affected by different factors compared to those for material strength. An increase in stress in a crystalline material increases both the shear stress on each slip system and the normal stress on each cleavage plane. If the shear stress reaches the critical stress for dislocation movement first, plastic deformation occurs. If the normal stress attains the critical value for cleavage first, a pre-existing or newly-formed crack will propagate extremely rapidly on a cleavage plane, causing sudden brittle fracture. The cleavage stress to initiate a crack in the matrix is dependent on the chemical composition of the solid solution in which the crack forms. In steels, cracks may open easily at other places such as in carbides or inclusions; at the particle-matrix interface or they may be present due to fabrication techniques (24). Once cracks are formed, the stress to propagate the crack depends on the microstructure therefore microstructural features impeding crack propagation such as grain boundaries will improve the materials toughness.

Fracture toughness is a measure of a materials resistance to failure in the presence of a flaw (26). The fracture resistance of a material can be optimized by manipulating the microstructure to influence strength and ductility by means of strain hardening, dislocation-particle interactions or slip behaviour (27). In high-strength steels, there is a general inverse relationship between strength and fracture toughness as seen in Figure 2-6 (27). Fracture resistance in quenched and tempered steels can be improved by increasing the austenitization temperature and eliminating coarse alloy carbides. A higher austenitization temperature will result in a higher fracture toughness at all tempering temperatures when compared to a lower austenizing temperature. A further increase in fracture toughness can be achieved in some alloy steels which contain retained austenite, by either crack-tip blunting or strain-induced martensitic transformation at the crack tip during fracture (27).

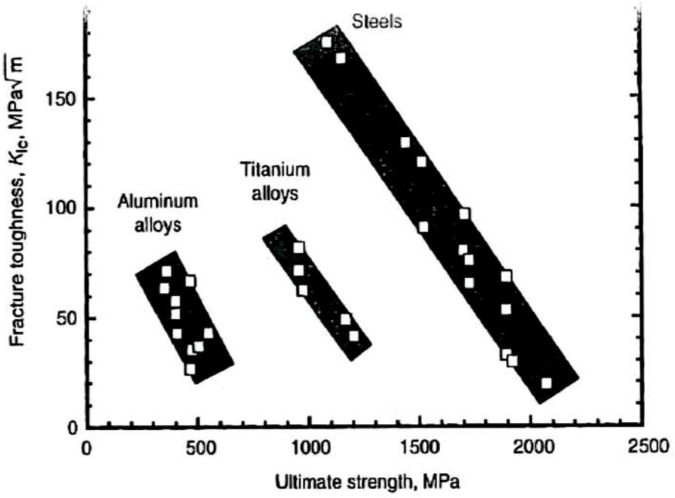

Figure 2-6: Fracture toughness as a function of strength for high-strength structural alloys (27).

2.2.4 Martensitic Precipitation Hardened Stainless Steels

The development of precipitation hardened stainless steels originated during World War II when there was a need for high-strength; corrosion-resistant materials that would retain considerable strength up to moderately elevated temperatures (28). Since then, these steels are widely used in the aeronautical, power and nuclear industries among others. There are three types of precipitation hardened stainless steels available which are austenitic at the annealing temperatures and are classified by their austenitic stability as seen in Figure 2-7.

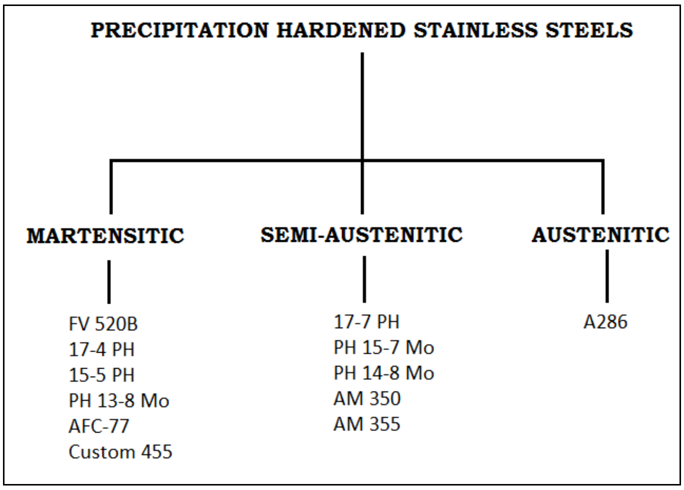

Figure 2-7: The three types of precipitation hardened stainless steels and commercially available grades of each type (28).

The classification of precipitation hardened stainless steels in Figure 2-7 is dependent upon the materials alloy content. High alloy content steels will remain austenitic on cooling to room temperature while those steels with comparatively low alloy content will transform to martensite. The alloy content of the steel also affects its martensitic transformation temperature, as seen in Figure 2-8. Since FV520B is classified as a *martensitic* precipitation hardened stainless steel, this section will focus mainly on this particular type.

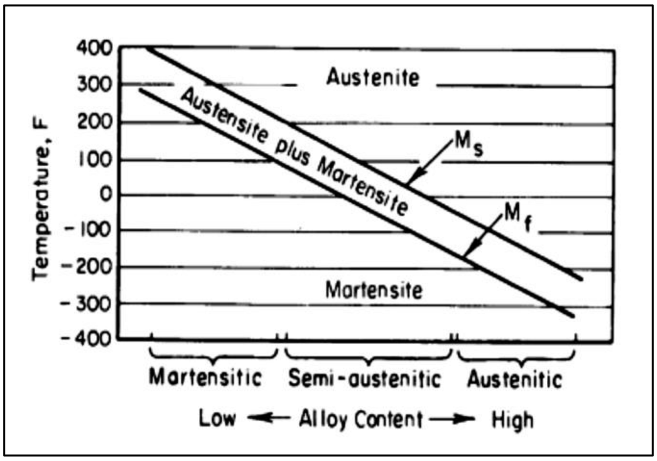

Figure 2-8: The effect of alloy content on the transformation temperature of precipitation hardening stainless steels (28).

The heat treatment of martensitic precipitation hardened stainless steels consists of a three step cycle viz. homogenisation, solution treatment, and precipitation hardening treatment:

1) **Homogenisation** is carried out between 1000°C and 1050°C to remove residual influences from previous hot working operations (8) and produce a homogenous microstructure. Alloying elements are absorbed into the austenitic solid solution matrix

and are more uniformly distributed by diffusion during this treatment (28). The material is then cooled rapidly to room temperature.

2) **Solution treatment or 'primary hardening'** involves reheating the material in the 750°C-850°C range. The importance of the solution treatment temperature is twofold:
   i. It is selected to give the optimum combination of austenite composition in order to control the M_f temperature so that complete martensitic transformation takes place at room temperature upon cooling. If the M_f temperature is below room temperature sub-zero cooling will be required.
   ii. To dissolve significant amounts of hardening elements in the martensite for the precipitation hardening treatment to follow.

Heating to temperatures higher or lower than the recommended temperatures will adversely affect both the metallurgical structure and mechanical properties of the material (28). Rapid cooling (air cooling is sufficient in most cases) ensures that supersaturation of the hardening elements is achieved in the transformed martensitic structure. The structure produced is untempered martensite which does not possess the best combination of tensile strength and ductility, hence the need for a further heat treatment.

3) **Precipitation hardening or 'ageing' treatment** is the final step in the heat treatment cycle. This step involves reheating the steel to intermediate temperatures in the range of 430°C-620°C. The hardening elements, such as copper, form precipitates in the martensite which raises both the hardness and tensile strength. The effect of copper on hardness can be seen in Figure 2-9 (23). Tempering of the martensitic matrix occurs simultaneously, improving the ductility of the steel. By varying the ageing temperature the size and distribution of the precipitates formed are controlled. This enables a wide range of mechanical properties to be developed. At the low temperatures in the precipitation range, small, uniformly distributed particles are formed resulting in the highest strengths. This is known as the peak hardened condition. Ageing at high temperatures causes the precipitates formed to grow large in size. Shearing between the precipitate and the matrix takes place relieving the strain, thus making them ineffective in strengthening. The formation of chromium carbides also occurs at high temperatures thus causing a softening in the material. The yield and ultimate tensile strengths achieved will be approximately the same as for the annealed condition (29) but the ductility will be greatly improved. This is known as the overaged condition.

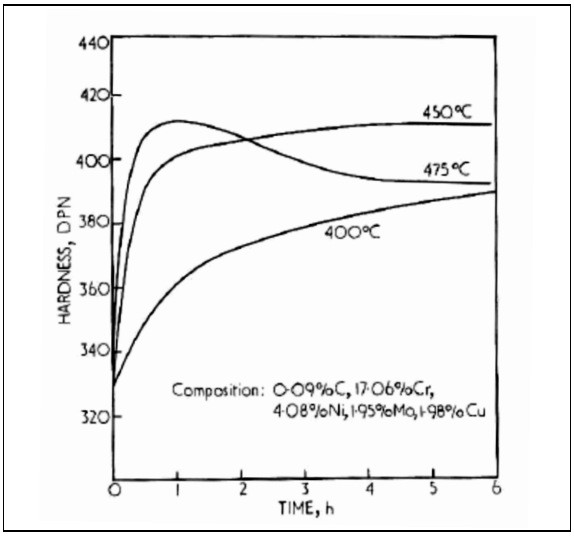

Figure 2-9: Precipitation hardening effect of copper (23).

Figure 2-10 shows the three steps in the heat treatment cycle graphically in terms of temperature and time:

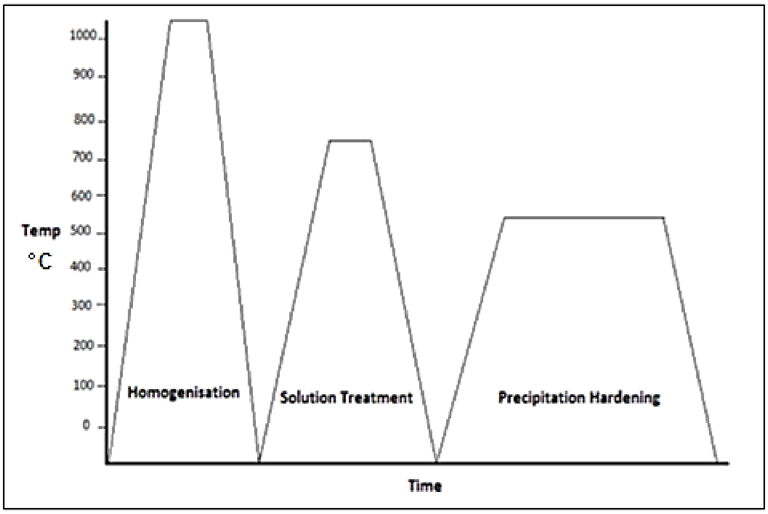

Figure 2-10: Heat treatment cycle of precipitation hardened stainless steels.

Due to the complex chemistry of precipitation hardened steels, various microstructural changes occur during the precipitation hardening (ageing) treatment. One such change is the reversion of the martensitic structure to austenite which is commonly referred to as reverted austenite. This phase is produced when ageing the material close to or above the temperature at which austenite starts to form, i.e. the Ac_1 temperature. The mechanism of its formation is still not clearly understood but it has been proposed that reverted austenite forms as a result of the diffusion of nickel (30, 31) from the surrounding matrix which prevents the transformation to martensite during cooling. Schnitzer et al. (31) and Bhambroo et al. (29) have both reported that the formation of reverted austenite starts during the initial stages of the ageing treatment.

The amount of reverted austenite produced is dependent upon the ageing temperature and time i.e. the higher the ageing temperature or the longer the treatment time at lower temperatures, the greater the amount of reverted austenite formed (5). Mechanical properties of the heat treated material are affected by the presence of reverted austenite. There is a decrease in hardness (30) and strength (29), (32) and an increase in ductility and energy absorption (32) as the volume of reverted austenite increases.

2.2.5 FV520B - 14% Cr stainless steel

FV520B is a low carbon, precipitation hardening martensitic stainless steel used extensively in a wide variety of engineering applications, particularly in the power generating and aerospace industries. Properties exhibited by this material include high strength, excellent corrosion resistance, good high-temperature oxidation resistance and toughness (8) making it a suitable material for use in low pressure steam turbine blades. The typical chemical composition range for FV520B is shown in Table 1.

C	Si	Mn	P	S	Ni	Mo	Cr	Cu	Nb
0.07 max	0.7 max	1.0 max	0.03 max	0.03 max	5.0-6.0	1.2-2.0	13.2-14.7	1.2-2.0	0.2-0.7

Table 1: Typical chemical composition of FV520B (weight percentage, balance Fe) (8).

The standard heat treatment schedules for FV520B as stipulated by the material manufacturer are as follows (8):

Heat treated Condition	Homogenisation	Solution Treatment	Precipitation Hardening Treatment
Peak Hardened	30 min @ 1050°C Air cooled	2 hours @ 750/850°C Air cooled	4 hours @ 450°C Air cooled
Standard Overaged	30 min @ 1050°C Air cooled	2 hours @ 750°C Air cooled	2 hours @ 550°C Air cooled
Softened Overaged	30 min @ 1050°C Air cooled	2 hours @ 750°C Air cooled	2 hours @ 620°C Air cooled

Table 2: Standard heat treatment schedules for FV520B.

2.3 Corrosion in power plant alloys

According to DIN ISO 8044, corrosion can be defined as the “physical interaction between a metal and its environment which results in changes of the metal’s properties and which may lead to significant functional impairment of the metal, the environment or the technical system of which they form a part.” (33). In power plants, which use various metals in many different environments, corrosion has proven to be a significant problem with corrosion-related costs running into the billions of dollars annually (1).

The corrosion of metals is almost always due to an electrochemical reaction which can be defined as a chemical reaction involving the transfer of electrons. An electrochemical cell is formed which contains an anode and cathode physically connected to one another and immersed in an electrolyte. A diagram of an electrochemical cell can be seen in Figure 2-11.

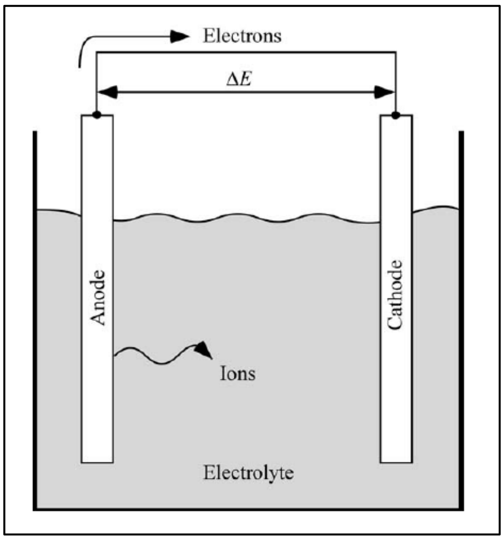

Figure 2-11: A simple electrochemical cell (34).

Atoms from the anode material give up electrons, resulting in ions being released into the electrolyte and electrons flowing to the cathode. A voltage drop (ΔE) occurs between the anode and cathode. Over time, the anode is consumed (i.e. oxidised) as it releases ions into the electrolyte. The cathode accepts the released ions and is reduced. The reactions at the anode and cathode occur simultaneously and at the same rate. This is clearly demonstrated in the corrosion of steel in aerated water, as seen below.

The anodic reaction involves the oxidation of the metal to its ion:

Equation-3

where e^- is the number of electrons produced.

During the simultaneous cathodic reaction, the reduction of oxygen within the electrolyte takes place:

Equation-4

Combining Equation-3 and Equation-4 gives the overall reaction:

Equation-5

The product of the above reaction, ferrous hydroxide, is unstable in aerated water. It combines with water and oxygen to produce ferric hydroxide which is a reddish-brown corrosion product that falls out of the solution:

$$_2\mathrm{O} + -$$ **Equation-6**

Drying in the atmosphere dehydrates this ferric hydroxide and forms the red-brown ferric oxide, Fe_2O_3, commonly known as rust:

Equation-7

2.3.1 Corrosion Mechanisms in a Steam Turbine

The corrosion mechanisms in a steam turbine are dependent on the following factors:

- the materials used in the manufacture of the components,
- the stresses experienced during operation, and
- the local environmental conditions.

The corrosion mechanisms most prevalent in steam turbines are pitting corrosion, stress corrosion cracking (SCC), corrosion fatigue (CF), and to a lesser extent erosion and erosion corrosion (E-C) as seen in Figure 2-12. Although these mechanisms are classified separately, they do not necessarily operate independently of each other. One form of corrosion can sometimes initiate the start of another, e.g. pitting can lead to crack formation and SCC. The corrosion mechanisms pitting, CF and SCC will be looked at in greater detail the following sections.

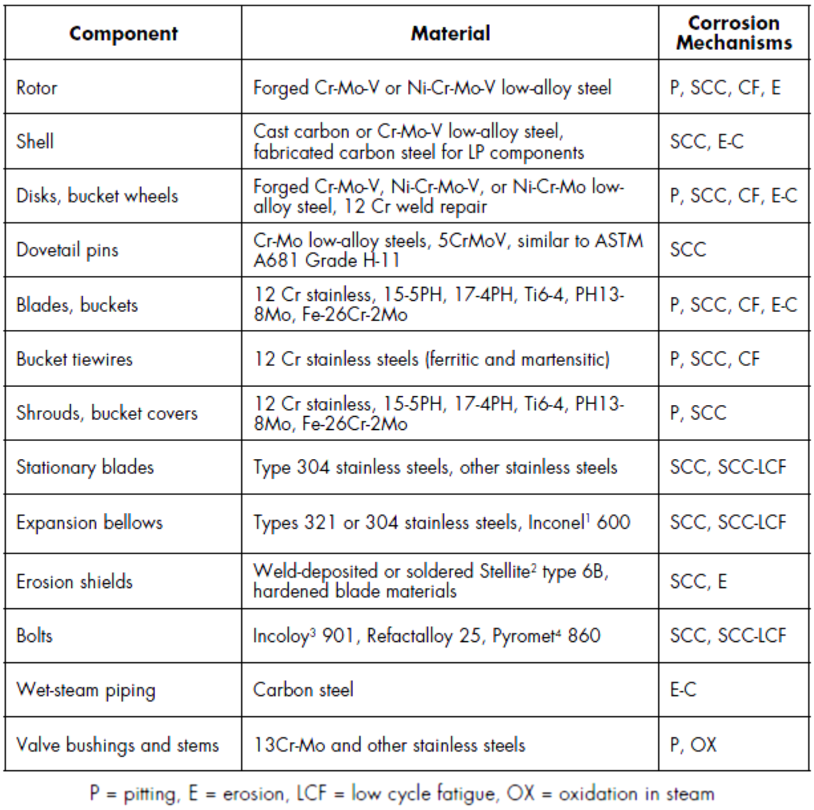

Component	Material	Corrosion Mechanisms
Rotor	Forged Cr-Mo-V or Ni-Cr-Mo-V low-alloy steel	P, SCC, CF, E
Shell	Cast carbon or Cr-Mo-V low-alloy steel, fabricated carbon steel for LP components	SCC, E-C
Disks, bucket wheels	Forged Cr-Mo-V, Ni-Cr-Mo-V, or Ni-Cr-Mo low-alloy steel, 12 Cr weld repair	P, SCC, CF, E-C
Dovetail pins	Cr-Mo low-alloy steels, 5CrMoV, similar to ASTM A681 Grade H-11	SCC
Blades, buckets	12 Cr stainless, 15-5PH, 17-4PH, Ti6-4, PH13-8Mo, Fe-26Cr-2Mo	P, SCC, CF, E-C
Bucket tiewires	12 Cr stainless steels (ferritic and martensitic)	P, SCC, CF
Shrouds, bucket covers	12 Cr stainless, 15-5PH, 17-4PH, Ti6-4, PH13-8Mo, Fe-26Cr-2Mo	P, SCC
Stationary blades	Type 304 stainless steels, other stainless steels	SCC, SCC-LCF
Expansion bellows	Types 321 or 304 stainless steels, Inconel[1] 600	SCC, SCC-LCF
Erosion shields	Weld-deposited or soldered Stellite[2] type 6B, hardened blade materials	SCC, E
Bolts	Incoloy[3] 901, Refactalloy 25, Pyromet[4] 860	SCC, SCC-LCF
Wet-steam piping	Carbon steel	E-C
Valve bushings and stems	13Cr-Mo and other stainless steels	P, OX

P = pitting, E = erosion, LCF = low cycle fatigue, OX = oxidation in steam

Figure 2-12: Steam turbine main components, materials and corrosion mechanisms (1).

2.3.2 Pitting Corrosion

Pitting corrosion is a form of localized corrosion attack of a material with an otherwise resistant surface (1). The shape of pits can differ from wide and shallow to deep and narrow. Pit characteristics such as their depth and morphology are dependent on the metallurgy of the material and the specifics of the local chemistry. The nature of pits is often not recognized as they are hidden by corrosion products.

Pitting corrosion is observed in passive film forming alloys, such as stainless steels, in steam turbine environments. Although passive films can provide improved corrosion resistance to materials they can also make them susceptible to pitting corrosion. The presence of an aggressive local environment in a steam turbine comprising concentrated aqueous electrolytes and the presence of oxygen can cause the passive films to break down locally. Since oxygen levels are typically low during on-load conditions, this is more likely to occur during shutdown periods when liquid oxygenated films of chlorides and sulphates may form on blade and disc surfaces. A concentration of these impurities in the defective passive film allows self-sustaining corrosion reactions to develop and initiate pit formation. The base of the pit becomes anodic and leads to further dissolution of the metal while the surrounding metal surface becomes cathodic, supporting the reduction of dissolved oxygen or other oxidizers. Mass transport of species between the anodic pit and cathodic surfaces is prevented by the sheltered pit geometry, allowing the pit to acidify and further sustain the corrosion (1).

The susceptibility of materials to pitting corrosion is also dependent on the electrochemical potential. An applied potential exceeding the film breakdown or critical pitting potential (E_b) will lead to spontaneous pitting. If the potential decreases to the appropriate level, repassivation of the surface can occur. The difference between the pitting and repassivation potentials provides an indication of the sustainability of pits to continue growing i.e. the larger the difference between pitting and repassivation potentials, the greater the susceptibility for continued growth of the pits. Factors affecting the critical pitting potential include the environment and alloy chemistry. The presence of chlorides tends to increase current densities at all potentials and decrease the critical pitting potential, resulting in increased susceptibility. This was clearly demonstrated by Williams et al. (35) who conducted pitting corrosion experiments on two industry-standard turbine blade steels, FV566 (12Cr) and FV520B (14Cr). They showed that in deaerated aqueous NaCl at near-neutral pH, both alloys exhibited a dependence of pitting potential on chloride concentration following the general relationship for stainless steels:

$$E_b = A + B\log_{10}[Cl^-] \qquad \textbf{Equation-8}$$

where A and B are constants. When plotted according to Equation-8, their data described reasonable straight lines thereby concluding that at any given temperature, the pitting potential decreased with increasing chloride concentration while the anodic current density was found to increase.

As chromium content of an iron alloy increases, so does the critical pitting potential, resulting in increased resistance. A correlation between pitting potential and pitting resistance equivalent number (PREN) was demonstrated by Williams et al. (35) for three stainless steel alloys, FV566 (12Cr), FV520B (14Cr) and AISI 304 (18Cr). The PREN is an empirically derived function of chromium, molybdenum and nitrogen content such that:

$$\mathrm{PREN} = \mathrm{Cr\ (wt\%)} + 3.3\ \mathrm{Mo\ (wt\%)} + \mathrm{X\ N\ (wt\%)} \qquad \textbf{Equation-9}$$

where X typically lies between 11 and 30. Values of pitting potential were taken under identical conditions of chloride concentration and temperature for all three alloys. PREN's were calculated using Equation-9 in conjunction with the alloys' chemical composition. The results showed that pitting potential increases with PREN (and subsequently chromium content) of the alloy at all chloride concentrations. The similarity of results for FV520B and AISI 304 was noticeable with FV566 being markedly lower. The results led Williams et al. to conclude that once pits become initiated, the probability of a transition from metastable pitting to stable pitting at any given potential is determined by the metal's chromium content. The hypothesized mechanism for the transition was that for a given potential, temperature, and pit geometry, increasing Cr decreases the probability of a metastable pit, completing the transition to a stable state by increasing the minimum metal chloride concentration that must be maintained within the pit environment to avoid repassivation during the transition period (35).

Manganese sulphide (MnS) inclusions in the metal, formed during the steel-making process, have been known to play a role in pit initiation due to their preferential dissolution. Shimahashi et al. (36) investigated the effect of MnS inclusions on pit initiation and cracking in a commercial

Type 304 stainless steel both with and without an applied stress in an $MgCl_2$ solution. In the absence of applied stress, manganese and sulphur dissolve during anodic polarization and a composition change from a complex sulphide of manganese and chromium (Mn,Cr)S to a chromium sulphide (CrS) covered with an oxide film occurred. Trenches were formed at the boundaries between the steel matrix and the inclusion. Both metastable and stable pits were formed in the trenches with trench depth being the hypothesized determining factor for whether metastable or stable pits are formed. Under applied stress, stable pits were consistently formed during anodic polarization with micro-cracks initiated on the inclusion surface, most likely attributed to the rupture of the oxide film on the inclusion due to the applied stress.

Propagation of pits requires both the anodic and cathodic electrochemical reactions to be sustained. Pit growth rates are affected by a number of factors, including pH, impurity species and concentration, and temperature. The growth rate kinetics are complex and subject to the metal, the nature of the passive film, and the environment (1). For pitting in constant environmental conditions, parabolic rate behavior is often described (5, 37) by a relationship of the form:

$$d = At^n \qquad \textbf{Equation-10}$$

where d and t are pit depth and time respectively. A and n are system specific constants. For pitting in fluctuating conditions, such as during turbine start-up and shutdown sequences, the kinetics are more difficult to predict.

While pitting does not necessarily lead to severe corrosion damage that affects the functionality of steam turbines, it can cause minor roughening of the material surface which can disrupt the steam flow across the surface and thus change the designed steam flow through the turbine. This can cause unexpected stresses which, if vibratory in nature, can lead to problems associated with fatigue (1). A more significant problem associated with pitting presents itself when the stress and environmental conditions are such that a pit can transition into a crack. Under static loads, the newly developed crack would then be subject to SCC. If the load is dynamic, corrosion fatigue would likely be the dominant mechanism. Turbine failures have occurred as a result of cracks developing from corrosion pits in both blade and disc materials and the consequences of such failures are often catastrophic (35).

2.3.3 Corrosion Fatigue

Corrosion fatigue combines the detrimental features of fatigue and corrosion. Fatigue is due to cyclic loading of a material at levels below yield strength that results in localized plastic deformation and crack initiation. Once the crack has initiated, the stress concentration at the crack tip due to the continued loading will allow it to propagate relatively quickly resulting in fracture. Corrosion fatigue can therefore be defined as the acceleration of fatigue crack growth due to interaction with the environment (34).

The influence of the environment on corrosion fatigue performance can be seen in Figure 2-13 (38) for a 13% Cr steel, used in steam turbine blades. The two graphs represent results for a smooth test specimen (left) and a notched test specimen (right). It can clearly be seen that corrosion fatigue performance declines as the test environment becomes more severe for both types of test specimens. For the smooth test specimen, the fatigue limit in the 1% NaCl solution is reduced to about 25% of its value in air. The overall performance of the notched specimen in all test environments is greatly reduced although the difference in the fatigue limit between the different test environments for the notched specimen is less pronounced. Spiedel (38) parallels the effect of the notch to the effect of aggressive environments on the corrosion fatigue of this and similar Fe-Ni-Cr alloys. The 1% NaCl test solution was found to produce pitting corrosion. It is strongly believed that localized corrosion such as pitting plays an important role in corrosion fatigue crack initiation by providing stress concentrations or by collecting damaging species in occluded corrosion cells (38). Corrosion fatigue cracks tend to form slowly, contain corrosion products on the crack surface and are often blunted. They are more likely to be transgranular (i.e. propagate through grains), similar to fatigue cracks in inert environments (1).

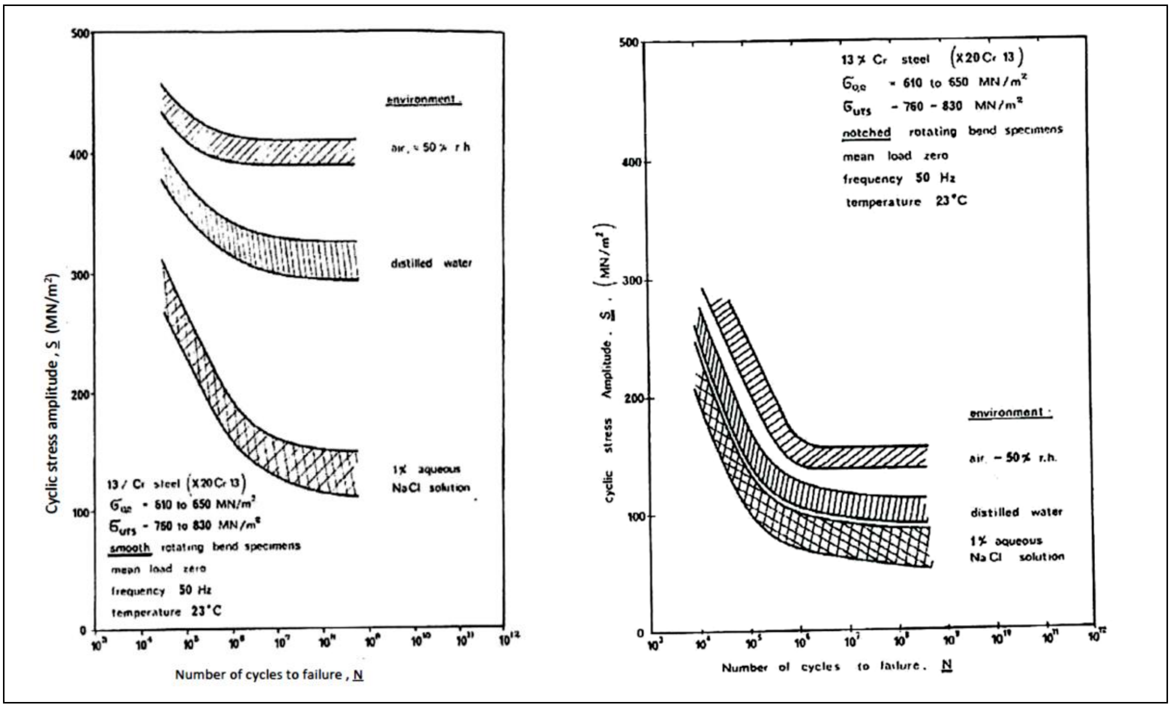

Figure 2-13: Corrosion fatigue of 13-Cr steel in different environments for smooth (left) and notched (right) specimens (38).

Fatigue crack growth rates in inert environments are independent of loading frequency. However, crack growth rates in corrosive environments are dependent on loading frequency. At low frequencies, the behavior is time-dependent and allows enough time for corrosion kinetics to play a role (1, 38). It is therefore typically with low frequency that the greatest effect of the environment is observed. At high frequencies, the crack growth rate is purely cycle dependent and the effect of the environment is insignificant (38). At intermediate frequencies, there is a combination of time- and cycle-dependent behavior.

Vibration in blades is the main cause of cyclic stresses in steam turbines as a result of mistuning or interrupted flow in the turbine (1). Vibrations produce cyclic stresses with an extremely high number of cycles of very small loads. Interrupted flow in the turbine can lead to undesirable vibrational stresses through the formation of pits on the blade surface. Extensive effort is made to minimize vibrations through proper design and construction. Shroud connections or lashing wires can be used to minimize vibrations. Blades are also tuned to prevent buildup of resonant vibrations.

The corrosion fatigue strength of Fe-Ni-Cr alloys in aqueous environments can be improved by the following parameters:

Metallurgical Parameters	**Mechanical Parameters**	**Environmental Parameters**
High Cr, Mo, Ni contents	Highly polished surfaces	Low concentration of pitting agents
Small grain size	Compressive stresses on surface	Cathodic protection
High fatigue strength	No notches	Inhibitors
Coating with mild steel	Low mean stress	Protective oils
Avoid sensitization	High frequency	Low temperature

Table 3: Parameters which improve corrosion fatigue strength in aqueous environments (38).

2.3.4 Stress Corrosion Cracking

Stress-corrosion cracking (SCC) is an extremely complex phenomenon involving environmentally induced sub-critical crack propagation. The complexity arises from the synergistic interaction of mechanical, environmental and metallurgical factors that promotes crack propagation which can ultimately lead to service failures. SCC will only occur if all three of the following requirements are satisfied i.e. a tensile stress, a corrosive environment and a material that is susceptible to said corrosive environment.

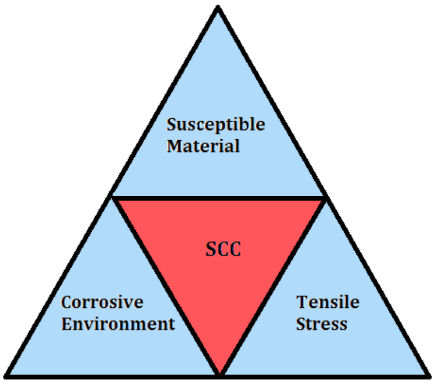

Figure 2-14: Schematic showing the interaction of the factors that promote SCC.

2.3.4.1 Characteristics of SCC

The following characteristics by Brown (2) are common to most if not all SCC although they are generalized and there are exceptions which do exist:

1. Pure metals are generally immune to SCC however there are specific environment/metal reactions that occur to allow crack advance. In the case of SCC of iron and nickel, this reaction occurs between the environment and impurities segregated to the grain boundaries (39).
2. A tensile stress is necessary which may be provided by an applied service stress or a residual stress although compressive residual stresses are sometimes used to prevent SCC. The applied load is usually static for SCC, as compared to cyclic loading for corrosion fatigue as seen in the previous section.
3. The environments which produce SCC in an alloy are limited i.e. only certain species will cause SCC in a particular alloy.
4. Usually, the alloy susceptible to SCC in a specific environment is relatively inert with respect to that environment in the absence of stress although low alloy high strength steel may experience general rusting.
5. The concentration of specific corrodent species necessary to initiate SCC in an alloy is low. Also, the localized concentrations of these species in the active corrosion sites differ greatly from the bulk environment e.g. in steels undergoing SCC in neutral or alkaline salt water, the corrodent within the cracks is conspicuously acidic.
6. SCC cracks appear brittle even though the alloy may fracture in a ductile manner in a mechanical tensile test. The SCC fracture mode is also generally different to the plane strain fracture for the same alloy.
7. Some alloy/environment systems appear to have a threshold stress intensity below which SCC does not occur.

2.3.4.2 SCC Crack Initiation Processes

Stress-corrosion cracking in structures frequently initiates at pre-existing crack-like defects. Grooves, laps, or burrs resulting from fabrication processes provide favourable initiating features for SCC cracks to develop. If a metal covered with an oxide film does not contain a pre-existing flaw, the initiation of cracks will follow the sequence of events as depicted in Figure 2-15:

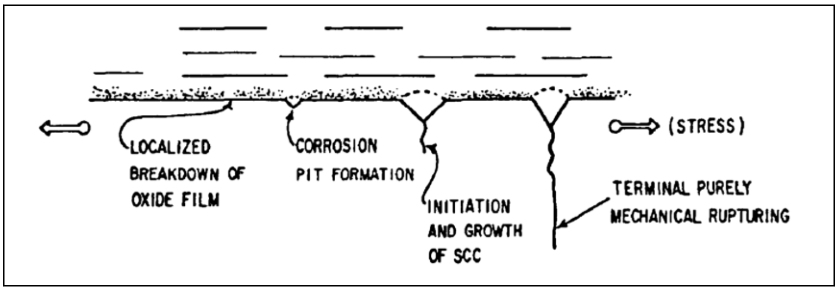

Figure 2-15: Sequence of events in SCC of initially smooth surfaces (2).

The first step is the rupture of the oxide film either mechanically or by the action of a chemical species resulting in the initiation of pitting. Pits will form when the electrochemical potential exceeds the pitting potential. The transition from pitting to cracking is dependent on the same parameters that control SCC such as the electrochemistry at the base of the pit, pit geometry, chemistry of the material, and stress or strain rate at the base of the pit (39). Other forms of localized corrosion which can initiate cracking include crevice corrosion, de-alloying, intergranular corrosion and localized dissolution along slip bands due to slip-induced rupture of oxide films (40).

2.3.4.3 Mechanisms of SCC Crack Propagation

It has been said that due to the specificity of SCC, a single, general, unified mechanism for all systems is not likely (41). However, broadly speaking, it can be said that there are certain processes (chemical, mechanical, electrochemical) which take place to cause the breaking of the interatomic bonds of the crack tip and result in crack propagation. It is the degree to which each of these elemental processes operates that controls the cracking and it is the combination of these processes that encompasses the mechanism. Many different mechanisms have been proposed to explain the complex interaction that occurs at the crack tip. The following is a list of the more prominent mechanisms found in literature:

Pre- Existing Active Path Model

Grain boundaries are high energy regions which makes them favorable to anodic dissolution compared to the grain interior. Solute segregation and precipitation along grain boundaries create localized anodic zones. Crack initiation and propagation due to dissolution can occur in these anodic areas along the grain boundaries thus following a “pre-existing active path”. Since the crack propagates along grain boundaries the morphology is intergranular. The action of tensile stress would be to open the crack further exposing the crack tip to the electrolyte. The classic case of sensitization of austenitic stainless steel is one example of active path corrosion where the precipitation of chromium carbides along the grain boundaries results in a depletion of chromium adjacent to the grain boundaries to levels below that required for passivity. These Cr depleted regions are then susceptible to corrosive attack.

Film Rupture

In order for the crack to propagate by the film rupture model, the corrosion rate at the crack tip must be much greater than the corrosion rate at the crack walls (34). The passivating film at the crack walls inhibits corrosion while plastic strain at the crack tip causes the passive film to fracture locally exposing bare metal to the environment as seen in Figure 2-16 (34). The freshly exposed bare metal then dissolves rapidly, resulting in crack extension by anodic dissolution. There are a number of variations of the film rupture model which usually fall into two categories relating to the rupture of the passive film at the crack tip. Some models assume that once propagation starts, the film remains ruptured leaving the crack tip bare. This could be due to the rate of repassivation being less than the rate of film rupture at the crack tip. Others assume that the crack tip repassivates completely and is periodically ruptured by the emergence of slip steps (39). This results in the formation of crack arrest marks on the fracture surface as seen in Figure 2-17 (34).

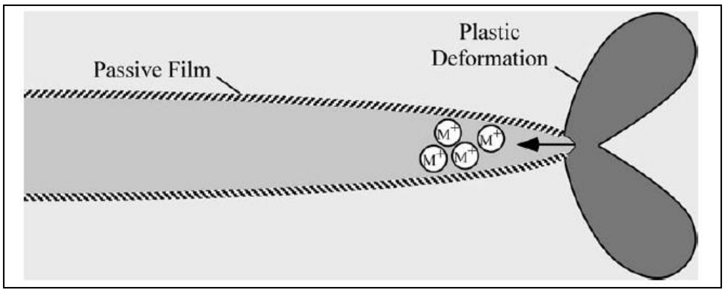

Figure 2-16: The film rupture model (34).

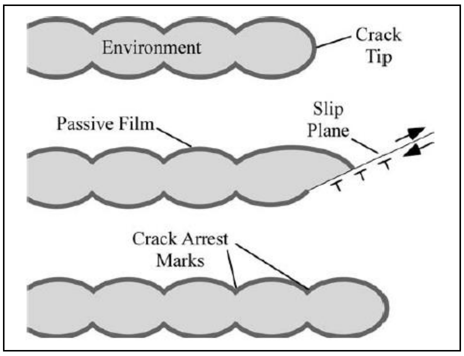

Figure 2-17: Film rupture model with discontinuous crack growth (34).

Corrosion Tunnel Model

In the crack tip slip-step zone, multiple small corrosion tunnels form which progress inside the material. These tunnels will grow in diameter and length while the ligaments between adjacent tunnels are reduced. The stress experienced by the ligaments will increase until they fracture due to ductile overload. The crack propagation is thus due to alternating tunnel growth and ductile fracture. A modification to this model explains the influence of tensile stress which results in a change in appearance from tunnels to thin flat slots, as shown in Figure 2-18 (39).

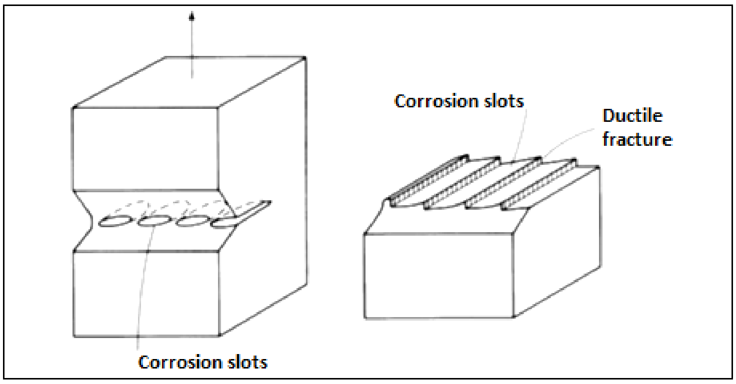

Figure 2-18: Corrosion tunnel mechanism showing flat slot formation (39).

Film-Induced Cleavage Model

The film-induced cleavage (FIC) model for SCC involves the repeated formation and fracture of a brittle film by corrosion at the crack tip. The newly formed film undergoes rapid brittle fracture which continues into the underlying metal covering a distance much greater (10 – 1000X) than the film thickness before the crack arrests and blunting occurs. The brittle film forms again and the crack is propagated. Some important properties of the film are as follows (40):

a) The film should be brittle in structure,
b) It should be strongly bonded to the substrate,
c) The degree of coherency with the substrate will affect cracking.

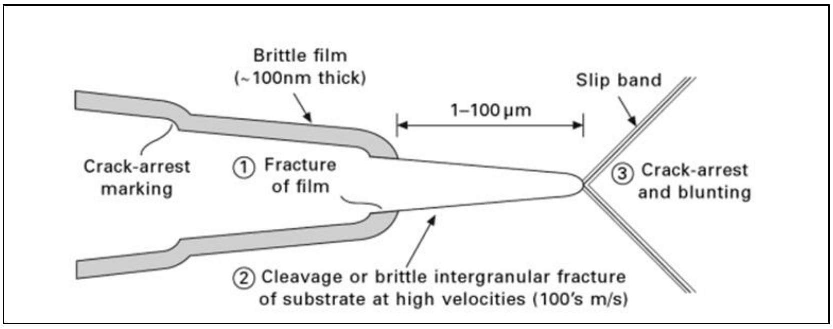

Figure 2-19: Film-induced Cleavage model (40).

Adsorption-based Mechanisms

This mechanism assumes that adsorption of specific ion species from the environment could affect deformation and fracture of solids due to decreases in surface energy. Uhlig (42) proposed that the adsorption of specific ions weakens the strained interatomic bonds at the crack tip thereby promoting crack growth by decohesion along a cleavage plane or a grain boundary. In the model proposed by Lynch (40), known as the 'adsorption-induced dislocation-emission' (AIDE) mechanism, adsorption aids the nucleation of dislocations rather than decohesion thus promoting the shear processes responsible for brittle cleavage-like fracture at the crack tip through the formation and coalescence of micro-voids in the plastic zone ahead of the crack tip.

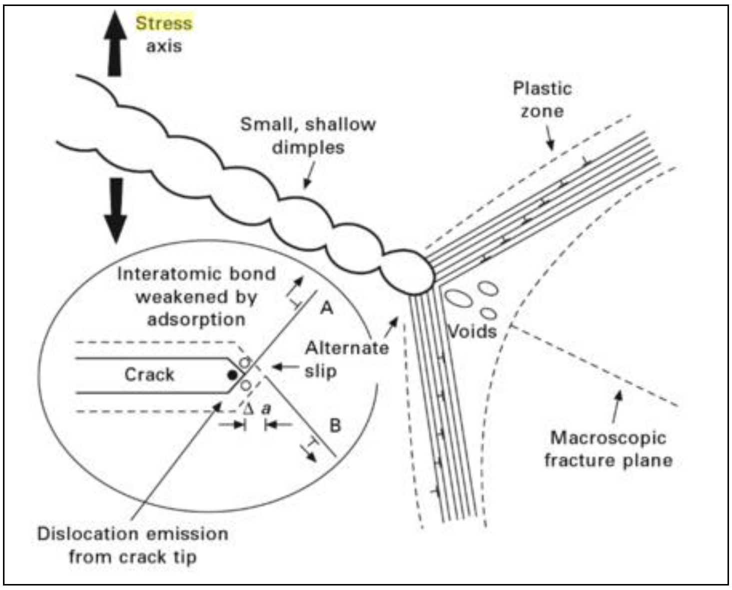

Figure 2-20: Schematic showing the adsorption-induced dislocation-emission (AIDE) mechanism (40).

Hydrogen Embrittlement

The presence of atomic hydrogen in an alloy can cause the mechanical behavior to change. Toughness and ductility can be reduced dramatically, and subcritical crack growth can occur resulting in non-ductile fracture. This process is known as hydrogen embrittlement (HE).

Stress-corrosion cracking in some material/environment couplings can be a form of hydrogen-induced subcritical crack progression (39) and mechanisms of SCC based on the effects of hydrogen are widely accepted for many materials e.g. high-strength steels and alloys of nickel, titanium and aluminium.

The process of HE depends on three major factors (43):

1. The origin or source of the hydrogen.
2. The transport process to move the hydrogen from its source to the locations where embrittlement occurs.
3. The embrittling mechanism at the failure location.

Hydrogen sources: Hydrogen may be present within the alloy or it may exist externally and be in contact with the alloy. Internal hydrogen can be retained during the melting, casting and pickling of alloys or as a result of using damp welding electrodes (21). External sources of hydrogen include service in a molecular gas environment and, importantly for SCC in aqueous environments, the cathodic reaction during the dissociation of water:

$$2\mathrm{H}^+ + 2\mathrm{e}^- \rightarrow \mathrm{H}_2 \qquad \textbf{Equation-11}$$

Hydrogen transport: The transport of hydrogen from an external source such as an aggressive aqueous environment to the degradation site would require adsorption of hydrogen onto the metal surface and diffusion into the lattice structure (44). Due to the hydrogen atom being smaller than most metallic atoms such as iron or aluminium, they are able to fit within interstitial sites in a metallic crystal (34) making its diffusivity in these structures considerably large. Hydrogen transported through lattice diffusion can accumulate at various microstructural features, such as dislocations, grain boundaries, inclusions, voids, and impurity atoms. Hydrogen trapping at these sites has been observed to be an important role in controlling the hydrogen solubility and diffusion efficiency thus affecting the likelihood of HE occurring (43).

Hydrogen mechanisms: According to Lynch (40), mechanisms of SCC based on hydrogen can be classified in two groups: 1) mechanisms based on solute hydrogen which can be further categorized into hydrogen-enhanced decohesion (HEDE) mechanisms or hydrogen-enhanced localized-plasticity (HELP) mechanisms, and 2) mechanisms based on adsorbed hydrogen such as AIDE explained previously.

HEDE postulates that hydrogen concentrates in regions of high stress where the lattice is slightly dilated or at trap sites such as particle-matrix interfaces or grain boundaries. This results in the weakening of the interatomic metal bonds at or near the crack tip so that separation of the metal atoms occurs (40). A decrease of electron-charge density between the metal atoms is thought to occur as a result of the presence of hydrogen at the crack tip or at interstitial sites (43).

HELP occurs when concentrated hydrogen facilitates dislocation activity in the plastic zone ahead of cracks (40).This leads to softening of the material on a localized scale due to the hydrogen atmospheres rearranging themselves, rapidly minimizing the total elastic energy. Decreased resistance to dislocation motion and increased dislocation velocities results. Due to the concentration of hydrogen in the areas around the crack tip, local deformation occurs in these regions.

The AIDE process, as explained previously, involves the weakening of substrate interatomic bonds through adsorption. In the case of hydrogen as the adsorbed species, its large diffusivity enables adsorption to occur at external crack tips as well as internal cracks and voids ahead of cracks. High hydrogen concentrations at crack tips are also the result of greater diffusivity enabling a higher degree of metal-to-metal bond weakening (40).

2.3.4.4 SCC Crack Morphology

SCC cracks can be either intergranular (IGSCC) or transgranular (TGSCC) in appearance with a single dominant crack propagating alone or a branched network. It is not uncommon for both intergranular and transgranular fracture to appear on the same fracture surface. Intergranular fracture surfaces produced by SCC often have a ‘rock-candy’ appearance where crack propagation occurs along grain boundaries. Transgranular cleavage-like fracture surfaces exhibit fine-scale features such as serrated steps. Crack arrest markings can also be seen in both intergranular and transgranular fracture surfaces (40).

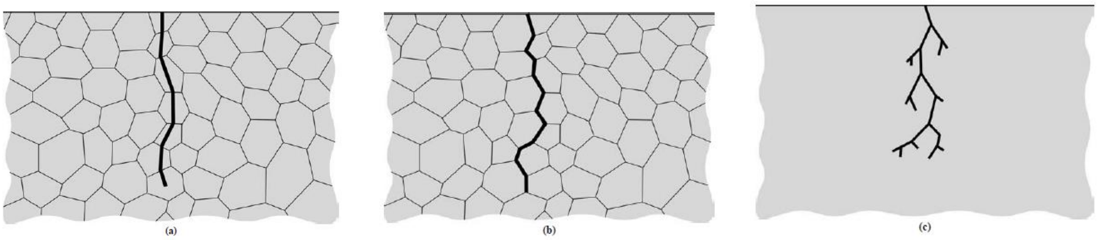

Figure 2-21: SCC crack morphology: a) Transgranular b) Intergranular c) Crack branching (34).

2.3.4.5 Metallurgical Factors Affecting SCC

Alloy composition

Alloying elements and compounds that are present in an alloy can affect its SCC behavior. Alloy composition in stainless steels can affect passive film stability, grain boundary precipitation and grain boundary segregation. Chromium concentrations in the alloy will determine the stability of the passive film which can affect the nucleation of pits on the surface of the metal. Grain boundary precipitation of chromium carbide results in a depletion of chromium in the regions adjacent to the grain boundaries making these areas susceptible to anodic dissolution and intergranular SCC as seen in austenitic stainless steels. Grain boundary segregation of minor alloying elements can increase the susceptibility to SCC by promoting hydrogen adsorption/absorption and contributing to weakening of metal-to-metal bonds together with hydrogen (40). Electrochemical reactions can also be influenced by the amounts of alloying elements and impurities. Variations in alloy chemistry can modify the polarization and greatly affect SCC behavior (34).

Grain size

The effect of grain size on SCC susceptibility seems to differ among different researchers. Variation in grain size in AISI 4340 steel produced little effect on threshold stress intensity for SCC, although decreasing grain size did lower crack growth rates according to Procter et al. (45). This is in contrast to Banerji et al. (46) who showed a decrease in threshold stress intensity for SCC with an increasing prior austenite grain size for a high purity 4340 steel. This disparity is probably due to the high impurity levels in the commercial steel. The SCC behaviour in the commercial steel could thus not be improved by grain refinement alone.

Heat treatment

For a specific alloy composition, different heat treatments will produce varied microstructures each having a distinctive response to similar stress corrosion conditions (44) i.e. an alloy may be immune in one heat treatment and susceptible in another. It is well recognised that, in most cases, high-strength alloys are more susceptible to SCC than low-strength alloys (34, 40). This is especially significant in high-strength steels where tempering and aging can produce a range of strength levels with improvement in SCC resistance at increasing temper temperatures. Steam turbine disk and blade materials fall into the category of high-strength steels, which due to their operating environments are susceptible to SCC.

Numerous studies (18, 19, 47) have been conducted on steam turbine materials to evaluate their SCC behavior in different environments. Speidel et al. (19) have shown that yield strength plays a crucial role in the stress corrosion crack growth rates (CGRs) of steam turbine materials as seen in Figure 2-22. In the figure on the left, for three blading steels (a 13% Cr steel and two precipitation hardening steels) tested in hot water, there is a definite increase in the CGRs for increasing yield strengths. The scatter in the results could be as a result of different microstructures due to different heat treatments. In the figure on the right, the effect of varying precipitation hardening temperature on stress corrosion CGRs was investigated for a precipitation hardened blade material. It can be seen that annealing temperatures corresponding to peak strength resulted in higher CGRs thereby implying the benefit of overaging.

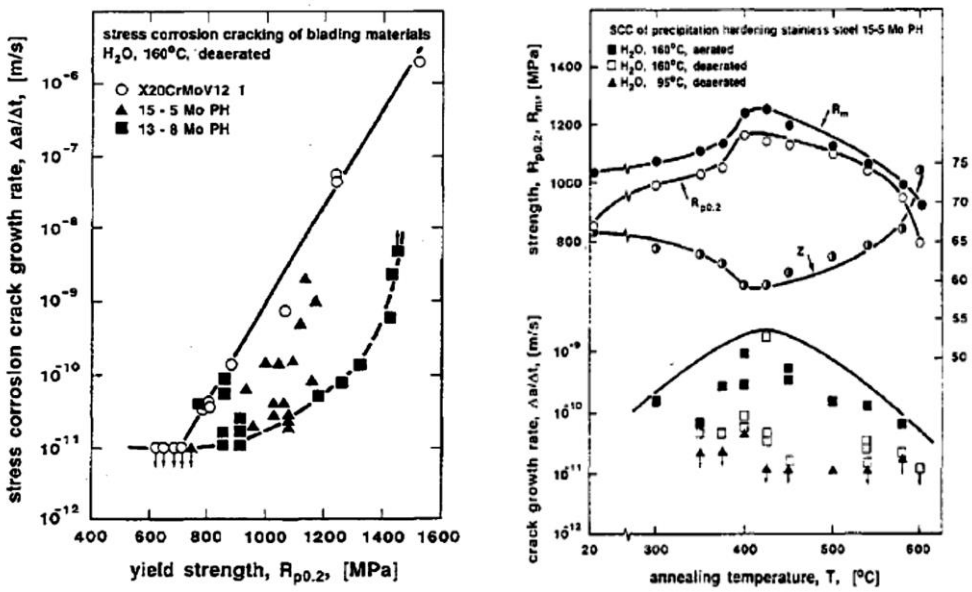

Figure 2-22: Left - Stress corrosion CGRs vs. yield strength for steam turbine blading materials Right – Effect of precipitation hardening temperature on stress corrosion CGRs (19).

2.3.4.6 *Environmental Factors Affecting SCC*

SCC of an alloy is typically the result of the existence of a particular chemical species in the service environment (39). An environment that causes SCC in one alloy may not necessarily cause SCC in another alloy hence there is no general pattern dictating if SCC will occur in a specific material/environment combination without first testing it. A change in environmental conditions may turn a seemingly harmless environment into one that causes failure due to SCC. Environmental parameters known to influence SCC crack growth rates in aqueous solutions include, but are not limited to (39):

- Temperature
- Pressure
- Solute species
- Solute concentration and activity
- pH
- Electrochemical potential
- Solution viscosity
- Stirring or mixing

A change in any of these parameters may result in either increasing or decreasing the crack propagation rate. If an adjustment to the bulk environment allows for the development of a critical SCC environment in the region of the crack tip, then crack propagation will result. It is widely accepted that the shielded environment at occluded sites, such as a crack tip, can vary considerably from the bulk environment (34, 39). A crack exposed to a neutral dilute sodium chloride environment may experience a drastic drop in pH in the range of 2 to 3. The chlorine concentration could also increase by as much as 10 times that of the bulk solution. This harsher crack-tip environment can accelerate both anodic SCC and hydrogen-embrittlement cracking (34). Crack propagation will stop if the bulk environment cannot maintain this localized highly corrosive crack tip environment.

Steam Turbine Service Environment

The environment in an operating steam turbine is complex and varies between stations. This complexity is further compounded by the transient nature of service conditions and difficulty in generalizing the distribution of steam moisture content and the exact location where condensation starts for all turbines (48). Turnbull et al. have conducted a review (49) of the existing knowledge of steam turbine operating conditions and its effects on environment assisted cracking. Subsequent research (48) has expanded on this with advances in the understanding of SCC and CF of steam turbine steels. The following is a summary of their findings:

Characteristics of service conditions

The temperature and pressure distribution in a steam turbine is complex and varies between machines. Furthermore, variations in these parameters exist in individual turbines during operation; especially during start-up and shutdown periods e.g. last row low pressure (LP) blades normally operate at around 40°C but can reach 150°C during transient states. As such, the prediction of where condensate starts to occur cannot be exact. The formation of the liquid film on turbine components upon condensation (phase transition zone) depends on the steam moisture content, chemical impurities, wettability, and speed of rotation of the film surface (50-52) SCC only occurs when condensate has formed and is more likely to occur in LP turbines than HP turbines.

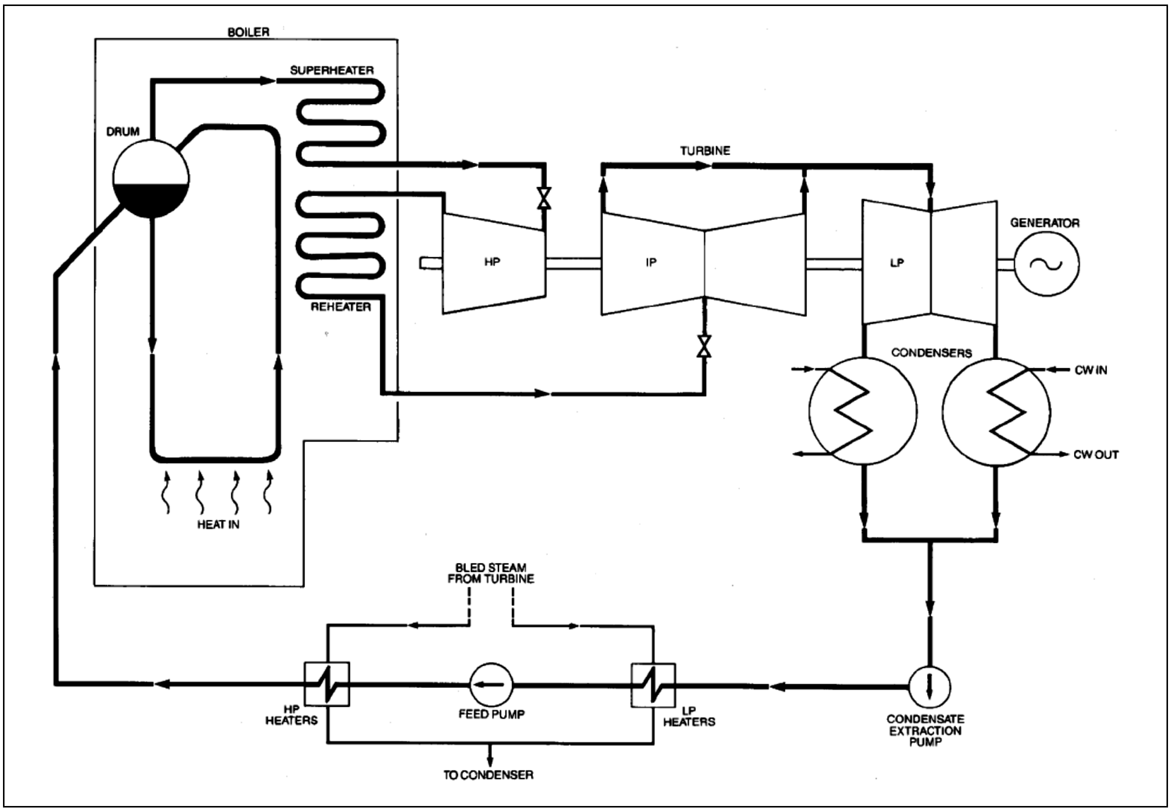

Figure 2-23: Rankine steam cycle in a fossil power plant (49).

Under normal operating conditions, power plant boiler and feedwater chemistry is strictly controlled. Chemical excursions can, however, lead to impurities in the feedwater which could have detrimental consequences for turbine components with regards to SCC initiation and propagation. Ingress of impurities could be due to deficiency of water treatment, leakage from the condenser; transients in water chemistry during start-up and shut-down periods; etc. Some of the impurities which can be present include sodium hydroxide, chlorides, sulphides, iron and copper (1, 49, 53). These impurities can make their way into the steam in numerous ways. The concentration of impurities present on the saturated metal surface is of prime concern. Efforts have been made to assess the water chemistry through modelling power plant operation (50) the results of which showed that the pH of the early condensate and liquid film is either neutral or slightly acidic which is lower than that of the inlet steam. This could be due to carryover of organic acids from the boilers (1). Chloride levels in the inlet steam are 2-3 parts per billion (ppb) while levels in the early condensate were approximately 100 ppb. The chloride concentration in the liquid film was found to be more variable but higher that the inlet steam.

Transient operating states can lead to poorly controlled steam chemistry and the ingress of gases such as oxygen. This is most likely to occur during outages when gland steam is no longer supplied and the condensate becomes air saturated. Start-up processes also lead to a temporary high level of oxygen. The structural complexity of the turbine means that air leaked into the turbine chamber takes longer to be removed with tests putting this time frame at a few hours after start-up. This may cause the corrosion potential to drop slowly to the low potential associated with on-load conditions. These results show that on-load conditions with strictly controlled inlet water chemistry present less of a risk of SCC when compared to transient and off-load states.

2.3.4.7 Mechanical Factors Affecting SCC

The mechanical aspects of SCC differ to the environmental or metallurgical factors in terms of its effects on various material/environment combinations. Where environmental and metallurgical factors are specific to a given material/environment combination, mechanical factors such as applied stresses, threshold stress intensities and stress-independent crack growth are common to a variety of materials (39).

Most structural engineering applications result in applied stresses which, although designed to be lower than the yield strength of the material, could be at a level sufficient to increase the local stress state at the tip of an advancing crack increasing susceptibility to SCC. If the crack initiation and growth process is allowed to continue, sudden structural failure is possible.

Application of Fracture Mechanics to SCC

Fracture mechanics is the study of a material’s ability to withstand stress in the presence of a flaw (26). It uses analytical methods to characterize the initiation and growth of cracks from pre-existing flaws in the structure. Due to the fracture process during SCC being brittle, stresses are below the yield strength of the material and cracks propagate mostly elastically, with local plasticity effects being minimal. This enables the use of linear elastic fracture mechanics (LEFM) to characterize SCC behavior in terms of the kinetics of sub-critical crack growth and the associated stress intensity at the crack tip in the opening mode, K_I. [For low-strength materials that form a significant plastic zone ahead of the crack, nonlinear fracture mechanics relationships must be used to calculate K (39).]

It has been experimentally shown that a unique relationship exists between stress intensity, K_I, and the SCC growth rate, for a given material/environment combination. Plotting K_I against the crack growth rate, da/dt, results in the curve seen in Figure 2-24. Many material/environment combinations display subcritical crack growth behavior characterized by a threshold and the three distinct stages (I, II, and III) in the curve.

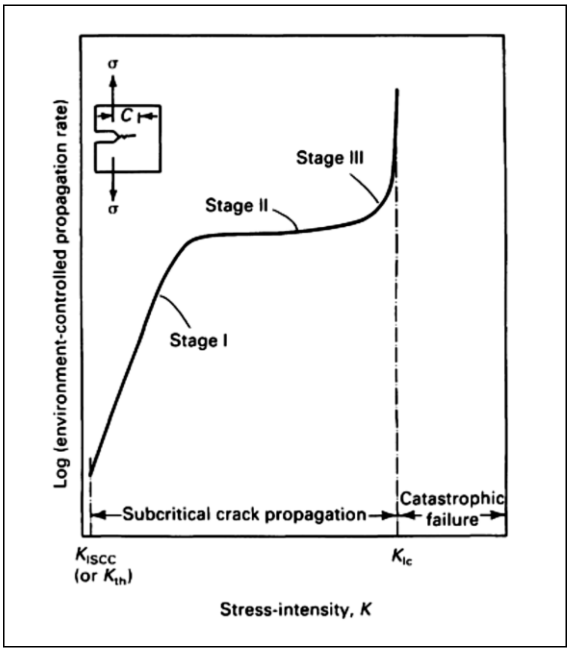

Figure 2-24: Relationship between stress intensity and crack growth rate for SCC (39).

The threshold stress intensity for SCC, K_{ISCC}, can be defined as the lower shelf value of stress intensity for which the smallest reliably measured crack growth rate can be detected. The existence of a true threshold does not appear to exist for all material/environment combinations however it does appear to hold true for titanium alloys and high-strength steels (2). The practical engineering significance of K_{ISCC} is the fact that below this stress intensity level, SCC growth rates usually fall below 10^{-10} m/s, which is low enough for the crack to be considered stationary. The K_{ISCC} level is determined by the composition and metallurgical condition of the alloy as well as by the environment (39).

The three stages in Figure 2-24 can be described as follows:

Stage I: At low stress intensity levels subcritical crack growth rate increases rapidly with a small increase in K. Changes in crack velocity of two orders of magnitude with minor changes in K are not uncommon. The K dependence of stage 1 is believed to be due to the rapid increase in transport of species into and out of the crack with increasing crack volume (39).

Stage II: At intermediate stress intensity levels, the crack propagation rate approaches some constant velocity that is relatively independent of the stress intensity. This "plateau velocity" is characteristic of many alloy-environment combinations. Environmental factors such as crack tip potential, corrosion rates, and pH affect crack velocity in this regime such that the limiting velocity is a function of crack tip corrosion rate, strain rate, and transport rate (39).

Stage III: In this stage, the rate of crack propagation exceeds the plateau velocity as the applied stress intensity level approaches the fracture toughness of the material, K_{IC}, and fast fracture occurs.

Crack Branching

SCC cracks do not always follow a singular propagation path. Secondary cracks branching off the main crack path are sometimes observed. Crack branching, also known as bifurcation, can be distinguished into two types: 1) microbranching and 2) macrobranching. Microbranching occurs when the crack front splits into several short cracks separated by distances the length of a grain diameter. Macrobranching involves the macroscopic crack separation into two or more diverging elements (2).

Carter (54) concluded that the criteria for SCC crack branching are constant crack velocity and a critical stress intensity. Constant crack velocity prior to crack branching was shown to be true by Clark et al. (55). They found that the stress distribution around the crack tip of a static crack is such that the maximum normal stress is significantly less along the crack plane compared to the planes inclined 60° to the crack tip. The advancement of the crack front is thus directed towards these higher stressed planes causing crack branching. The rapid acceleration during the initial growth of the crack will prevent branching of the crack during this period.

Constant velocity for crack branching can also be explained in terms of the "plateau velocity" seen in the curve of Figure 2-24. Due to crack growth in stage II being stress intensity-independent, any branches would have the same velocity and hence one sees crack branching in this region. This was proven experimentally where various steels were tested for SCC susceptibility with the results (54) showing that crack branching occurred when crack velocity was constant. In the materials where crack velocity was proportional to the applied stress, there was no crack branching.

It was also found that there existed a critical stress intensity, K_{Ib}, at which crack branching will occur which equals two to four times the threshold stress intensity, K_{ISCC}, for several high-strength steels (54).

3 Experimental Procedure

3.1 As received material

The material used to perform the experimental work in this study was supplied by Eskom in the form of a forged low pressure turbine blade manufactured from FV520B as seen in Figure 3-1. The length of the blade is approximately 1 meter. The thickness of the aerofoil increases through the length with the maximum thickness just ahead of the blade root. The blade was sectioned into multiple pieces such that the material could be optimized for the manufacture of the various specimens used in this study.

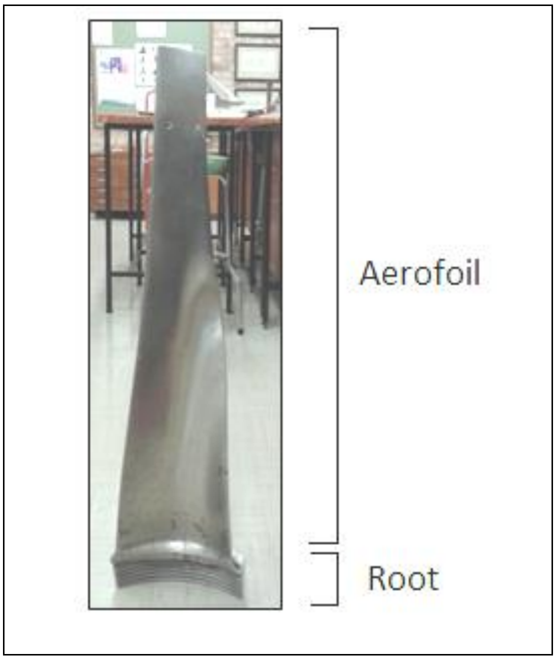

Figure 3-1: Low pressure turbine blade manufactured from FV520B supplied by Eskom.

3.2 Heat Treatment

The as received turbine blade was subjected to the following three step heat treatment as specified by the blade manufacturer (56):

1. Homogenization at 1020°C for 30 min followed by air cooling.
2. Solution treatment at 790°C for 2 hours followed by air cooling.
3. Precipitation hardening at 545°C for 6 hours followed by air cooling.

3.2.1 Modelling temperature evolution in turbine blade during heat treatment

A low pressure turbine blade has a complex geometry which is necessitated by its function. Due to this, the blade is not of a constant thickness. The aerofoil section has an increasing thickness down the length of the blade while the serrated blade root decreases in thickness from the first serration to the last. As such, the heat treatment regime of turbine blades needs to take into account the varying thickness in order to ensure that the entire blade is heated to the required temperature in the time allocated. Failure to do this would result in the blade consisting of an inhomogeneous microstructure at the thickest sections which could result in a deterioration of mechanical and stress corrosion properties in these parts.

An investigation into the effect of temperature evolution during heat treatment on blade thickness was performed. This was done using a finite difference approximation method and modelling the turbine blade as a flat plate with thickness equal to the thickest section in the blade.

Using the general heat equation:

$$\frac{}{} \qquad \frac{}{} \quad \text{where} \quad \frac{}{} \qquad \textbf{Equation-12}$$

T = Temperature
t = time
x = spatial variable (thickness of plate)
λ = Material Thermal Conductivity
ρ = Material Density
C_p = Material Specific Heat Capacity

and converting the two partial derivatives to finite difference approximations gives:

$$\frac{}{} \qquad \left[\frac{}{}\right] \qquad \textbf{Equation-13}$$

$$T(x, t + \Delta t) = T(x, t) + \Delta t\alpha\left[\frac{}{}\right] \qquad \textbf{Equation-14}$$

In numerical terms, we can discretize ‘x’ and ‘t’ such that:

$$x_i = i\Delta x,\ i=0,1,2\ldots$$

$$t_j \quad j\Delta t,\ j=0,1,2\ldots$$

Letting $T_{i,j}$ be the abbreviated notation to $T(x_i, t_j)$ Equation-13 becomes:

$$\frac{T_i \quad -T_i}{\Delta t} \qquad \frac{T_i \qquad 2T_{i,j}+T_i}{\Delta x}$$

Defining the parameter r as $r=\frac{}{}$

And Equation-14 then becomes:

$$\mathrm{T_i} \qquad \mathrm{rT_i} \qquad (1 \qquad)\mathrm{T_i} \quad \mathrm{rT_i}$$ **Equation-15**

Equation-15, referred to as an explicit formula, can be used to find one unknown value directly in terms of several other known values. However, due to the thermal conductivity, λ, and the specific heat capacity, C_p, being dependent on the temperature, this needs to be accounted for in the calculation. Temperature dependent functions for the thermal conductivity and specific heat capacity of stainless steel were therefore used (57):

$$\lambda = 14.6 + 1.27\mathrm{x}10^{-2}\mathrm{T}\ (\mathrm{W/m.K})$$ **Equation-16**

$$\mathrm{C_p} = 450 + 0.28\mathrm{T} - 2.91\mathrm{x}10^{-4}\mathrm{T}^2 + 1.34\mathrm{x}10^{-7}\mathrm{T}^3\ (\mathrm{J/kg.K})$$ **Equation-17**

where T is in (°C).

Microsoft Excel was used to perform the numerical simulation using the equations listed above. The turbine blade was modelled as a flat plate with thickness corresponding to the thickest section of the blade. The input parameters required for the model are as follows:

1.	Duration of heating	(s)
2.	Heat treatment temperature	(°C)
3.	Ambient temperature	(°C)
4.	Thickness of plate	(mm)

Other parameters such as the step size of both the time and spatial domain in the model can also be refined to improve the results obtained. One important assumption made to simplify the model is that the temperature of the plate surface is equal to the surrounding air in the furnace during heating up. The output of the model is a temperature-time plot showing the temperature evolution in the plate during heat treatment. Each curve in the graph represents the temperature profile at a certain distance (depth) from the surface of the plate as shown in Figures 4-1 to 4-3.

3.2.2 Selection of heat treatment temperatures

In order to evaluate the influence of heat treatment on the materials susceptibility to stress corrosion cracking (SCC), the heat treatment parameters needed to be varied for testing. Since the heat treatment regime of the blade consisted of three steps there were numerous ways in which these steps could be varied and tested (possibilities included variations in time and temperature in all steps). Although the results of these tests could prove valuable, limited time and material resources meant that the heat treatment variation had to be constricted. It was ultimately decided that the only variation in the heat treatment regime would be in the final step i.e. varying the precipitation hardening temperature and evaluating this variation on the SCC properties for FV520B.

Since the SCC properties of FV520B in chloride environments were not widely available in literature, its susceptibility was not known. However, it is documented that SCC is most likely to occur when the material is in its highest strength condition (8, 9). It was therefore decided that one of the heat treatments to be tested should be that which provides the highest strength in FV520B since this material condition would be the most susceptible to SCC if at all. The material manufacturer's data handbook (8) was used to determine the heat treatment condition which provided highest strength.

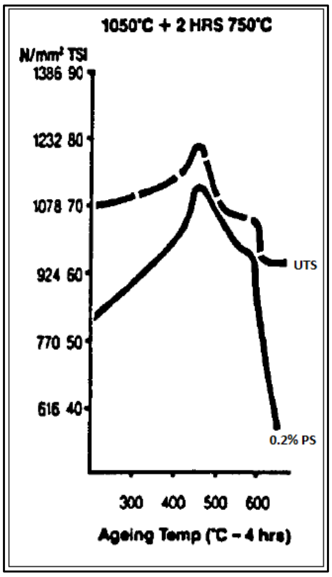

Figure 3-2: Ageing temperature vs. tensile strength and proof stress for FV520B (8).

Figure 3-2 shows the variation in mechanical strength properties with ageing temperature for FV520B. Although the homogenization and solution treatment temperatures used in producing the curves (1050°C and 750°C respectively) differed slightly from the heat treatment regime of the turbine blade (1020°C and 790°C), these small differences in temperature should not have any considerable effect in changing the overall shape of the curves. It can be seen from Figure 3-2 that the peak in both curves exists in the region of 430°C ageing temperature which corresponds to the temperature at which maximum secondary hardening takes place. This was confirmed by hardness measurements as seen in Figure 4-4. It was therefore decided that the final step in the heat treatment regime would be a variation in the precipitation hardening (ageing) temperature from 430°C to 600°C. This would ensure that the heat treatments incorporated the following:

1. The material in its highest strength state (430°C ageing temperature).
2. The original heat treatment of the turbine blade (545°C ageing temperature).
3. The effect of over aging the material (600°C ageing temperature).
4. The effect of a gradual increase in ageing temperature on the material microstructure, mechanical properties and SCC properties.

The final heat treatment matrix for testing was as follows:

Specimen	Homogenisation	Solution Treatment	PH Treatment
S430	1/2 hr @ 1020°C A/C	2 hrs @ 790°C A/C	6 hrs @ 430°C A/C
S450	1/2 hr @ 1020°C A/C	2 hrs @ 790°C A/C	6 hrs @ 450°C A/C
S470	1/2 hr @ 1020°C A/C	2 hrs @ 790°C A/C	6 hrs @ 470°C A/C
S500	1/2 hr @ 1020°C A/C	2 hrs @ 790°C A/C	6 hrs @ 500°C A/C
S545	1/2 hr @ 1020°C A/C	2 hrs @ 790°C A/C	6 hrs @ 545°C A/C
S600	1/2 hr @ 1020°C A/C	2 hrs @ 790°C A/C	6 hrs @ 600°C A/C

A/C = Air Cooled

Table 4: Heat treatment matrix for testing.

Specimens were coated in Foseco Isomol 100, a spirit-based coating, prior to heat treatment, to prevent excessive oxide layer formation and decarburization of the material. The specimens were heat treated in an electric box furnace with an external K-type thermocouple attached to get an accurate temperature reading of the specimens in the furnace. Once the specimens were removed from the furnace after the heat treatment, they were air cooled at room temperature and allowed to stand for approximately 24 hours before the next heat treatment step as stipulated in the material manufacturer's data handbook (8).

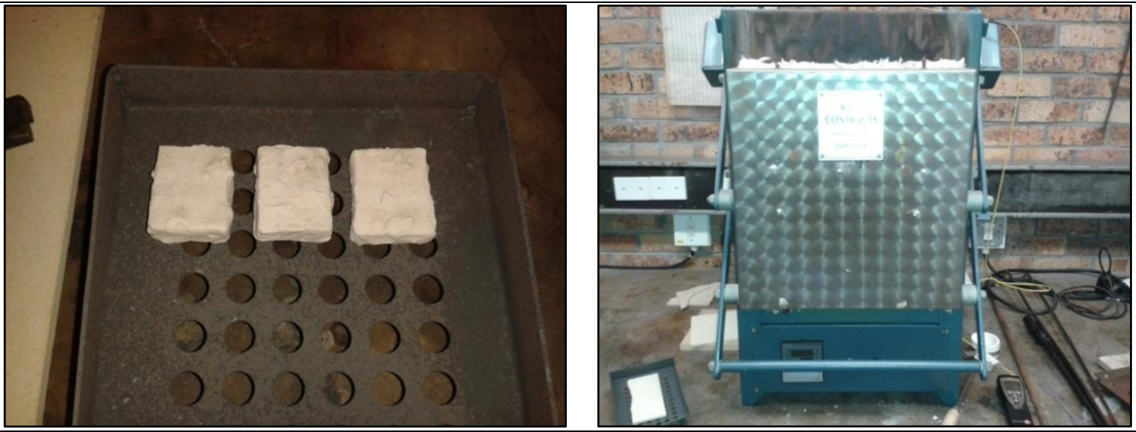

Figure 3-3: Specimens coated with Foseco Isomol 100 (left) and electric box furnace with external thermocouple (right).

3.3 Testing of Mechanical Properties

3.3.1 Hardness Testing

Hardness testing was conducted on all heat treatment conditions as stipulated in Table 4. Heat treated specimens were mounted in resin and ground to a 1200 grit finish. Vickers hardness (HV) testing in accordance with ASTM E92 (58) was completed on a Zwick/Roell macro-hardness testing machine using a 30 kg load. Each heat treated specimen was used to obtain 10 hardness measurements. The average hardness and standard deviation were calculated for each specimen.

3.3.2 Tensile testing

Round dumbell tensile specimens as shown in Figure 3-4 were machined and heat treated to all heat treatment conditions in Table 4. Tensile testing was carried out at Eskom's Rosherville testing facilities. Two tensile specimens per heat treatment were tested to failure in accordance with BS EN 10002-2001 (59) utilizing an Instron 5582 tensile testing machine. All tensile tests were conducted at room temperature.

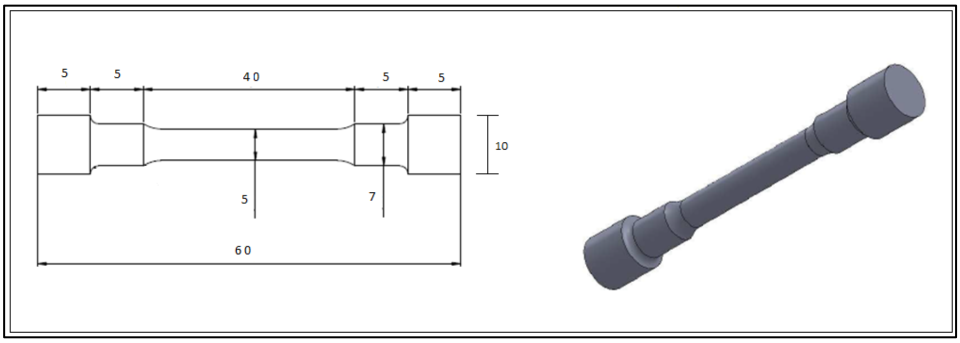

Figure 3-4: Tensile test specimen dimensions and isometric view.

3.4 Microstructural Characterization

Microstructural characterization was carried out to determine the effect of the variation in precipitation hardening temperature on the microstructure of FV520B. Various techniques were utilized to characterize the material. These included light microscopy, X-ray diffraction (XRD), scanning electron microscopy (SEM), carbide replica extraction, and transmission electron microscopy (TEM).

3.4.1 Specimen Preparation

The heat treated specimens were mounted with a hot press using Struers Polyfast mounting resin which contains graphite powder to ensure a conductive mount for usage in a SEM. The specimens were mechanically ground and polished using automatic specimen preparation machines. The specimen preparation steps are shown in Table 5.

Step	Surface	Suspension	Lubricant	Rotation (rpm)	Force (N)	Time (min)
Grind	SiC paper 800	-	Water	150	30	2-4
Grind	SiC paper 1200	-	Water	150	30	2-4
Polish	MD-Mol	3µm DiaDuo diamond suspension	-	150	20	12
Polish	MD-Nap	OP colloidal silica suspension	-	150	20	2

Table 5: Specimen preparation steps.

3.4.2 Light Microscopy

Polished specimens were etched in Villela's Reagent (5 ml hydrochloric acid, 1 g picric acid in 100 ml ethanol) and examined under bright field mode and Nomarski (differential interference contrast) mode using a Leica Reichert MeF3. General microstructural features such as grain boundaries, phase identification, inclusions and carbide segregation were evaluated.

3.4.3 Energy Dispersive X-ray Spectroscopy (EDS)

Energy Dispersive X-ray Spectroscopy is a chemical microanalysis technique used in conjunction with scanning electron microscopy (SEM). The technique uses an energy dispersive spectrometer to detect x-rays emitted from the specimen during bombardment by an electron beam thereby characterizing the elemental composition of the analysed volume (60).

When the specimen is bombarded by the SEM's electron beam, electrons are ejected from the atoms comprising the specimen's surface. The electron vacancies are filled by electrons from a higher energy state and an x-ray is emitted to balance the energy difference between the two electrons' states. The x-ray energy is characteristic of the element from which it was emitted (60). This energy is measured by the spectrometer and is further processed to give the elemental composition of the analysed volume.

Inclusion and precipitate content in FV520B stainless steel was analysed using EDS on a Nova NanoSEM 230 microscope. An accelerating voltage of 20 kV and a spot size of 4.5 were used in the analysis. Results are presented in section 4.3.3.

3.4.4 Dilatometry

Dilatometry is a thermo-analytical technique for the measurement of dimension changes in materials due to expansion or contraction over a controlled temperature regime with negligible specimen strain. In this case, dilatometry was performed to determine the phase transformation temperatures of FV520B i.e. the Ac_1 (austenite start) and Ac_3 (austenite finish) temperatures on heating, and the M_s (martensite start) and M_f (martensite finish) temperatures on cooling.

The dilatometry work was performed using a customised instrumented dilatometer at the Centre for Materials Engineering at UCT. The dilatometer specimen diameter and length were 6 mm and 44 mm respectively, in accordance with the reference specimen for the machine. The dilatometry software allowed for the heating rate to be varied. This reduced the time taken to perform the test as high heating rates were used when heating from room temperature. The heating rate was then lowered as the temperature approached the anticipated transformation temperatures so that more precise data points could be plotted to give more accurate transformation temperatures. A sample rate of 1 minute per data point was used. The specimens were heated to 800°C and held for 10 minutes before cooling. The cooling rate was kept constant when cooling down to room temperature using argon gas. An example of the heating and cooling regime used can be seen in Figure 3-5. The temperature was monitored using a K-type thermocouple which was attached to the specimen. The change in dimension of the specimen during the heating and cooling regime was recorded by the linearly variable differential transducer (LVDT).

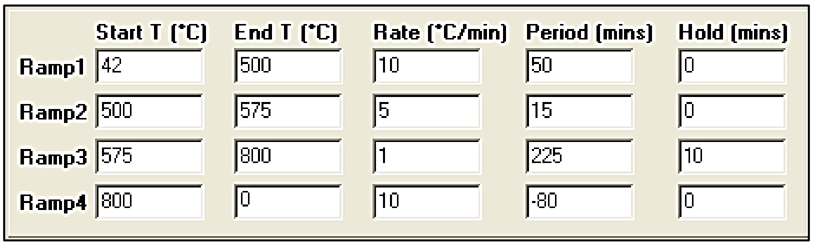

	Start T (°C)	End T (°C)	Rate (°C/min)	Period (mins)	Hold (mins)
Ramp1	42	500	10	50	0
Ramp2	500	575	5	15	0
Ramp3	575	800	1	225	10
Ramp4	800	0	10	-80	0

Figure 3-5: Dilatometry heating and cooling regime used.

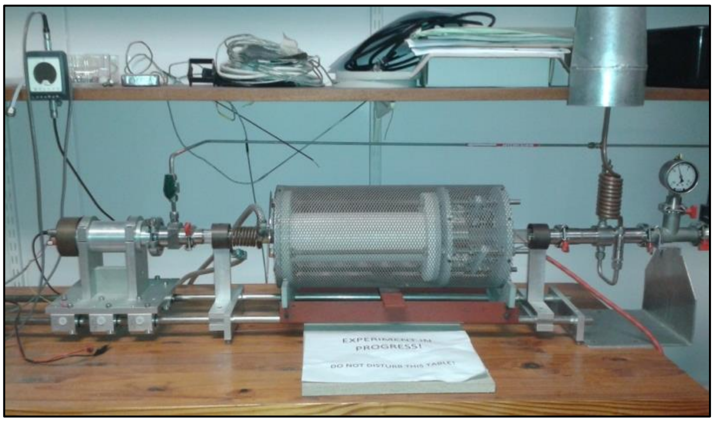

Figure 3-6: Dilatometer setup used.

3.4.5 X-Ray Diffraction (XRD)

The technique of x-ray diffraction (XRD) was used to detect and determine the microstructural phases and corresponding volume fractions within FV520B in the different heat treated specimens. The precipitation hardening process will temper the martensitic matrix formed after solution treatment. A previous study (5) performed on FV520B heat treated to the standard heat treatment conditions seen in Table 2 showed that tempering can sometimes cause a reversion of martensite to austenite in FV520B, the amount of which can be significant as the temper temperature increases. XRD was therefore used to determine the presence and quantities of reverted austenite as a result of this particular heat treatment regime of FV520B.

Specimens heat treated to the six conditions listed in Table 4 as well as two additional specimens, one undergoing homogenisation only and the other homogenisation and solution treatment, were prepared for XRD analysis. The samples were mounted in resin, grinded and polished to a 3 μm finish according to Table 5. Polished specimens were subsequently removed from the resin due to the specimen size restrictions of the XRD equipment.

XRD analysis was performed at iThemba Laboratories in Stellenbosch utilizing a Bruker D8 Discover High – Resolution Diffractometer with Copper Kα radiation. X-ray intensities diffracting through Bragg angles (2θ) of 20°-100° were recorded. The spectra from the XRD analysis of the heat treated specimens are presented in Figures 4-19 to 4-26 respectively showing the variation in X-ray intensity as a function of the Bragg angle (2θ).

3.4.5.1 Quantitative Phase Analysis

The principle behind quantitative analysis by diffraction is due to the relation between the intensity of the diffraction pattern of a particular phase in a mixture and the concentration of that phase in the mixture (61). Many methods have been developed over the years for quantitative phase analysis. The software used for the analysis in this study was MAUD – Material Analysis Using Diffraction. This software is based on the Rietveld refinement method.

The Rietveld method is based on a least-squares fit between a measured diffraction spectrum and a simulated X-ray-diffraction pattern. The simulated XRD pattern is calculated based on various parameters, including crystal-structure parameters of each component phase, a scale factor for each phase to adjust the relative intensities of the reflections, parameters describing the peak profile and the background, etc. (62). Once the diffraction pattern is simulated, it is refined to match the measured experimental diffraction spectrum.

The results from the quantitative phase analysis using MAUD software can be seen in Table 8.

3.4.6 Transmission Electron Microscopy (TEM)

TEM is a characterisation technique in which a high energy beam of electrons is emitted through a very thin specimen. The interactions between the electrons and the material can be used to observe features of interest in the specimen. Due to the wavelength of electrons being much smaller than that of light, the optimal resolution attainable for TEM images reveals even the finest details of the microstructure - in some cases even individual atoms.

TEM specimens were prepared to determine if there was any appreciable chromium depletion across prior austenite grain boundaries (PAGB's) due to the different heat treatments and the extent thereof. TEM was also used to characterize the type of precipitates found at the different temper temperatures.

TEM analysis requires thin electron transparent specimens in the order of 100 nm or less in thickness. In this study, two different specimen preparation techniques were employed. Specimens were prepared using (a) the focused ion beam technique and (b) carbon replica extraction.

3.4.6.1 Focused-Ion Beam Technique

Focused-ion beam (FIB) specimen preparation was conducted in a Helios NanoLab FIB-SEM. Ga^+ ions are used to mill material from the bulk specimen in a controlled fashion to produce thin TEM lamellae approximately 5x5x0.1 µm in size. The first stage in the process was choosing the area of interest in the bulk specimen which was done in normal SEM mode. Because TEM specimens containing PAGB's were required, the etched surface of the bulk specimen was scanned for PAGB's in the hope that grain boundaries on the surface would extend more or less perpendicular into the specimen. Choosing a PAGB on the etched surface was done purely based on visual judgement and the only way to verify if it extended into the material was by milling. If the PAGB did not extend into the material, the process had to be repeated, which proved time-consuming. Once a PAGB was chosen on the etched surface the procedure for preparing the samples are as shown in Figure 3-7. In the first step a layer of carbon is deposited onto the surface at the chosen area for protection against the rough milling steps to follow. This was followed by the milling of trenches on either side of the carbon layer. The probe was then attached to the sample before the lamella was cut free and removed from the bulk. The micro-manipulator was then used to transport the lamella to the TEM-grid where it was attached using carbon deposition. The final step involved polishing the lamella down to less than 100 nm.

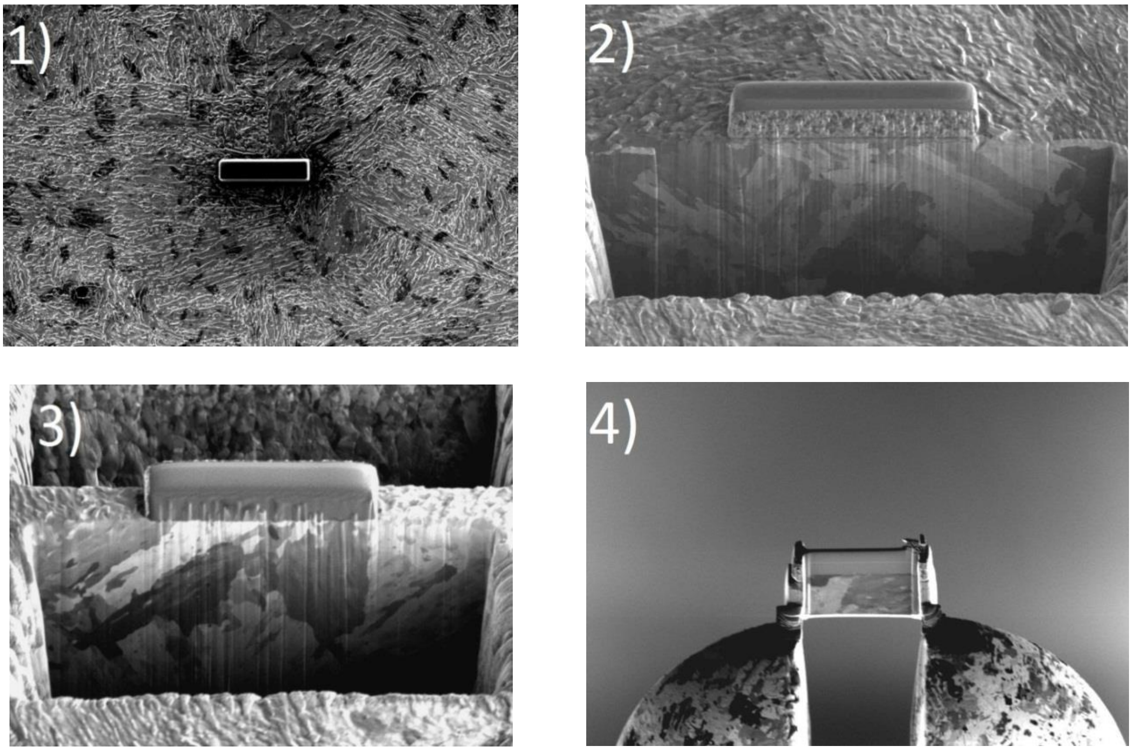

Figure 3-7: Stages of FIB-SEM specimen preparation: 1) Carbon Deposition; 2) Milling of trench on one side of carbon layer; 3) Milling of trench on other side; 4) Specimen attached to TEM grid and polished down to 100 nm with grain boundary clearly visible.

3.4.6.2 Carbon Replica Extraction

Characterization of the precipitates formed during the test heat treatments was done using the carbon replica extraction technique and subsequent TEM analysis. There are many techniques available for making an extraction replica of the particles embedded in the material matrix. The technique used in this study was the Direct Carbon Extraction Replica technique, also called the Negative Carbon Extraction Replica technique.

Heat treated samples were polished to a 1 µm finish. The samples were then etched with Vilella's reagent to expose the carbide precipitates. The length of exposure to the etchant varied between the different heat treated specimens dependent upon temper temperature. The higher the temper temperature the quicker the response will be to the etchant. Samples were then placed in a vacuum environment where carbon was coated onto the etched surface to a thickness of approximately 20 nm. A scalpel was then used to score the coated sample surface in a grid pattern with individual squares measuring approximately 2 mm x 2 mm. The scored samples were then placed in the etchant once more and left in until the scored carbon films detached completely from the surface. The average duration of the second etch was 45-60 minutes for the carbon films to detach from the surface. The carbon films were collected using tweezers and cleaned in a H_2O-10vol% methanol solution. The carbon films which now contain precipitates were then carefully collected onto 200-mesh copper TEM grids and allowed to dry before examination in the TEM. The TEM samples were analysed using a JEOL JEM 2100 (Lab6) and JEOL Double Cs-corrected Atomic Resolution Microscope (ARM) 200F.

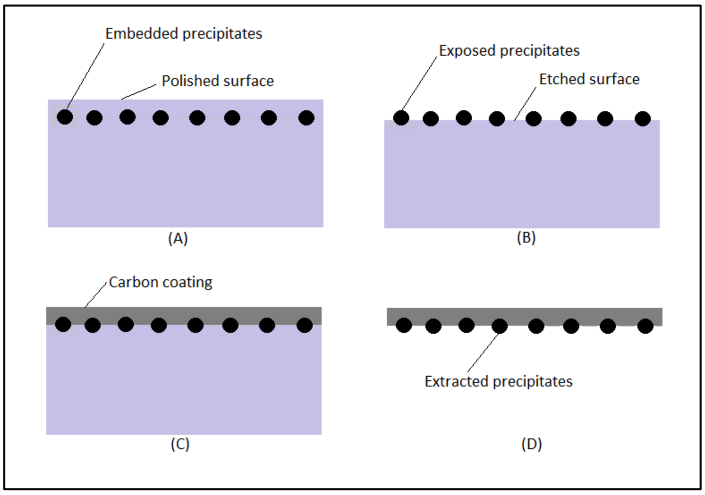

Figure 3-8: The carbon replica extraction process.

3.4.6.3 Energy Filtered Transmission Electron Microscopy (EFTEM)

EFTEM is a technique used in a TEM to create elemental distribution maps by irradiating a very thin specimen with a broad beam of high-energy primary electrons. Most of the electrons will easily pass through the specimen but some will interact with the specimen resulting in elastic and inelastic scattering. Inelastic scattering will result in both a loss of energy and a change in momentum which, in the case of inner shell ionization, is then used to characterize the element that the electron interacted with (63). The electrons of a specific energy can be filtered out using an adjustable slit and an image can be formed through the detection of these electrons. In this way, elemental mappings are generated in a relatively fast and easy manner. EFTEM was utilized to create elemental distribution maps of the thin specimens prepared using the focused ion beam technique to investigate the presence of chromium-rich precipitates along the prior austenite grain boundaries in the various heat treatment conditions. These results can be seen in section 4.3.6.1.

3.4.6.4 High Angle Annular Dark-Field (HAADF) Imaging

HAADF imaging is a technique which utilises the high angle Rutherford forward scattering electrons where the interaction is between these electrons and the atomic nuclei in the specimen. The scattering phenomenon is strongly dependent on the atomic number, Z, of the elements in the specimen. This technique thus enables compositional contrasts with greater sensitivity and faster image collection and recording than X-ray imaging (64). HAADF imaging is conducted on a scanning transmission electron microscope (STEM) equipped with an annular dark-field detector. The scattering generated when the focused beam moves across the specimen is due to the interaction between the Rutherford electrons and the specimen and will vary across the specimen. This high-angle scattering which is detected by the annular dark-field detector is then used to form the image of the specimen. HAADF imaging was conducted on focused ion beam prepared specimens to determine via EDS if chromium depletion was evident in the areas adjacent to prior austenite grain boundaries. The results can be seen in section 4.3.6.1. HAADF imaging was also done on the carbon replica extraction specimens to investigate the presence of chromium rich precipitates across prior austenite grain boundaries. These results can be seen in section 4.3.6.2.

3.5 Stress Corrosion Testing

Stress-corrosion cracking testing is usually performed either to determine the best material for a particular application or to compare the relative behaviours of variations in material and environment (39). The purpose of this study was the latter. As such, two types of SCC test methods were used in this study:

a) Susceptibility testing using smooth, statically loaded specimens;
b) Threshold stress intensity testing using precracked, statically loaded specimens.

A smooth specimen simulates a structure ideal in design and construction while a precracked specimen represents a structure containing the worst kind of flaw. Structures operating in typical service environments would usually behave a manner lying somewhere in between these two extremes. It would therefore prove fruitful to evaluate both types of specimens to establish the SCC characteristics of a test material under the two limiting conditions (2). Both SCC test techniques will be discussed in detail in the sections to follow.

3.5.1 SCC Environment and Test Setup

3.5.1.1 SCC Environment

The complexity and transient nature of service conditions presents challenges in trying to simulate a steam turbine operating environment accurately, however, there has been research conducted which looked at exactly this (1, 48, 49). The results have shown that some of the impurities which can be present in the condensate include sodium hydroxide, chlorides, sulphides, iron and copper which pose a genuine risk for corrosion-related failure.

It was not the intent to try to simulate steam turbine operating conditions in this study. However, an understanding of what those conditions are, helped in selecting a test environment which would provide meaningful results. As such, it was decided that a 3.5% sodium chloride solution would be used for the following reasons:

1. Sodium and chlorides are known to be present in the steam turbine environment.
2. A suitably aggressive test environment was required to accelerate SCC testing times in order to obtain the results within the timeframe of the project.
3. There have been numerous studies (9, 11, 65-68) which have been conducted using sodium chloride as a SCC test environment therefore results can be compared.
4. It is a relatively simple solution to make-up in a laboratory.

The test solution was prepared using analytical grade reagents and distilled water. The solution was maintained at a test temperature of 90±2°C which corresponds to early condensation and the formation of a condensate film in a steam turbine (10). The solution was aerated and would be representative of transient or off-load conditions where there is oxygen exposure in a steam turbine thus being a more conservative test environment. The test solution was refreshed weekly. Solution temperature and pH were monitored daily.

3.5.1.2 SCC test setup

The experimental setup, seen in Figure 3-9, consisted of a 10 L round bottom flask containing the test solution maintained at the test temperature of 90±2°C by a heating mantle. The concentration of the test solution was maintained constant at 3.5% NaCl with the aid of a reflux condenser. Water in a tank maintained at ambient conditions was pumped through the reflux condenser thereby condensing the steam from the test solution. In this way the concentration of the test solution was kept constant. The water from the reflux condenser then flowed back into the tank in a closed loop. The difference in temperature between the steam and the ambient water from the tank was sufficient to cause condensation.

Figure 3-9: Experimental setup for SCC testing.

3.5.2 SCC Susceptibility Testing

Accelerated SCC susceptibility testing was performed with plastically deformed U-bend specimens in accordance with ASTM G30-97 (69) to detect large differences in the SCC resistance of FV520B heat treated to several conditions in the test environment. U-bend specimens were selected due to their simplicity and the ability to manufacture multiple specimens easily and economically. Specimens are self-stressed with a fixed deflection and completely immersed in the test environment. U-bend specimens contain both elastic and plastic strain and may be used to test any material sufficiently ductile to be formed into the U-shape without cracking.

3.5.2.1 Specimen Preparation

U-bend SCC test specimens were manufactured in accordance with ASTM G30-97 (69). The U-bend specimen is a rectangular strip bent 180° around a predetermined radius and maintained in this plastically deformed state for the duration of the test (39). Various methods may be used to maintain the applied stress in the specimen. The method used in this study was by means of a bolt assembly.

U-bend specimens were manufactured from the aerofoil section of the turbine blade. Rectangular plate specimens were machined to the dimensions seen in Figure 3-10. Specimen dimensions were chosen to optimise the limited material available. Due to the high strengths achieved in the different heat treatment conditions, specimen thickness was kept to a minimum to enable the specimens to be bent into the final U-configuration without difficulty. A specimen thickness of 1 mm was thus used. Prior to bending, machined specimens were heat treated to the conditions to be tested. Heat treatment in an electric box furnace produced a thin oxide layer on the specimens. The specimens were therefore ground and polished to a smooth surface finish. The specimen surfaces were then measured using a profilometer to ensure a final surface finish of better than 0.76 μm as stated in ASTM G30-97 (69). Specimens were marked at the corners according to their heat treatment condition.

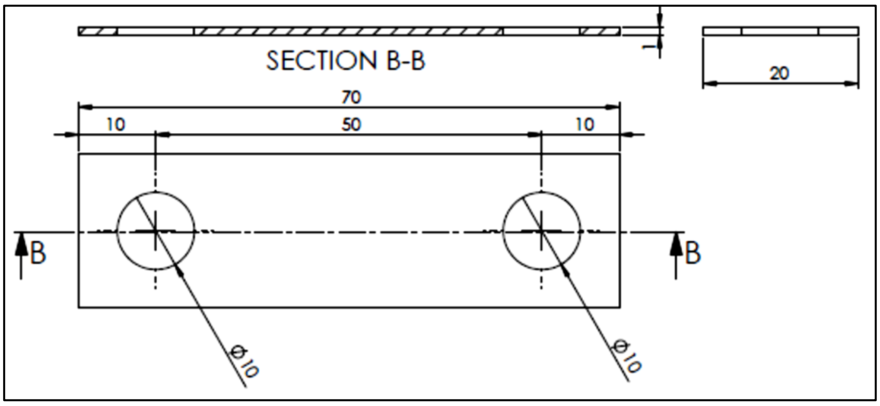

Figure 3-10: U-bend specimen dimensions (17).

Specimens were stressed using a two stage stressing method. Two-stage stressing involves first forming the approximate U-shape, and then allowing the elastic strain to relax completely before the second and final stage of test stress is applied. The first stage of stressing the specimen was performed in a 200 kN Zwick tensile testing machine fitted with a 3-point bending rig, as seen in Figure 3-11. To protect the highly polished surface finish of the specimens, thin soft cotton material was placed under the specimen to prevent severe scratching during the bending operation. The specimen was carefully positioned such that the mandrel would make contact with it at the centre position. This ensured that the holes would align for final assembly with the bolt. The mandrel used to form the U-shape was 10 mm in diameter. The mandrel was incrementally lowered onto the specimen until the specimen deformed by the required amount. After the mandrel was raised, the specimen was removed from the rig and allowed to elastically relax.

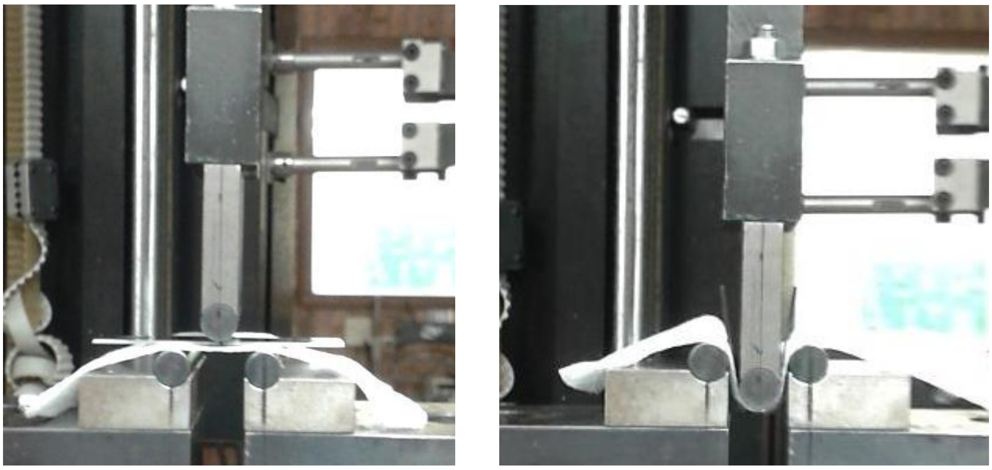

Figure 3-11: First stage of bending specimen using 3-point bending rig.

The second stage of stressing was done using a bolt, nut and plastic washers as seen in Figure 3-12. The stainless steel bolt and nut were coated with a neoprene primer paint to electrically isolate the specimen and prevent crevice corrosion. Insulating washers fabricated from polytetrafluoroethylene (PTFE) were used to provide further isolation between bolt and nut and the specimen. The bolt was tightened until the legs of the U-bend specimen were parallel to each other. The distance between the legs was measured and kept constant for all specimens.

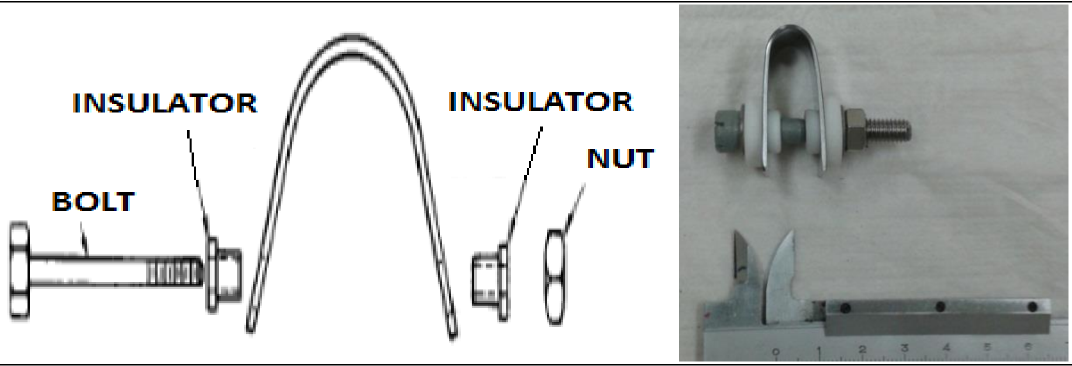

Figure 3-12: Left - Second stage of bending specimen using bolt, nut and PTFE washers (69); Right - Image of fully assembled U-bend specimen.

3.5.2.2 Test Procedure

Exposure to test environment

U-bend testing was conducted in batches. Each batch contained one specimen representing each of the six heat treatment conditions listed in Table 4. Prior to exposure to the test environment, assembled U-bend specimens were degreased ultrasonically and inspected in a stereo microscope at a magnification of 5x for cracks. After confirmation of the absence of cracks, specimens were immersed in the test environment described in section 3.5.1. Due to the large size (10 L) of the round bottom flask used, the solution volume to sample surface area ratio was more than adequate.

Inspection of test specimens

Specimens were periodically removed from the test solution and examined under the stereo microscope at 5x magnification for crack initiation and growth. Specimens were handled with clean nitrile gloves and inspected as is, without performing any cleaning operations on them. Inspection times were kept as short as possible and the frequency of inspections was as follows:

a) Twice a day for the first 7 days;
b) Daily for the following 7 days;
c) Every 48 hours for the following 7 days;
d) And weekly thereafter.

All inspection times were recorded precisely to obtain accurate time-to-failure results. Once crack initiation was confirmed in a specimen, the time was recorded and the specimen returned to the test solution for further crack growth. Specimens were only removed permanently from the test solution after crack propagation resulted to complete failure of the specimen. After failure, test specimens were examined optically using a Leica DFC 280 stereo microscope. Thereafter, a rust removing solution was prepared using Surtec 414 Neutral Activator in which test specimens were ultrasonically cleaned to remove all corrosion products from the fracture surface. Cleaned fracture surfaces were examined in a Zeiss/Leo 1450 scanning electron microscope.

3.5.2.3 Data Analysis

Time-to-failure was defined as the time at which first crack initiation was seen in a test specimen. This time was recorded for all test specimens when cracking occurred. Results were compared between the different heat treated specimens of each batch as well as specimens with the same heat treatment condition between batches. The results can be seen in Table 9.

Fractography was performed on the U-bend fracture surfaces to determine the mode of cracking. Hi-resolution SEM images were taken of the fracture surfaces of the test specimens and qualitative fractographic analysis was performed based on the images taken. The SEM images of the fracture surfaces can be seen in Figures 4-47 to 4-55.

3.5.3 SCC Threshold Stress Intensity Testing

Threshold stress intensity testing was conducted in accordance with ASTM E1681-03 (70) using precracked SCC specimens. A precracked SCC test specimen removes the uncertainties associated with growth of a corrosion pit to initiate cracking. It also allows for the use of fracture mechanics in analysing the stress distribution in the specimen (2). Precracked specimen configurations are usually categorised according to how the stress intensity changes with crack extension i.e. increasing, decreasing or constant stress intensity. Since the purpose of this test was to determine the threshold stress intensity and crack growth rate for SCC, a precracked specimen in which the stress intensity decreases with crack extension was chosen. This type of configuration can be further divided into constant load or constant deflection type specimens. To eliminate the need for elaborate and expensive experimental test rigs, a constant deflection type specimen was selected.

With a constant deflection precracked specimen, also known as a “crackline-loaded single-edge-cracked plate specimen” (2), the crack mouth opening displacement, measured along the load line, is kept constant, usually by some external device such as a bolt or wedge. As such, it is also referred to as a wedge open loading (WOL) specimen. When this specimen is exposed to the corrosive environment, the load and consequently the stress intensity at the crack tip, decrease as the crack grows. The stress intensity will decrease from the initial applied value, K_{I0}, to the threshold stress intensity for SCC, K_{ISCC}. The applied initial stress intensity usually exceeds the threshold stress intensity thus enabling crack growth to initiate fairly quickly. However, if no prior knowledge of K_{ISCC} is known and K_{I0} is applied very close to the threshold level, prolonged testing times may be required to achieve appreciable crack growth.

The WOL specimen is loaded to the required K_{I0} level by tightening a bolt against a reaction pin. As such, each specimen is loaded individually in a compact self-contained assembly. The advantages of this are:

1. It allows multiple specimens to be tested simultaneously thus reducing testing times.
2. It negates the need for expensive loading rigs thereby reducing testing costs.

3.5.3.1 Specimen Preparation

Bolt loaded WOL specimens were manufactured from root and aerofoil sections of a LP turbine blade. Specimen dimensions were chosen in order to meet the requirements of ASTM E1681-03 and can be seen in Figure 3-13. The notch in the specimen was cut by electric discharge machining (EDM) to increase dimensional accuracy. Bolt holes were drilled and tapped from both sides of the machined notch to aid in fatigue precracking (to be discussed in Section 3.5.3.2.). The loading bolt and reaction pin were manufactured from FV520B to prevent galvanic corrosion during testing. Specimens were heat treated to the required conditions in Table 4 prior to final surface preparation. Grinding and polishing was performed to produce a 1 µm surface finish on the specimen surfaces. Polished specimens were cleaned ultrasonically prior to fatigue precracking and loading.

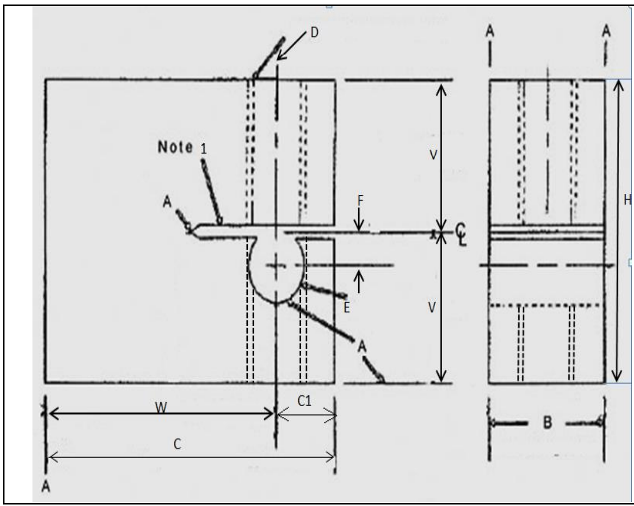

W = 28
H = 27
B = 11
V = 13.5
C = 35
D = M6 threaded
E = 7 diameter
F = 2.8
C1 = 7
Note 1: Notch length = 14, notch width = 1.6

Figure 3-13: Bolt-loaded WOL specimen dimensions (17).

3.5.3.2 Test Procedure

Fatigue Precracking

The machined notch cut using standard workshop methods is not sharp enough to allow for reasonably fast crack initiation. Therefore, a precrack is introduced at the notch tip to decrease the time needed to initiate a SCC crack. The precrack is usually grown by fatiguing the specimen under cyclic loading. The bolt loaded WOL specimens were fatigue precracked in an ESH fatigue testing machine. Specimens were fastened in the fatigue testing machine using custom manufactured jigs with threaded rods. The rods were threaded into the specimen bolt holes from opposite sides thus applying a tensile fatigue load to the specimen as seen in Figure 3-14. The load ratio used was $R=P_{min}/P_{max}= 0.1$. Due to the high strength levels of the specimens, a force-shedding (K-decreasing) method (71) was used to keep stress intensity during fatiguing below 60% of the expected K_{ISCC} value. The maximum applied stress intensity, K_{max}, used during precracking did not exceed 20 MPa√m, decreasing stepwise as the precrack grew. The precrack lengths were measured on both sides of each specimen using a Leica DFC 280 stereo microscope and the average length, a_0, calculated.

The stress intensity was calculated from (72):

$$K = \frac{P\sqrt{a}}{BW}\left[30.96 - 195.8\left(\frac{a}{W}\right) + 730.6\left(\frac{a}{W}\right)^2 - 1186.3\left(\frac{a}{W}\right)^3 + 754.6\left(\frac{a}{W}\right)^4\right] \qquad \textbf{Equation-18}$$

where K = stress intensity factor
B = specimen thickness
P = applied load
a = crack length (measured from the load line)
W = specimen width

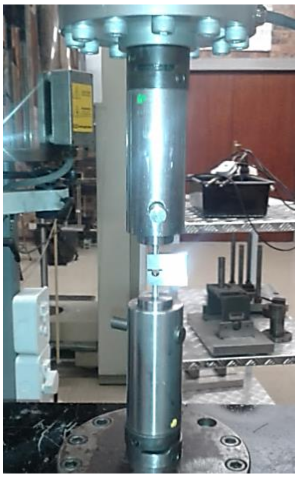

Figure 3-14: Fatigue precracking of WOL specimen.

Loading of specimens

In order to promote crack growth from the existing precrack, the WOL specimen is loaded to the predetermined initial applied stress intensity, K_{I0}, by means of tightening a bolt against a loading reaction pin such that the crack mouth opening displacement (CMOD) increases. The K_{I0} values were determined using the tensile strength data as well as SCC testing data for similar materials such as 17-4 PH stainless steel and varied according to the heat treatment condition.

The CMOD is related to the applied stress intensity by means of a compliance equation for the specific specimen geometry used (72):

$$\left(\frac{10}{}\right)\sqrt{a}\left[\frac{6\left(\frac{0}{}\right)}{3\left(\frac{0}{}\right)}\right] \qquad \textbf{Equation-19}$$

where E = Elastic modulus
a_0 = precrack length

$$\left(\frac{}{}\right) \quad 0.\ 6\left(\frac{}{}\right) - 195.8\left(\frac{}{}\right) \quad 730.6\left(\frac{}{}\right) \quad 1186.3\left(\frac{}{}\right) \quad 754.6\left(\frac{}{}\right)$$

$$\exp\left[4.495 \quad 16.130\left(\frac{}{}\right) + 63.838\left(\frac{}{}\right) \quad 89.125\left(\frac{}{}\right) \quad 6.\ 15\left(\frac{}{}\right)\ \right]$$

Precracked WOL specimens were fitted with knife edges on the top face to aid in CMOD measurements. Each specimen was then taped with thread tape below the load line creating a “dam” within the notch. This was done to enable some test solution to be pipetted into the notch prior to loading so that the notch and precrack are exposed to the test environment during loading. The specimen was then gripped in a vice and a calibrated clip gauge attached to the knife edges. The bolt was then tightened against the reaction pin opening the crack mouth. Each specimen was loaded to the calculated V_0, thus applying the predetermined stress intensity to the precrack tip. The time at which loading was completed was recorded representing the start of testing. The thread tape was then removed and each specimen immediately placed into the test solution. Loaded WOL specimens were fully immersed in the test solution during the test.

Inspection of test specimens

Specimens were removed periodically to measure crack growth. Specimens were handled with clean nitrile gloves and inspected as is, without performing any cleaning operations on them. Crack growth was measured using a Leica DFC 280 stereo microscope with Leica software. Inspection times were kept as short as possible and the frequency of inspections was as follows:

a) Twice a day for the first 7 days;
b) Daily for the following 7 days;
c) Every 48 hours for the following 7 days;
d) And weekly thereafter.

Crack lengths were measured on both sides of each specimen with the average taken for calculation purposes. All inspection times were recorded precisely to obtain accurate crack growth rate results.

Test termination

Specimens were permanently removed from the test solution when the crack growth rate was less than 10^{-9} m/s. The test termination time was recorded. The final crack lengths were measured on both sides of each specimen. Knife edges were refitted to the specimens and the change in CMOD, ΔV_T, was measured from the loaded to the unloaded state by removing the bolt. The specimens were then installed in the fatigue testing machine with the clip gauge attached and loaded to the measured change in CMOD, ΔV_T. The corresponding load (P_f) was recorded to be used to calculate K_{ISCC}.

The specimens were then fractured completely for examination of the fracture surfaces. Fractured pieces were ultrasonically cleaned to remove all corrosion products. Measurements of the final crack length were made using the stereo microscope, which was the average of five equi-spaced measurements across the thickness of the specimen. Fracture surfaces were then analysed in a Nova NanoSEM electron microscope.

3.5.3.3 Data Analysis

Since no direct measurement of the bolt load was possible during the test, compliance equations were used to calculate the stress intensity factor as a function of crack length and instantaneous load from (72):

$$\mathrm{P_i} = \left[\left(\frac{\mathrm{a_0}}{\mathrm{a_i}}\right)\left(\frac{\mathrm{a_i+C_1}}{\mathrm{a_0+C_1}}\right)\right]\frac{\mathrm{EBV_0}}{\mathrm{C_6}\left(\frac{\mathrm{a_i}}{\mathrm{W}}\right)}$$ **Equation-20**

where
P_i = instantaneous load
a_0 = initial crack length measured from load line
a_i = instantaneous crack length measured from load line
B = specimen thickness
W = specimen width
C_1 = distance as defined in Figure 3-13

The instantaneous stress intensity factor, K_{If}, was calculated from Equation-18 using the instantaneous load from Equation-20. The measured final load, P_f, together with the measured final crack lengths were then used to calculate the threshold stress intensity factor, K_{ISCC}.

The calculated threshold stress intensity factor, K_{ISCC}, is valid if plane strain conditions are present at the crack tip. Specific requirements relating to specimen dimensions and crack growth must be met in order to attain plane strain conditions:

$B, a, (W\text{-}a) \geq 2.5\left(\frac{KISCC}{\sigma y}\right)^2$, where σ_y is the 0.2% yield strength of the specimen.

4 Results

4.1 Heat treatment temperature evolution modelling

The output of the heat treatment temperature evolution model is a temperature-time plot showing the temperature evolution in the plate during heat treatment. Each curve in the graph represents the temperature profile at a certain distance (depth) from the surface of the plate. The thickness of the plate was taken as 40 mm corresponding to the thickest section measured in the turbine blade. The three heat treatment steps performed on the turbine blade by the manufacturer (56) were modelled:

Step 1: 1020°C for 30 min followed by air cooling.
Step 2: 790°C for 2 hours followed by air cooling.
Step 3: 545°C for 6 hours followed by air cooling.

The time-temperature plots for the three heat treatment steps modelled can be seen below:

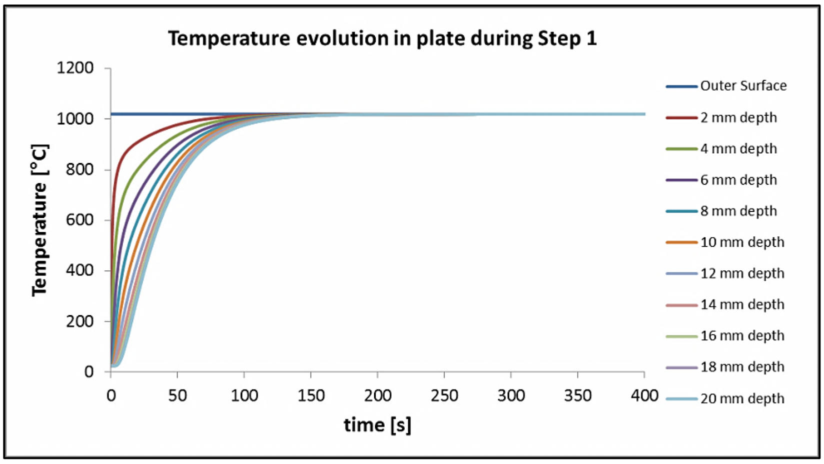

Figure 4-1: Temperature evolution during heat treatment Step 1.

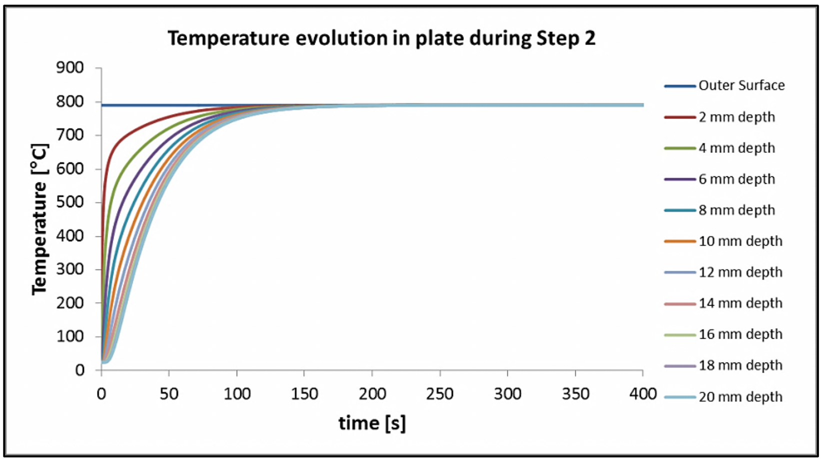

Figure 4-2: Temperature evolution during heat treatment Step 2.

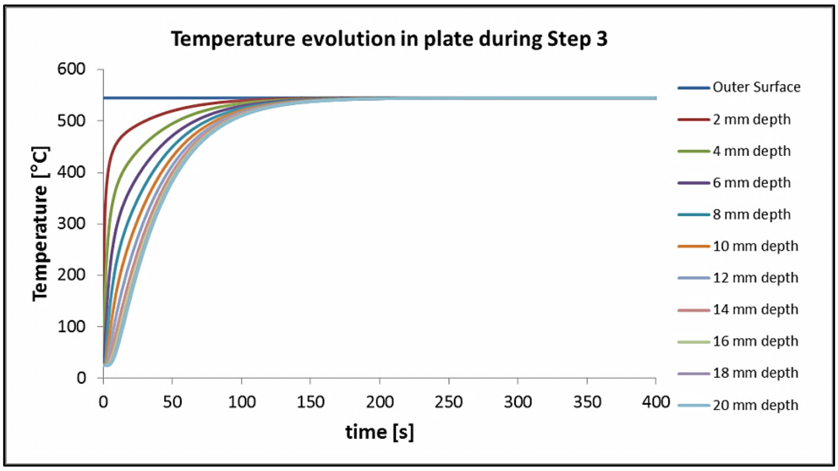

Figure 4-3: Temperature evolution during heat treatment Step 3.

The results from the simulation show that the entire plate will reach the desired heat treatment temperature within the time allocated in all three heat treatment steps:

For Step 1, the middle of the plate (at 20 mm depth from surface) will reach 1020°C in 157 seconds (2.62 minutes).

For Step 2, the middle of the plate will reach 790°C in 226 seconds (3.76 minutes).

For Step 3, the middle of the plate will reach 545°C in 235 seconds (3.92 minutes).

Each heat treatment step consists of a subsequent decrease in temperature and increase in time. The results from the model indicate a progressive increase in heating time in the middle of the plate in each subsequent heat treatment step i.e. as the heat treatment temperature decreases, the heating time in the middle of the plate increases.

It must be noted that the numerical model used is only an approximation. The actual times will differ in practice due to factors not accounted for in the model. However, the level of accuracy of the model is sufficient to give a reasonable indication of what is happening to the turbine blade during heat treatment. The results show that all three heat treatment steps will result in homogenous heating in the entire blade.

4.2 Mechanical Testing

Variation in heat treatment parameters will result in changes in the material microstructure. Mechanical testing was therefore performed to quantify this change in terms of mechanical properties. Hardness and tensile testing was completed on heat treated specimens to show the change in material hardness and strength as a result of varying precipitation hardening temperature.

4.2.1 Hardness Testing

Vickers hardness (HV) testing was performed on heat treated specimens as outlined in section 3.3.1. The average and standard deviation of ten hardness measurements per specimen are presented in Table 6.

Heat treatment condition	Average Vickers hardness $HV_{(30kgf)}$	Std. Deviation (σ)
As Received	351	2.2
S400	392	1.5
S430	415	4.4
S450	414	3.2
S470	397	2.8
S500	379	2.7
S545	350	1.3
S600	312	2.0

Table 6: Vickers hardness measurements for FV520B in various heat treatment conditions.

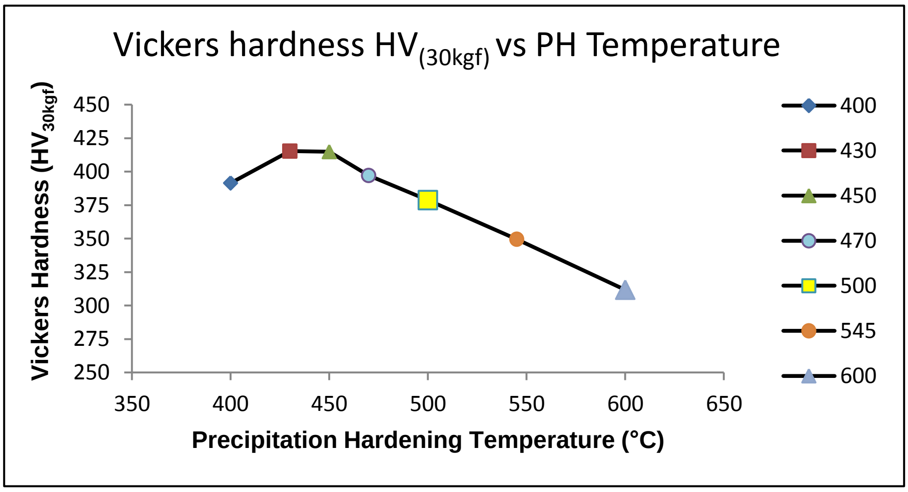

Figure 4-4: Vickers hardness as a function of precipitation hardening (PH) temperature.

It can be seen from the results presented in Table 6 and Figure 4-4 that there is a strong relationship between hardness and precipitation hardening (PH) temperature for FV520B. The appearance of a defined peak in Figure 4-4 indicates that secondary hardening has taken place at a PH temperature in the range 430-450°C. At PH temperatures higher than 450°C, hardness decreases linearly with increasing PH temperature.

A maximum hardness of 415 HV was achieved in the S430 heat treatment condition. This was closely followed by a hardness of 414 HV in the S450 heat treatment condition. These values compared well with hardness results obtained by Clark (5) for FV520B heat treated to the three standard conditions listed in Table 2. In the Peak Hardened condition, corresponding to a PH temperature of 450°C, the measured hardness was 420 $HV_{(30kgf)}$.

The hardness achieved in the As Received specimen was 351 HV. Comparing this to the hardness of 350 HV for the S545 specimen confirmed that the turbine blade was correctly heat treated to a PH temperature of 545°C. This also compares well with the hardness measured by Clark (5) for the Standard Overaged heat treatment condition of 340 $HV_{(30kgf)}$ for which the PH temperature was 550°C.

4.2.2 Tensile Testing

Tensile testing was performed on heat treated specimens as explained in section 3.3.2. The results of the tensile testing can be seen in Table 7 which shows the average values of the two tests for each heat treatment condition:

Heat treatment condition	Young's Modulus (GPa)	0.2% Proof Stress (MPa)	UTS (MPa)	0.2% PS to UTS ratio	Total elongation at fracture (%)	Reduction in Area (%)
S430	205.84	1144.31	1275.41	0.9	11.72	62.53
S450	208.25	1135.38	1258.36	0.9	14.86	64.76
S470	200	1128.92	1218.33	0.93	13.39	64.44
S500	210.82	1080.33	1129.91	0.96	12.91	69.38
S545	194.75	1026.54	1064.33	0.96	14.8	69.02
S600	203.66	851.06	964.14	0.88	16.6	71.13

Table 7: Tensile test results for FV520B in all test heat treatment conditions.

The tensile test results followed the trend of decreasing strength with increasing PH temperature. Both 0.2% proof stress and ultimate tensile stress (UTS) decreased as the PH temperature increased as seen in Figure 4-6. The specimen with the highest strength was the S430 specimen with a UTS of 1275.41 MPa and a yield stress of 1144.31 MPa. The S600 specimen possessed the lowest strength with a UTS of 964.14 MPa and a yield stress of 851.06 MPa respectively. The low strength of the S600 specimen enabled a greater elongation at fracture and reduction in area resulting in higher ductility. The yield-to-tensile strength ratio was calculated for all heat treatment conditions and ranged from 0.88 to 0.96. There was a strong linear correlation between hardness and strength for this material as seen in Figure 4-7 where an increase in hardness corresponded to an increase in tensile strength.

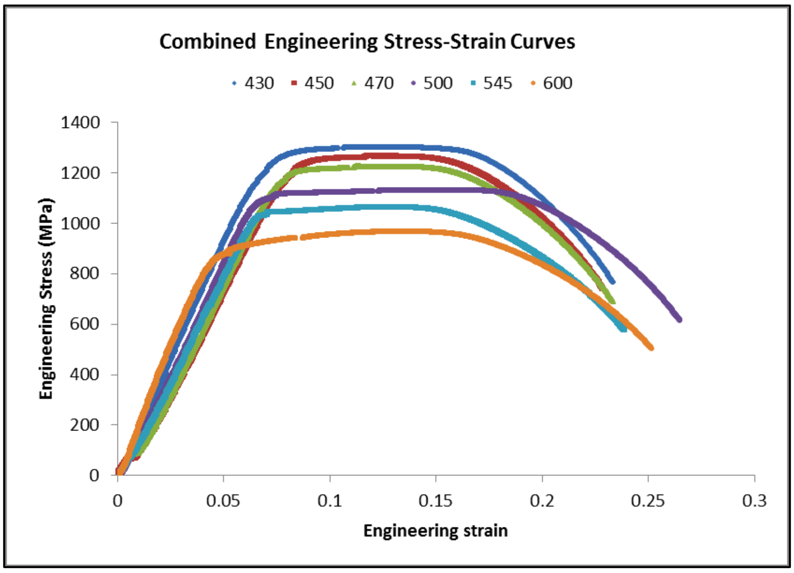

Figure 4-5: Combined engineering stress-strain curves for all heat treated specimens.

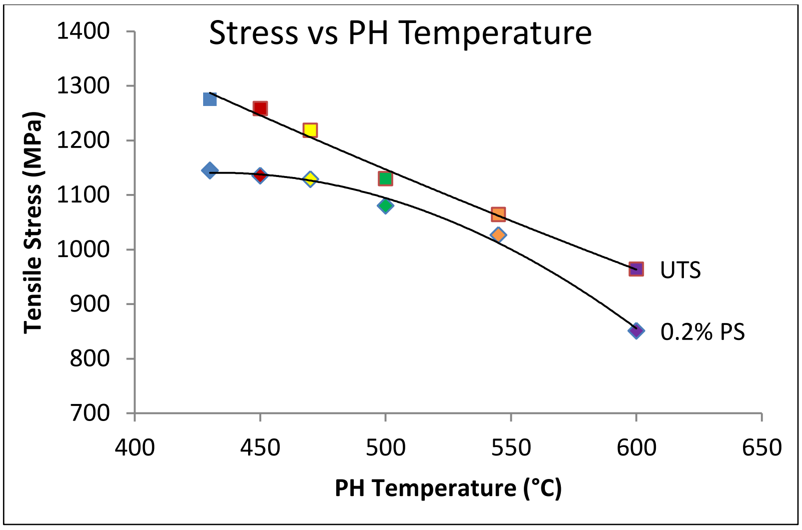

Figure 4-6: Variation in proof and tensile stress with PH temperature.

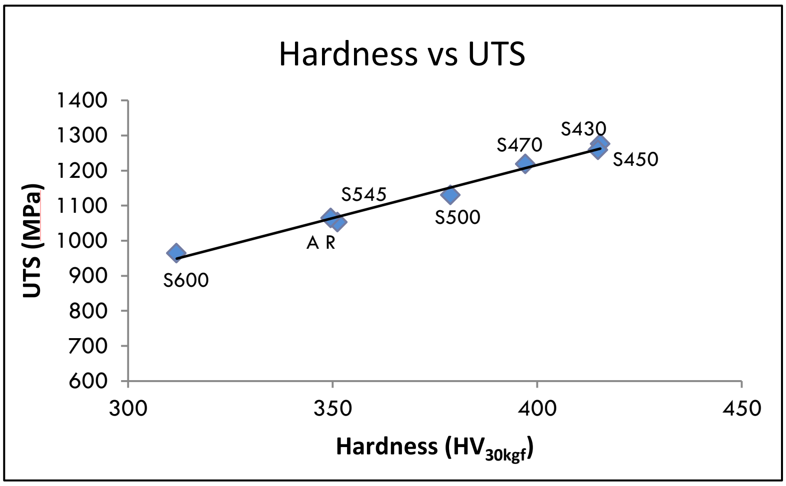

Figure 4-7: Correlation between hardness and tensile strength for FV520B.

4.3 Microstructural Characterization

4.3.1 Light Microscopy

Light microscopy was performed on polished and etched specimens to determine the general microstructural features in FV520B heat treated to different PH temperatures. Light micrographs for the different test heat treatments at 50x magnification can be seen in Figure 4-8.

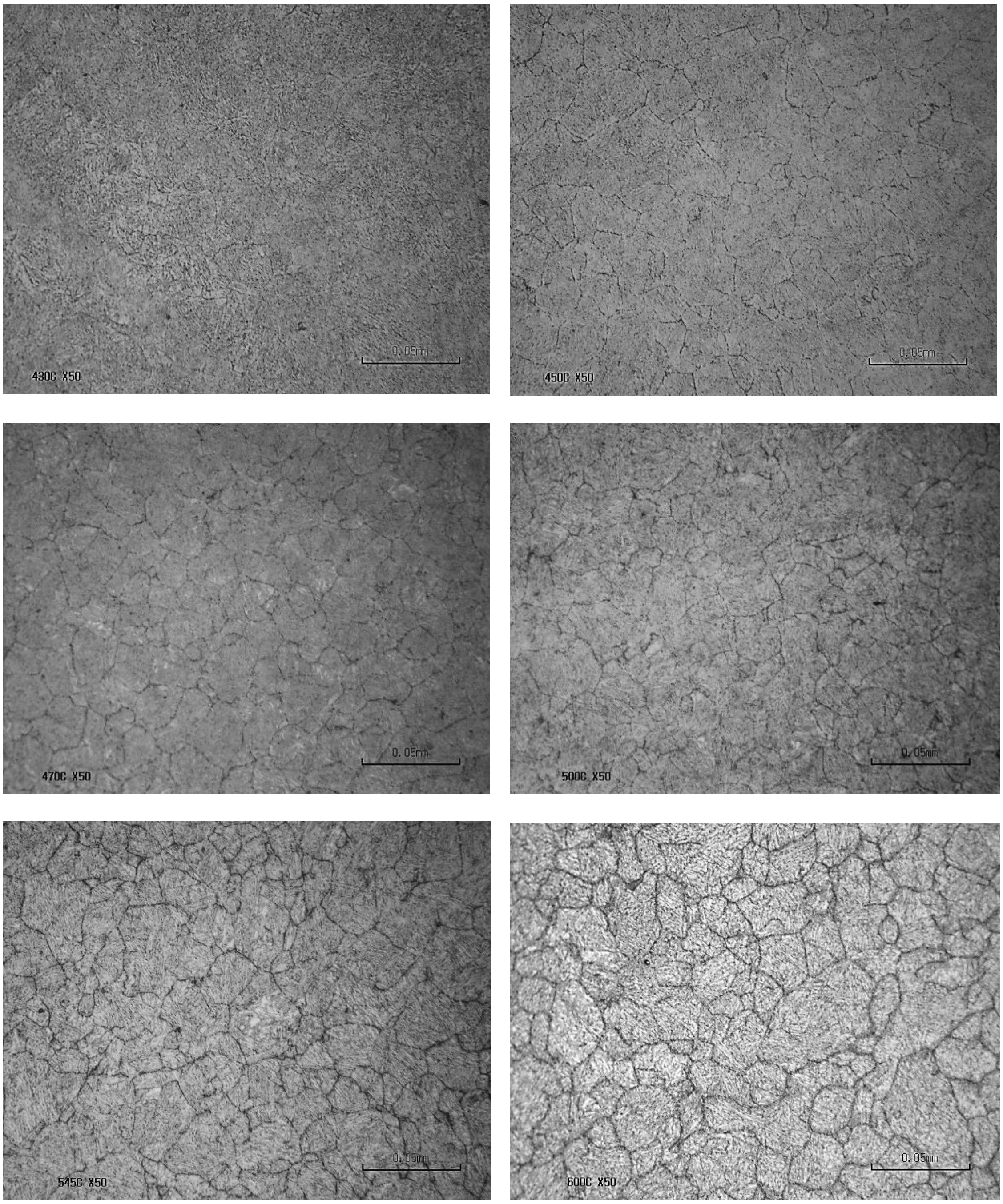

Figure 4-8: Light micrographs of heat treated specimens.

(Clockwise from top left: S430, S450, S500, S600, S545, S470)

The light micrographs in Figure 4-8 revealed martensitic microstructures containing prior austenite grain boundaries (PAGB's) and inclusions. A distinct increased visibility of PAGB's was seen as the PH temperature of the specimens increased. The S430 specimen, which was aged at the lowest PH temperature, showed very few distinguishable PAGB's. The PAGB's were more visible in the S450 specimen and continued to be more prominent in subsequent specimens. To eliminate the influence of the etching process having any effect on the visibility of the PAGB's, the specimens were grinded clean and repolished before etching again. The same pattern of PAGB visibility was seen in the repolished and re-etched specimens. This, coupled with the fact that the etching was done for shorter periods as the ageing temperature of the specimens increased, confirmed that the increased visibility of PAGB's was not due to the etching process but due to the increase in PH temperature of the specimens.

4.3.2 Scanning Electron Microscopy (SEM)

Scanning electron microscopy was conducted on etched specimens to view the microstructure under a higher magnification than was possible in the light microscope. SEM images for the S545 specimen can be seen in Figure 4-9.

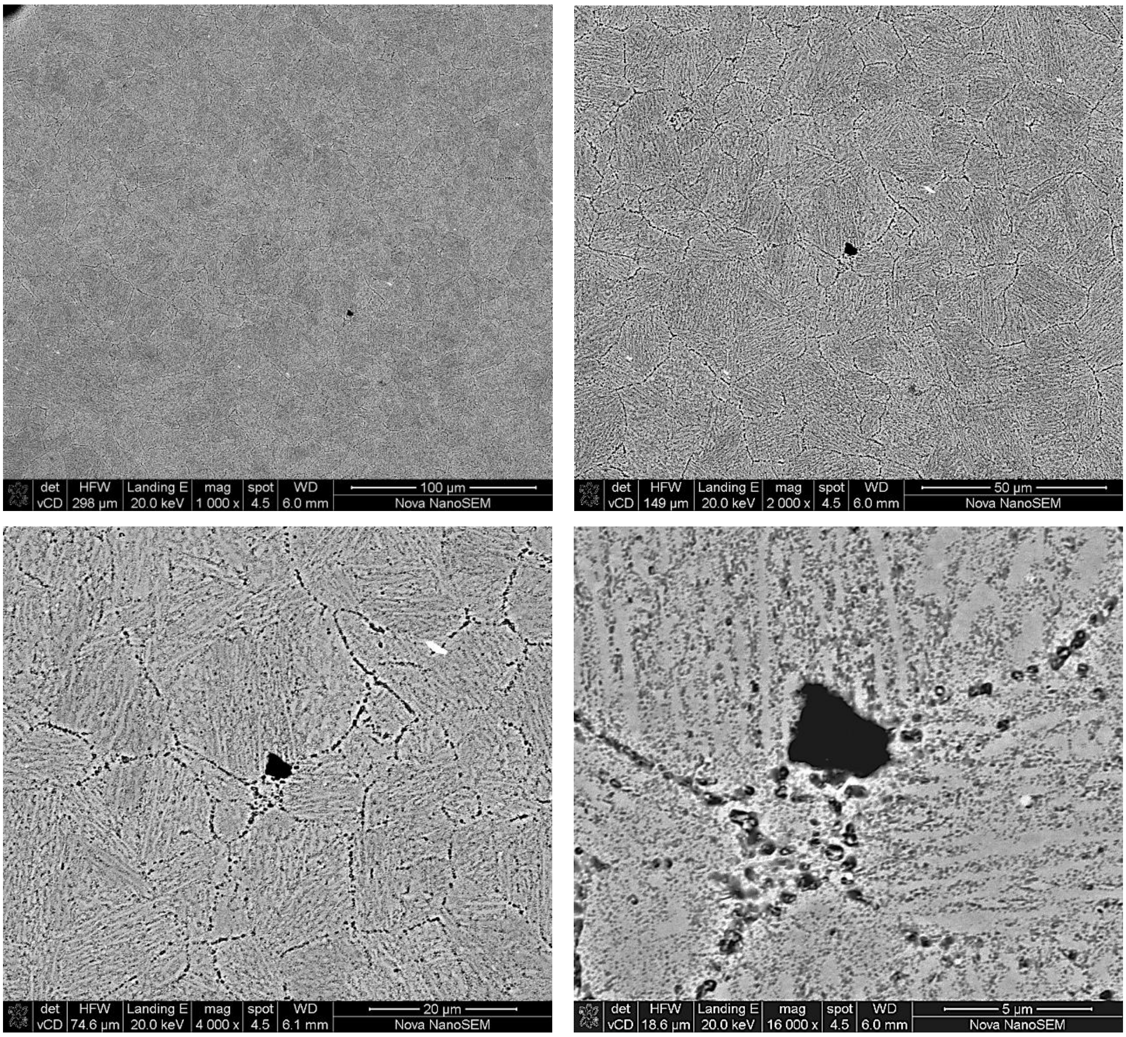

Figure 4-9: SEM images for S545 etched specimen at increasing magnification.

The etched specimens viewed in the SEM showed the same increase in PAGB visibility as was seen in the light microscope. Due to the higher magnification, it was evident that the reason for the visibility of the PABG's was the segregation of carbide precipitates to the PAGB's during heat treatment as can be seen in Figure 4-9. The segregation of carbide precipitates to the PAGB's therefore occurred more prolifically at the higher PH temperatures due to the increased diffusivity and stability of the carbides at the higher temperatures. Characterization of the precipitates segregated to the PAGB's was done using TEM and can be seen in section 4.3.6.

4.3.3 Energy Dispersive X-ray Spectroscopy (EDS) Analysis

SEM-EDS was used to perform elemental analyses on the heat treated specimens in order to identify non-metallic inclusions and other distinguishing features present in the microstructure.

4.3.3.1 Non-Metallic Inclusion Analysis

Advances in steelmaking technology have resulted in fewer foreign particles, or inclusions, in commercial steels. Their existence, however, can influence the alloys' mechanical properties such as toughness and ductility by disrupting the homogeneity of the microstructure. This necessitated their identification in FV520B. The identification of the inclusions was done purely on a qualitative basis although several different unetched specimens were analysed to provide a fairly representative sample of the material. The various types of non-metallic inclusions identified and their elemental analysis can be seen in Figures 4-10 to 4-15.

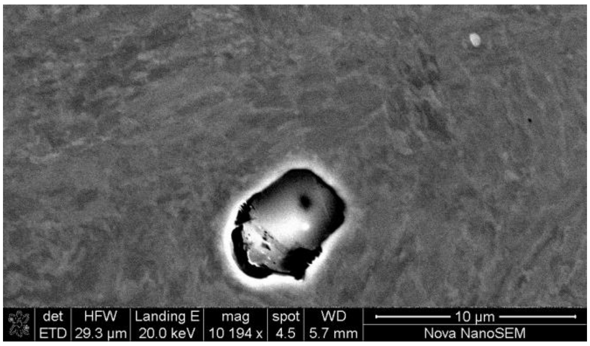

Figure 4-10: Aluminium oxide type inclusion.

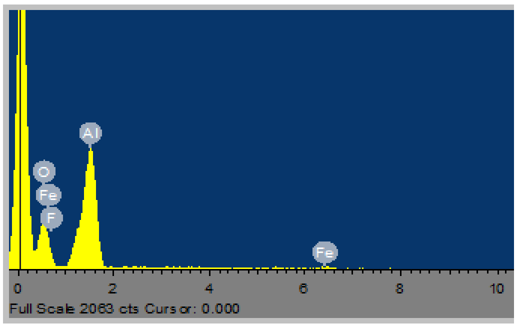

Element	Weight %	Atomic %
Al	45.72	35.77
Mg	12.66	11
O	39.84	52.56
Fe	1.78	0.67

Figure 4-11: SEM EDS spectrum analysis of aluminium oxide type inclusion (left) and elemental analysis (right).

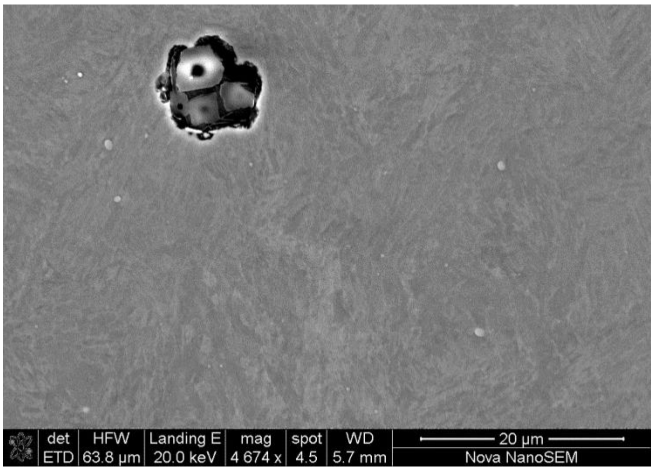

Figure 4-12: Aluminium oxide-calcium sulphide complex inclusion.

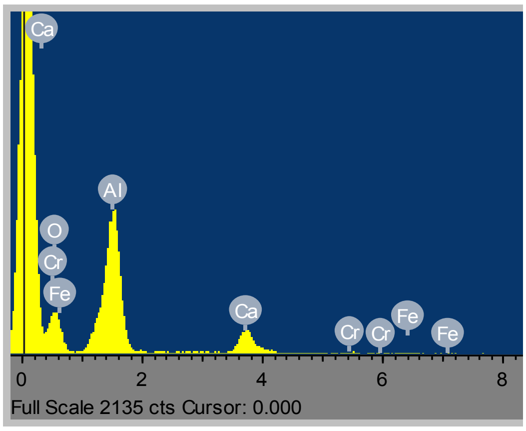

Element	Weight %	Atomic %
Al	63.43	67.75
Mg	12.44	14.75
S	4.42	3.97
Ca	16.3	11.72
Cr	1.29	0.72
Fe	2.13	1.1

Figure 4-13: SEM EDS spectrum analysis of aluminium oxide-calcium sulphide complex inclusion (left) and elemental analysis (right).

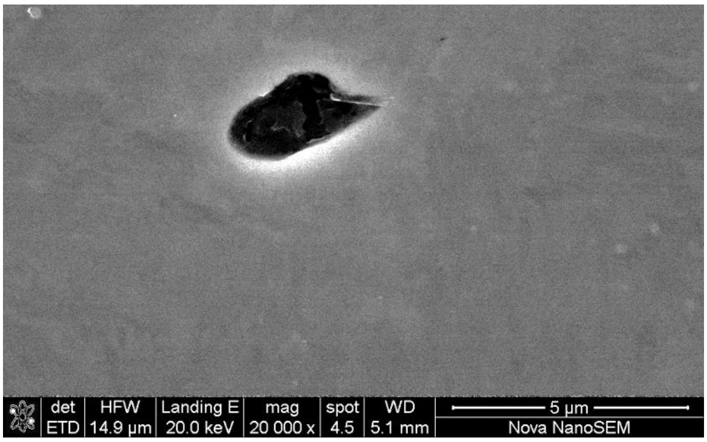

Figure 4-14: Calcium-manganese sulphide complex inclusion.

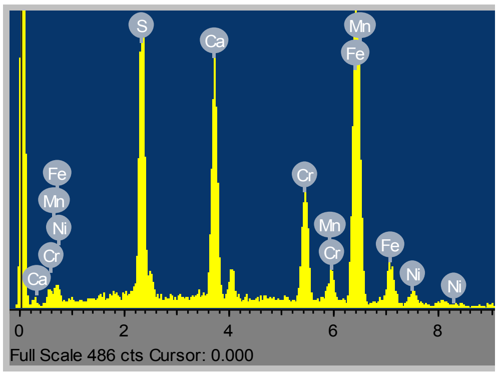

Element	Weight %	Atomic %
Ca	14.51	17.24
S	14.51	21.54
Mn	2.2	1.91
Cr	12.52	11.47
Ni	3.18	2.58
Fe	53.09	45.27

Figure 4-15: SEM EDS spectrum analysis of calcium-manganese sulphide complex inclusion (left) and elemental analysis (right).

There were predominantly three types of inclusions found most frequently: aluminium oxides, aluminium oxide-calcium sulphide complex particles and calcium-manganese sulphide complex particles. The size of the inclusions observed was typically under 10 μm in the longest dimension. The inclusion morphology varied between predominantly angular and globular particles, with few elongated stringer-type inclusions also observed. These results were consistent with inclusions found previously in FV520B (5) and FV566 (17).

4.3.3.2 Niobium carbide precipitates

During the inclusion analysis, another type of precipitate was found under high magnification in the SEM. Elemental analysis using EDS confirmed this precipitate to be niobium carbide (NbC) as seen in Figures 4-16 and 4-17.

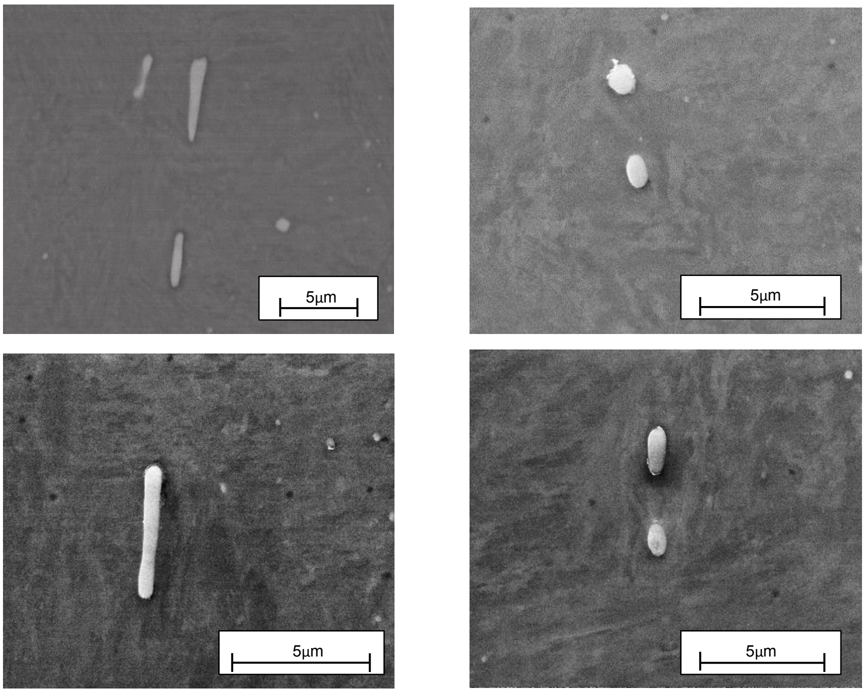

Figure 4-16: Niobium carbide precipitates-rod precipitates (left) and round precipitates (right).

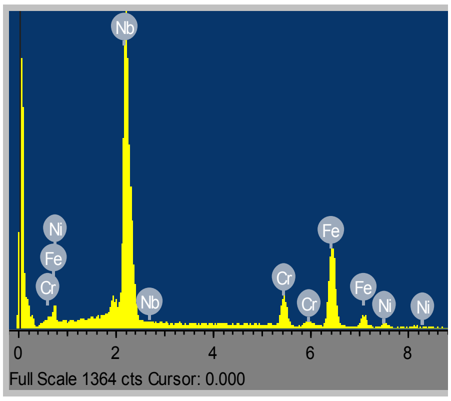

Element	Weight %	Atomic %
Nb	67.69	34.14
C	12.58	49.09
Ni	1.08	0.86
Fe	14.52	12.18
Cr	4.13	3.72

Figure 4-17: SEM EDS spectrum analysis of NbC precipitates (left) and elemental analysis (right).

The niobium carbide precipitates were easily located in the material due to their bright appearance and distinct shape. They usually appeared as a dispersion of either rod-like particles or round particles. These observations indicated that they probably precipitate as rod-like particles along preferred orientation planes in the material. Due to the specimen being a section through the material, they are sometimes seen as round particles where they are sectioned normal to their longitudinal axis. The rod-like NbC precipitates were approximately 5 µm in length and 1 µm in width. When viewed as round particles, the precipitates were approximately 1 µm in diameter.

Efforts were made to try to determine at which stage these precipitates start to form. Ma et al. (73) showed that no NbC precipitates were observed after homogenisation at 1050°C in a 13Cr supermartensitic stainless steel. A specimen subjected to homogenisation and solution treatment only (i.e. no precipitation hardening) was viewed in the SEM and NbC precipitates were seen in this specimen. It can thus be assumed that NbC precipitates start to form during solution treatment at 790°C.

The significance of the formation NbC precipitates lies in its ability to increase the strength level of the material during tempering through dispersion strengthening. Niobium is a strong carbide former whose effects on tempering are out of proportion to its concentration (20). At low concentrations (0.1% or less) and high tempering temperatures, they combine preferentially with carbon at the expense of other carbides such as $Cr_{23}C_6$ and form a fine dispersion which increases the secondary hardening effect (20). High strength levels can thus be achieved with the relatively small additions of niobium (73).

4.3.4 Dilatometry Results

Dilatometry testing was conducted to determine the phase transformation temperatures during heating and cooling cycles for FV520B. Three separate tests were conducted with each producing comparable results which can be seen in Figure 4-18.

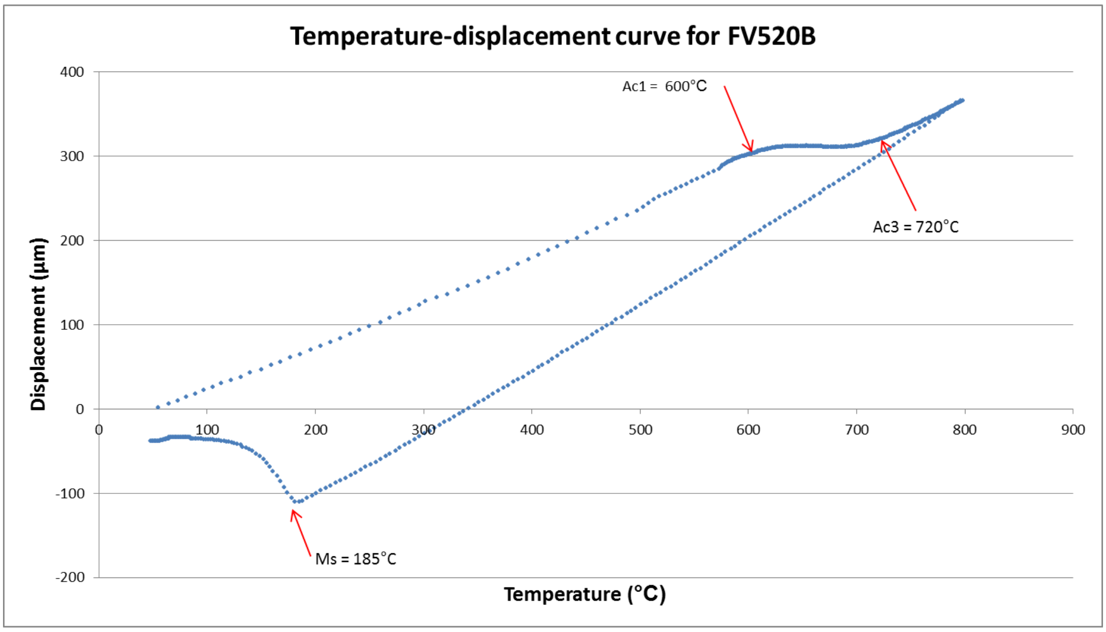

Figure 4-18: Dilatometry curve for FV520B.

The output of the dilatometry testing was a temperature-displacement curve depicting when phase transformation occurred. The transformation start temperature Ac_1 is defined as the temperature at which the linear thermal expansion first deviates from linearity (74). This is as a result of the volume contraction associated with austenite formation due to the increase in temperature. The Ac_1 temperature is determined by extrapolating the linear portion of the thermal expansion curve and locating the point of deviation. The transformation finish temperature Ac_3 is similarly determined by extrapolating the linear portion of the curve after transformation and locating the point of deviation. The Ac_1 and Ac_3 temperatures were 600°C and 720°C respectively.

Upon rapid cooling from a completely austenitic microstructure, the specimen underwent contraction with the dilatometric curve deviating from linearity due to the volume expansion associated with martensitic transformation. The M_s temperature was 185°C, representing the first deviation from linearity during cooling. The M_f temperature could not be determined due to the dilatometry software shutting down before M_f could be reached. This occurred during each test and was possibly due to a software limitation on the number of points sampled. The M_f temperature for martensitic precipitation hardening stainless steels is usually at or slightly above room temperature (75). The shape of the dilatometric curve in Figure 4-18 indicates that M_f was likely to be in the region of room temperature.

4.3.5 X-ray Diffraction Results

XRD analyses were performed on specimens heat treated to all conditions listed in Table 4. Two additional specimens were analysed, one undergoing only homogenisation at 1020°C and the other undergoing homogenisation at 1020°C followed by solution treatment at 790°C. The resulting XRD spectra can be seen in Figures 4-19 to 4-26 with each plot showing the intensity of diffracting planes as a function of the Bragg angle (2θ).

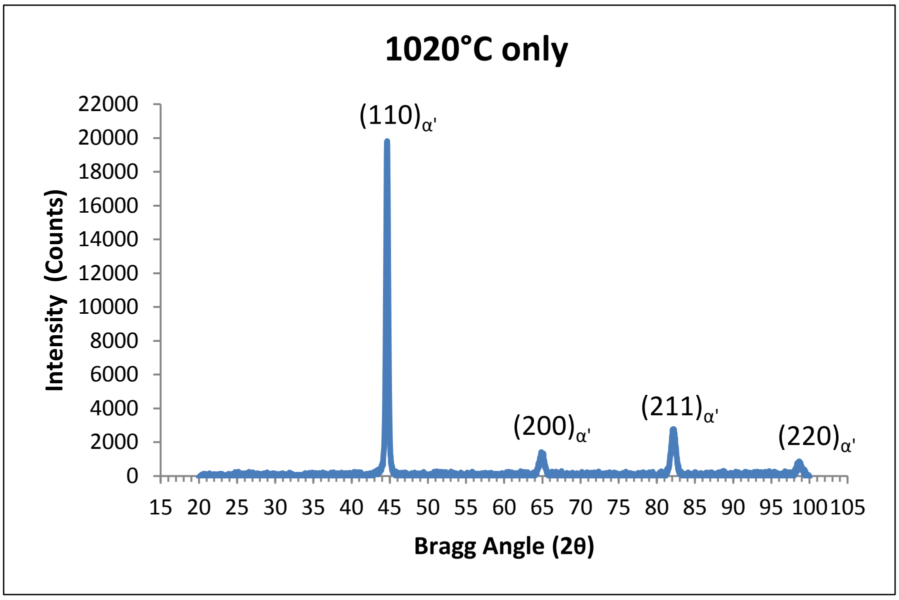

Figure 4-19: XRD spectrum for specimen undergoing homogenisation only.

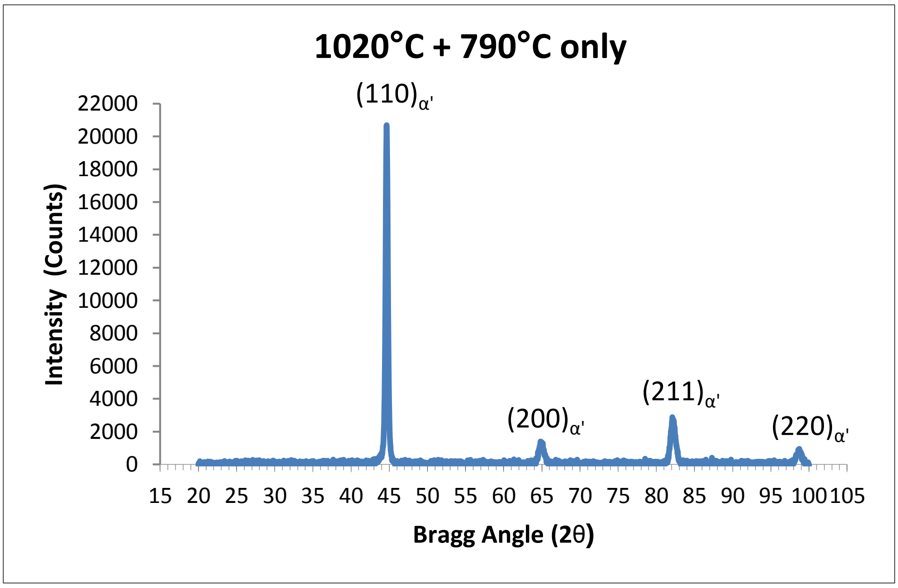

Figure 4-20: XRD spectrum for specimen undergoing homogenisation and solution treatment only.

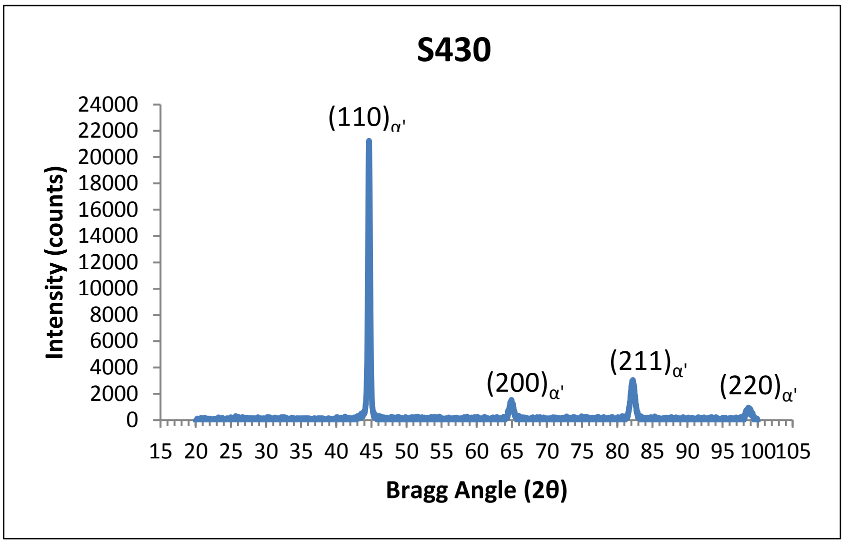

Figure 4-21: XRD spectrum for S430 specimen.

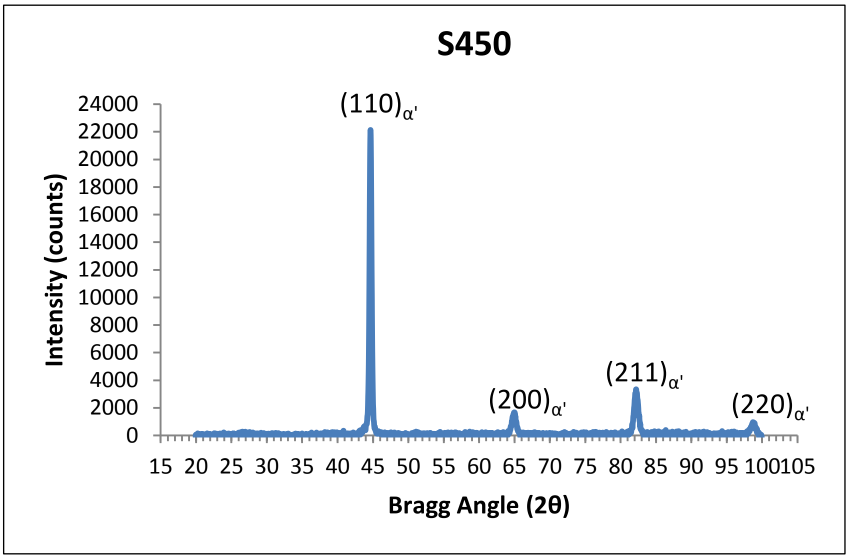

Figure 4-22: XRD spectrum for S450 specimen.

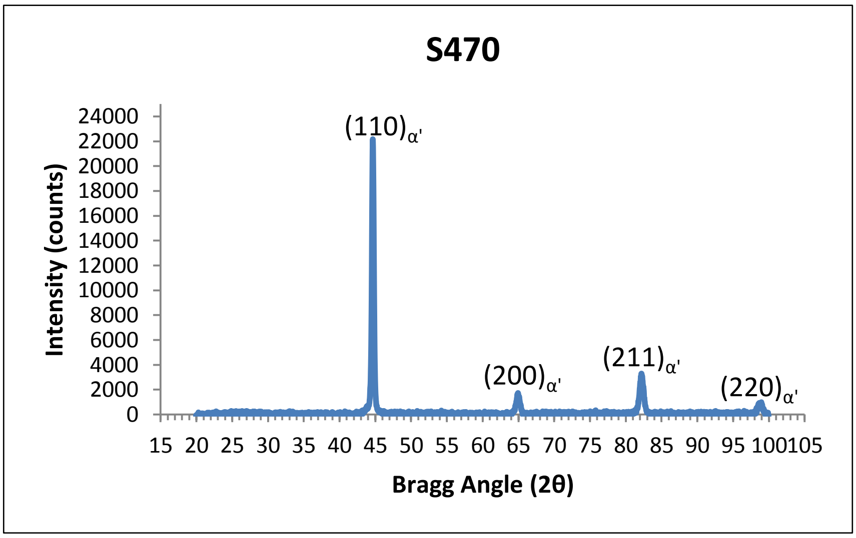

Figure 4-23: XRD spectrum for S470 specimen.

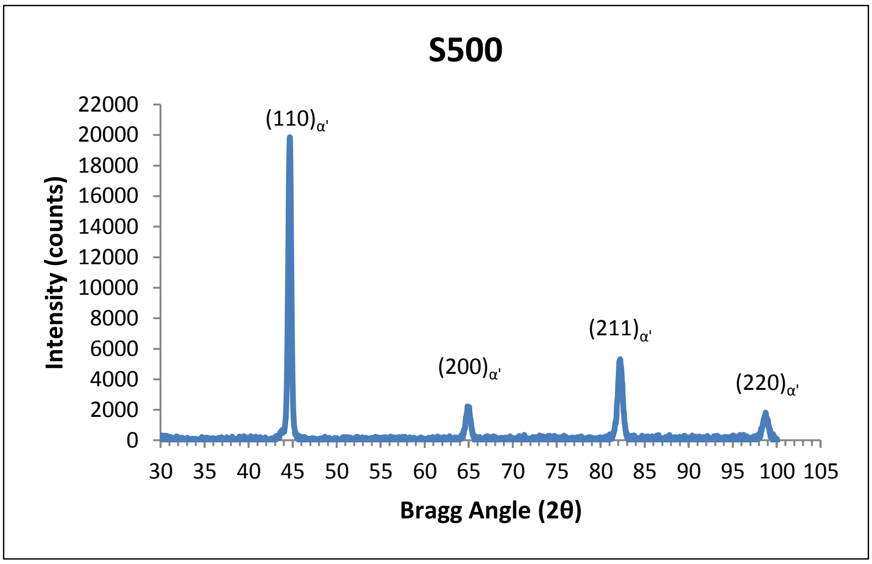

Figure 4-24: XRD spectrum for S500 specimen.

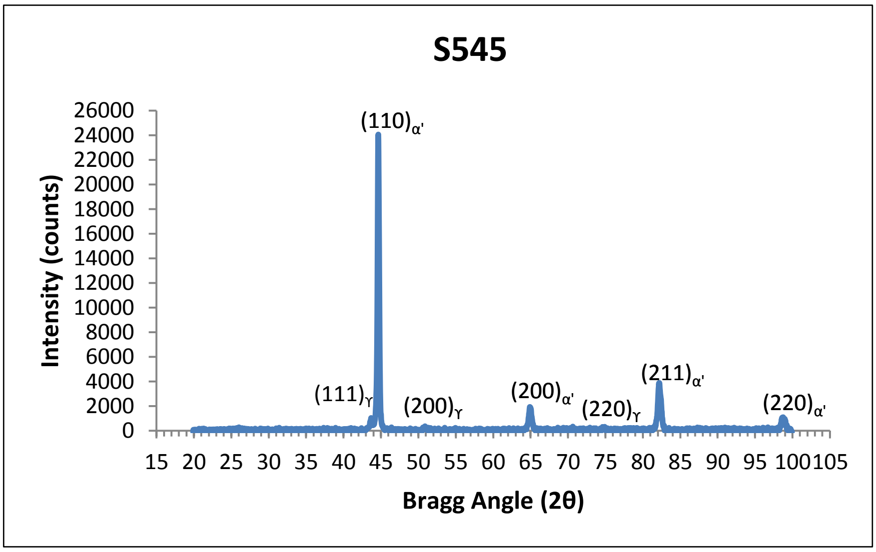

Figure 4-25: XRD spectrum for S545 specimen.

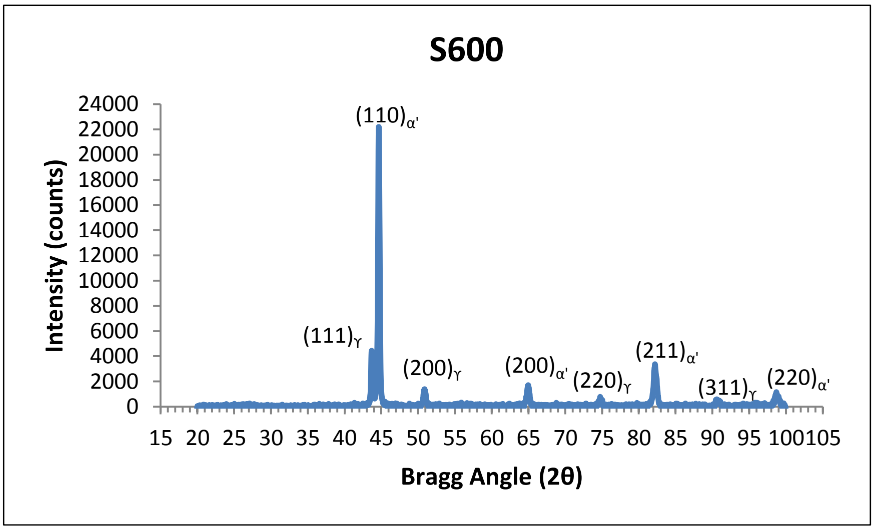

Figure 4-26: XRD spectrum for S600 specimen.

Figures 4-19 and 4-20 show that for the specimens that underwent homogenisation and homogenisation plus solution treatment only, high intensity peaks at Bragg angles of 45°, 65°, 82° and 99° indicated that diffraction occurred from the $(110)_{\alpha'}$, $(200)_{\alpha'}$, $(211)_{\alpha'}$, and $(220)_{\alpha'}$ planes. This corresponded a body-centered cubic (bcc) crystal structure which meant that the final microstructure in those specimens was martensite. Figures 4-21 to 4-24 for the S430, S450, S470 and S500 specimens revealed similar diffraction patterns indicating that those heat treatment conditions also resulted in a martensitic microstructure, although different levels of tempering would have occurred.

Figures 4-25 and 4-26 for the S545 and S600 specimens showed additional peaks at Bragg angles of 44°, 51°, and 75° indicating that diffraction occurred from the $(111)_{\gamma}$, $(200)_{\gamma}$, and $(220)_{\gamma}$ planes. The S600 specimen showed an extra peak at 91° corresponding to the $(311)_{\gamma}$ diffraction plane. These additional peaks corresponded to a face-centered cubic (fcc) crystal structure which revealed the presence of some reverted austenite in these two specimens. The intensity peaks corresponding to austenite for the S600 specimen were larger than those for the S545 specimen which indicated that there was a greater percentage of austenite in the S600 specimen.

4.3.5.1 Quantitative Analysis of XRD Results

Since the presence of reverted austenite was confirmed in the XRD analyses, this necessitated the need to quantify the amount of austenite present in the different test specimens. Quantitative analysis was performed using MAUD software in conjunction with the XRD spectra. Figure 4-27 shows the software output of the simulated and refined diffraction pattern for the S600 specimen overlayed onto the XRD spectrum. It can be seen that the XRD spectrum is simulated fairly well by the software which improved the likelihood that the resulting quantification of phases was relatively accurate. This was the case for all the specimens.

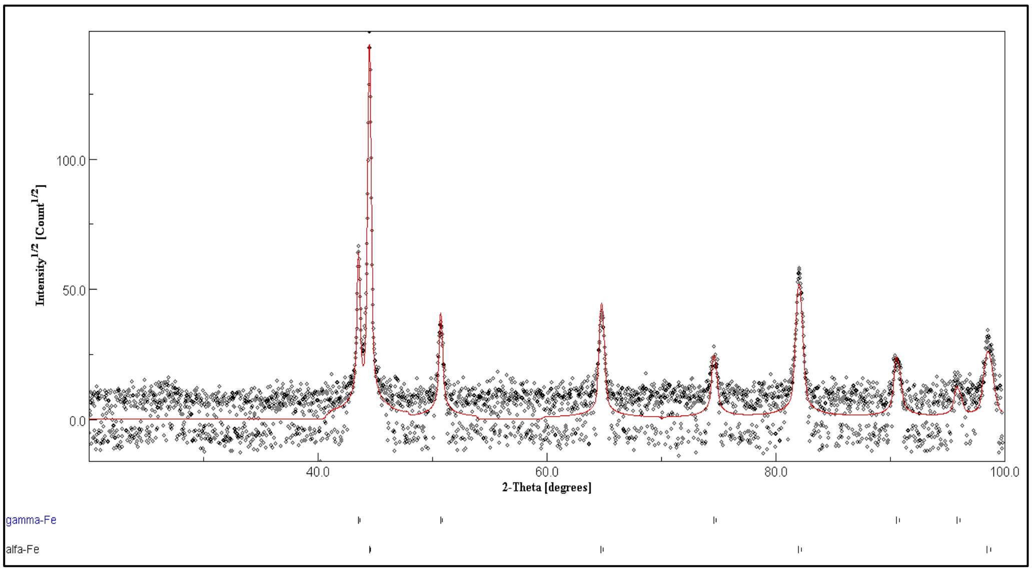

Figure 4-27: Simulated and refined diffraction pattern for the S600 specimen.

Since the two additional XRD specimens (Figures 4-19 and 4-20) showed no indications of austenite in the microstructure from the XRD spectra, it was decided not to perform quantitative analyses for them. Table 8 shows the quantitative analyses for the six specimens heat treated to the test conditions listed in Table 4.

Specimen	Phase	Volume Fraction (%)	Weight Fraction (%)
S600	Gamma-Fe (Austenite)	20.8	21.2
	Alpha-Fe (Martensite)	79.2	78.8
S545	Gamma-Fe (Austenite)	4.2	4.3
	Alpha-Fe (Martensite)	95.8	95.7
S500	Gamma-Fe (Austenite)	1.4	1.5
	Alpha-Fe (Martensite)	98.6	98.5
S470	Gamma-Fe (Austenite)	1.3	1.3
	Alpha-Fe (Martensite)	98.7	98.7
S450	Gamma-Fe (Austenite)	1.4	1.4
	Alpha-Fe (Martensite)	98.6	98.6
S430	Gamma-Fe (Austenite)	0.2	0.2
	Alpha-Fe (Martensite)	99.8	99.8

Table 8: Results of quantitative XRD analysis.

The results of the quantitative XRD analysis showed that significant amounts of austenite were found in the S545 and S600 specimens. The other specimens contained very little austenite, the amounts being within the margin of error for the analysis. The S600 specimen contained the most austenite with 20.8% while the S545 specimen contained 4.2%, both by volume fraction. The presence of austenite in the microstructure of the higher tempered specimens can be explained using the dilatometry results in section 4.3.4. It was found through dilatometry that the Ac_1 temperature was 600°C. Therefore, tempering at temperatures close to the Ac_1 temperature would result in a reversion to austenite from the martensitic structure obtained after solution treatment. The precipitation hardening (PH) treatment duration of 6 hours would also have aided the reversion to austenite. It can thus be concluded that above approximately 500°C, the amount of reverted austenite present in the microstructure upon cooling increases with PH temperature.

4.3.6 Transmission Electron Microscopy Results

Transmission electron microscopy was performed on heat treated specimens to determine how the formation and location of precipitates was affected by PH temperature. Focused ion beam (FIB) specimens taken across prior austenite grain boundaries were analysed for the S430, S500 and S600 conditions as well as the As Received condition. Carbon Extraction Replicas (CER) were taken for the S430 and S600 specimens.

4.3.6.1 Focused Ion Beam TEM Results

FIB specimens were selected to span across a prior austenite grain boundary and energy filtered TEM (EFTEM) elemental maps were generated. Chromium-rich precipitates were found in the S430, S500, S600 and As Received specimens analysed. The location of these precipitates appears to be along the sub-grain and prior-austenite grain boundaries.

The size of the Cr-rich precipitates varied within each of the specimens analysed. The S600 specimen did show a greater number of large precipitates compared with the other specimens analysed. The S600 specimen also showed the clear presence of Nb-rich precipitates which were readily distinguishable due to their circular shape as compared to the Cr-rich precipitates which were more angular in shape. The EFTEM elemental maps can be seen in Figures 4-28 and 4-29.

High angle annular dark field (HAADF) images were also analysed using EDS to determine if there was any chromium depletion adjacent to prior austenite grain boundaries where Cr-rich precipitates were present. Chromium depletion would be as a result of sensitization which could aid in explicating the stress corrosion behaviour of the material in the different heat treated conditions. The EDS results for the S430 and S600 specimens can be seen in Figures 4-30 to 4-32.

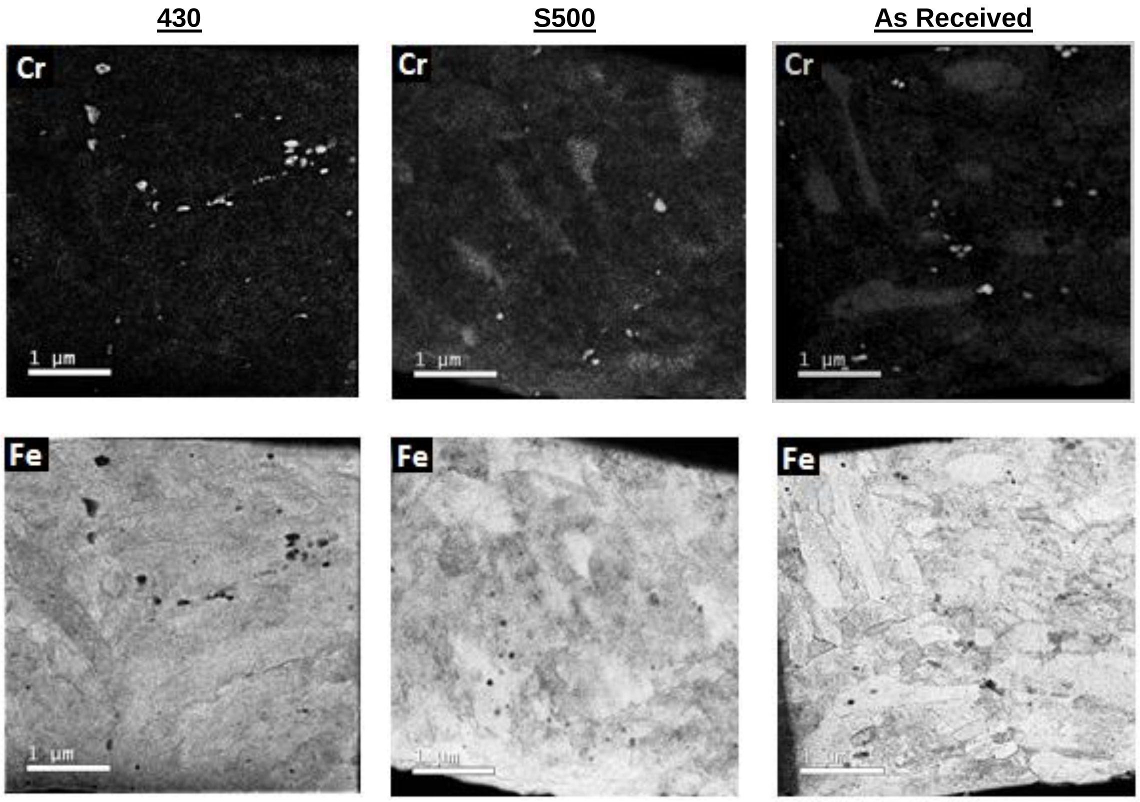

430 **S500** **As Received**

Figure 4-28: EFTEM elemental maps showing location of Cr-rich precipitates for S430, S500 and As Received specimens.

S600

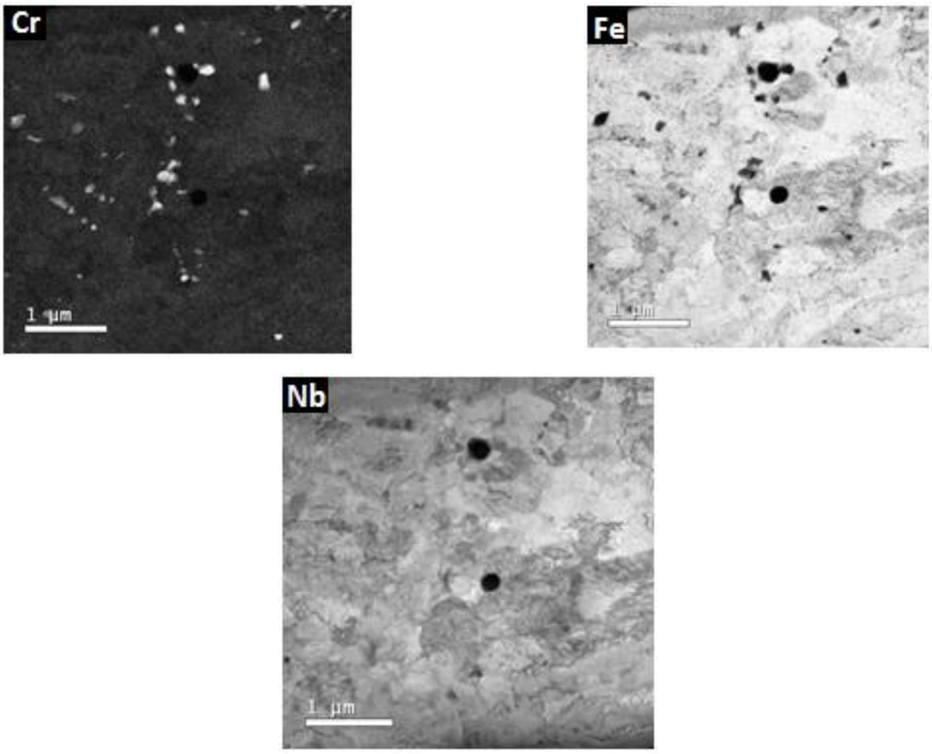

Figure 4-29: EFTEM elemental maps showing location of Cr- and Nb-rich precipitates for S600 specimen.

S430 specimen

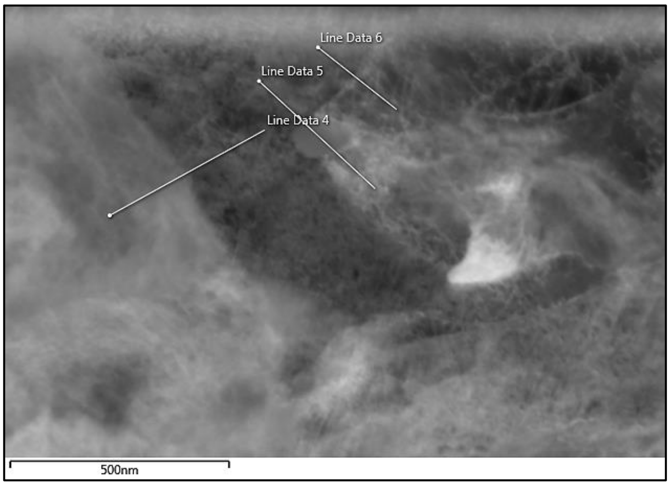

	Line Data 4	Line Data 5	Line Data 6
Cr	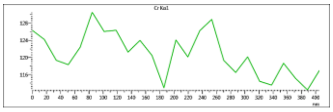	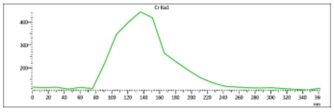	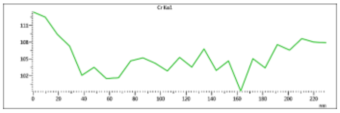
Fe	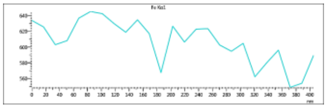	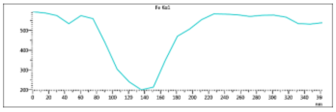	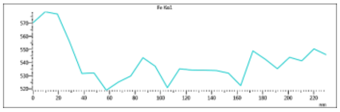
Ni	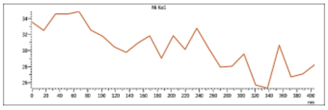	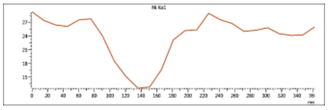	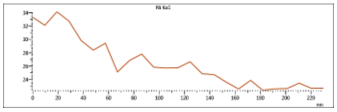

Figure 4-30: HAADF-STEM image and EDS results for S430 specimen.

Figure 4-30 shows the results of three line scans taken across prior austenite grain boundaries for the S430 specimen. Line data 4 shows a drop in Cr-content in approximately the region of the prior austenite grain boundary as seen in the HAADF image. However, the Cr-content continued decreasing further along the line, away from the grain boundary. The sharp increase in the Cr-content seen in Line Data 5 indicates the presence of a Cr-precipitate. The Cr-content, however, does not decrease below the normalised level in the regions adjacent to the grain boundary as would be seen if Cr-depletion had occurred. Line Data 6 shows no appreciable change in Cr-content in the region of the prior austenite grain boundary.

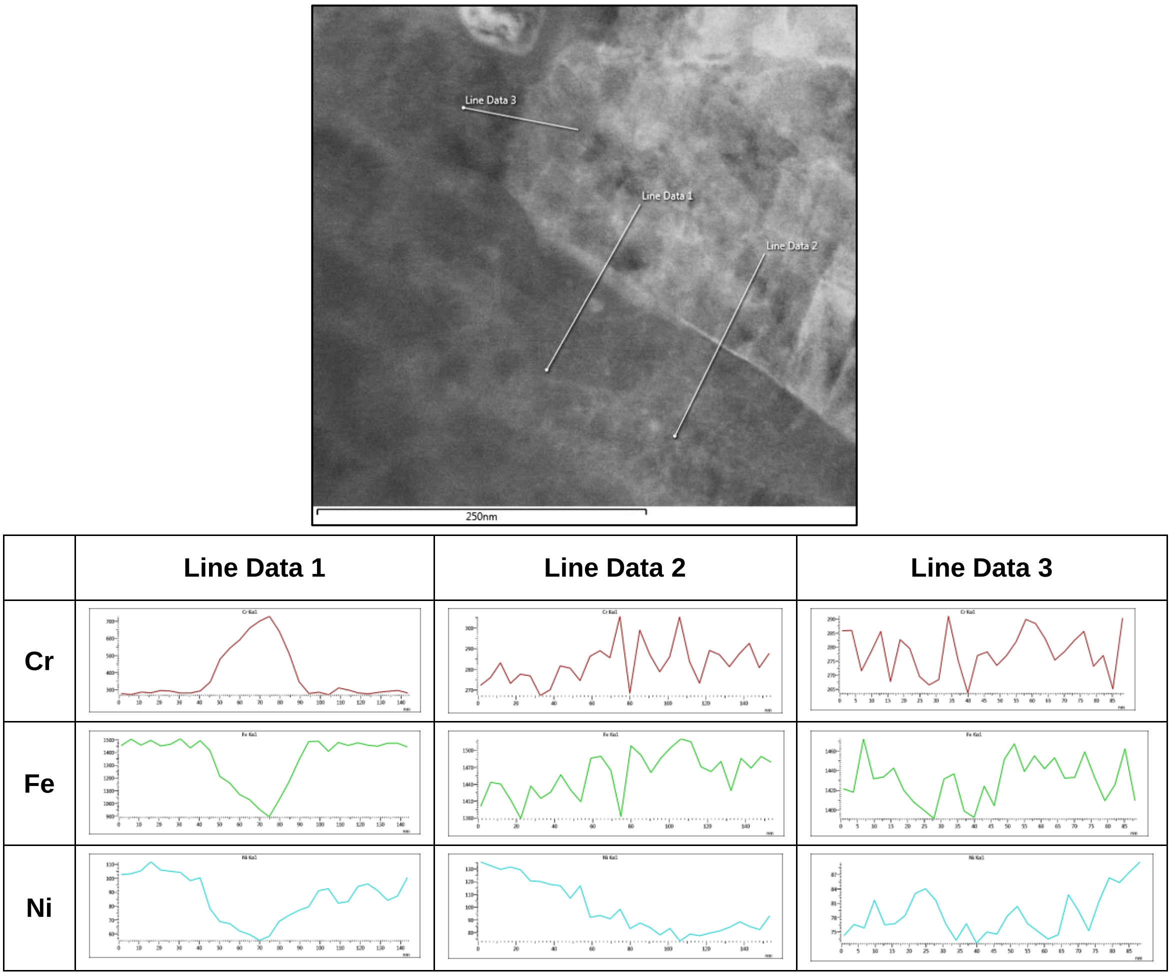

Figure 4-31: HAADF-STEM image and EDS results for S430 specimen using Atomic Resloution Microscope.

The width of the Cr-depletion zone in the region of the prior austenite grain boundary is approximately 25 nm in austenitic stainless steels like 316L (76). This Cr-depletion zone would be much narrower (in the region of 10 to 15 nm) for martensitic stainless steels due to their lower Cr content compared to austenitic stainless steels (77). It was therefore decided to analyse a smaller area around the prior austenite grain boundary using the JEOL Double Cs-corrected Atomic Resolution Microscope (ARM) 200F to improve the resolution. These results can be seen in Figure 4-31. Line Data 1 shows an increase in Cr-content in the region of the grain boundary most probably due to the presence of a Cr-rich precipitate. There was, however, no decrease in Cr-content below the nominal level in the areas adjacent to the grain boundary to indicate Cr-depletion. The results for Line Data 2 and Line Data 3 showed no definitive trend in the Cr-content.

S600 specimen

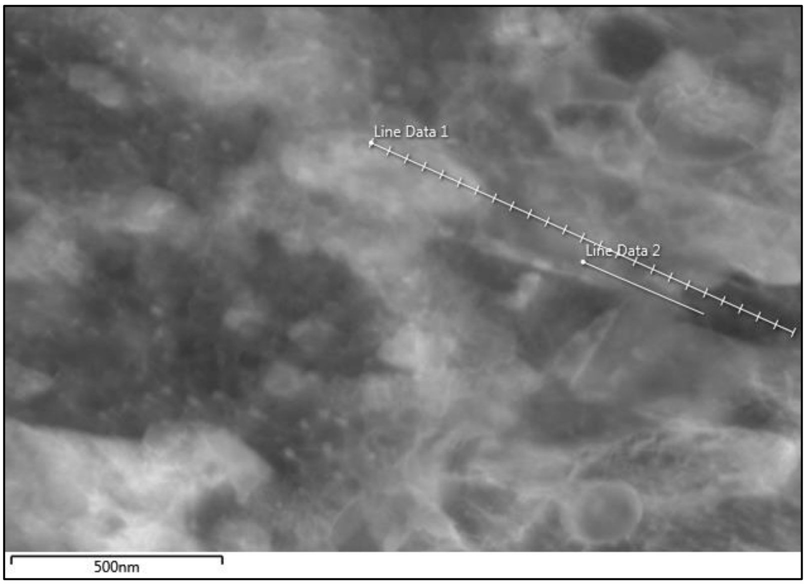

	Line Data 1	Line Data 2
Cr	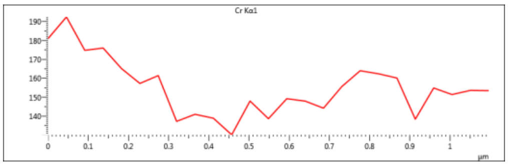	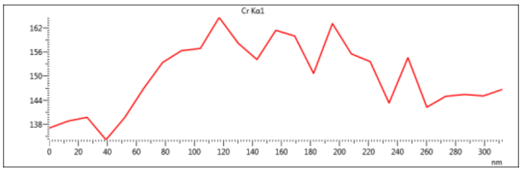
Fe	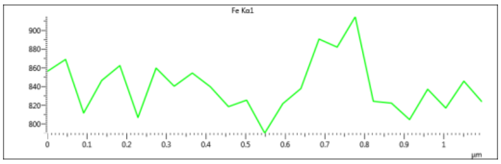	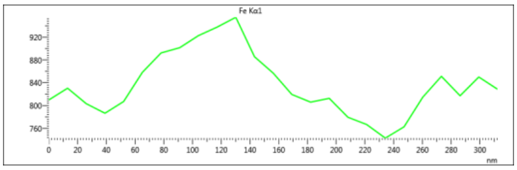
Ni	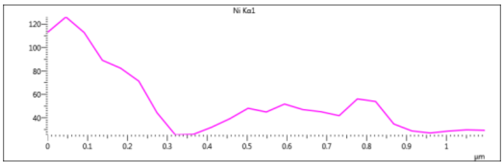	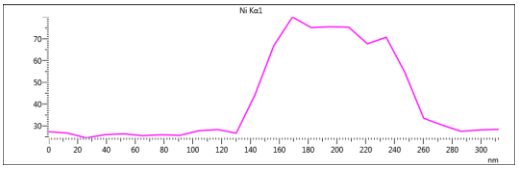

Figure 4-32: HAADF-STEM image and EDS results for S600 specimen.

Figure 4-32 shows the results for the S600 specimen. Line Data 1 shows a slight decrease in the Cr-level while Line Data 2 shows an increase in Cr-content. These results are indicative of the fact that the S600 specimen contained more Cr-rich precipitates along the prior austenite grain boundaries than the other specimens. This agglomeration of precipitates along the grain boundaries meant that a line scan would invariably pass through many Cr-rich precipitates leading to fluctuations in the Cr-content as seen above.

4.3.6.2 Carbon Extraction Replication TEM Results

Carbon extraction replication specimens were prepared from etched specimens in the S430 and S600 conditions and analysed in the TEM. The HAADF images clearly showed the accumulation of precipitates along the grain boundaries. EDS was conducted to determine the composition of the precipitates. Chromium-rich and niobium-rich precipitates were found in both specimens. The niobium precipitates were prominent due to their circular shape. The size of the precipitates varied within each of the specimens analysed. The S600 specimen showed a greater number of precipitates compared with the S430 specimen. The HAADF images and EDS spectra for the S430 and S600 specimens can be seen in Figures 4-33 and 4-34.

S430 specimen

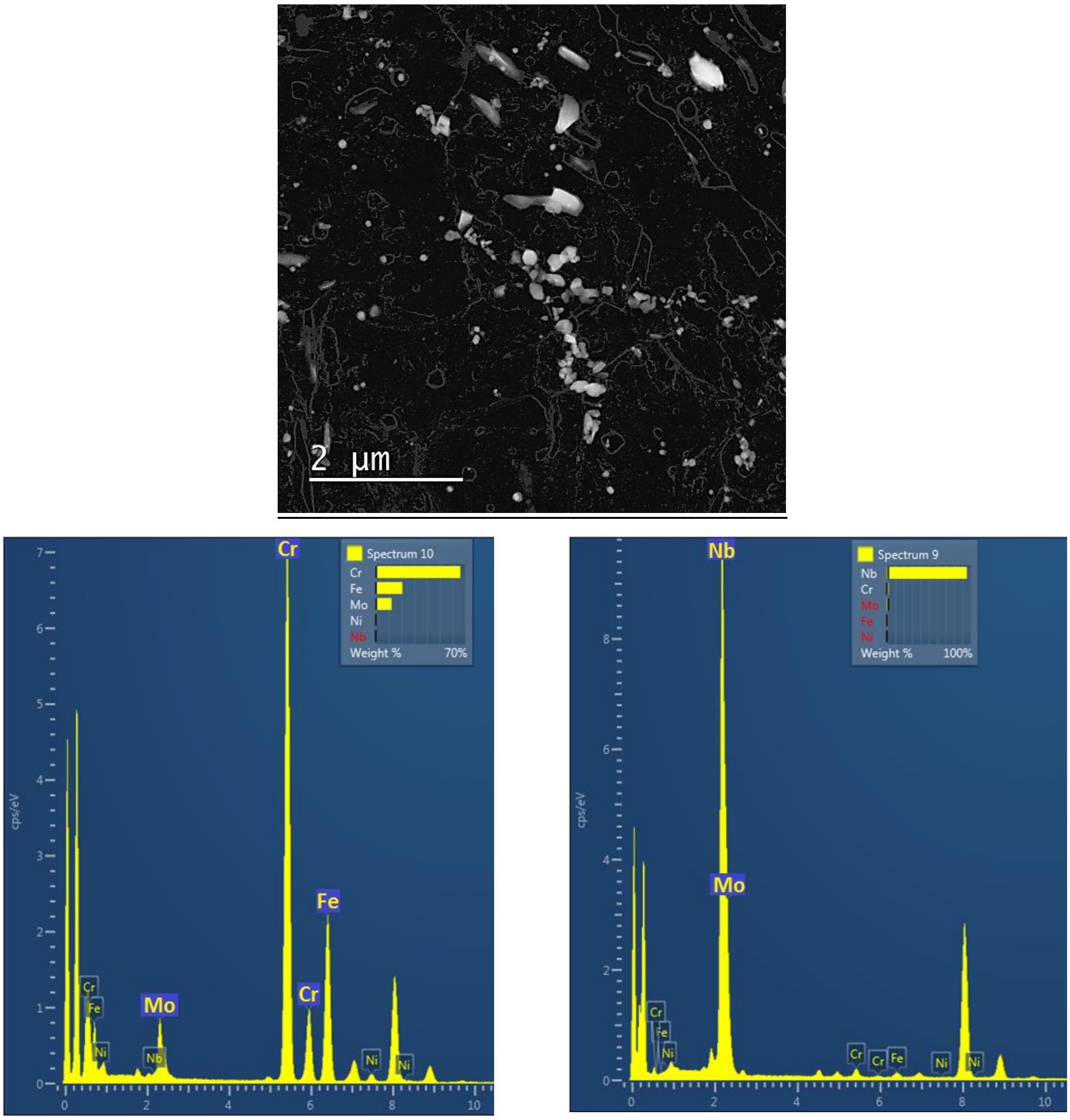

Figure 4-33: HAADF-STEM image showing precipitates and EDS spectra for S430 specimen.

S600 specimen

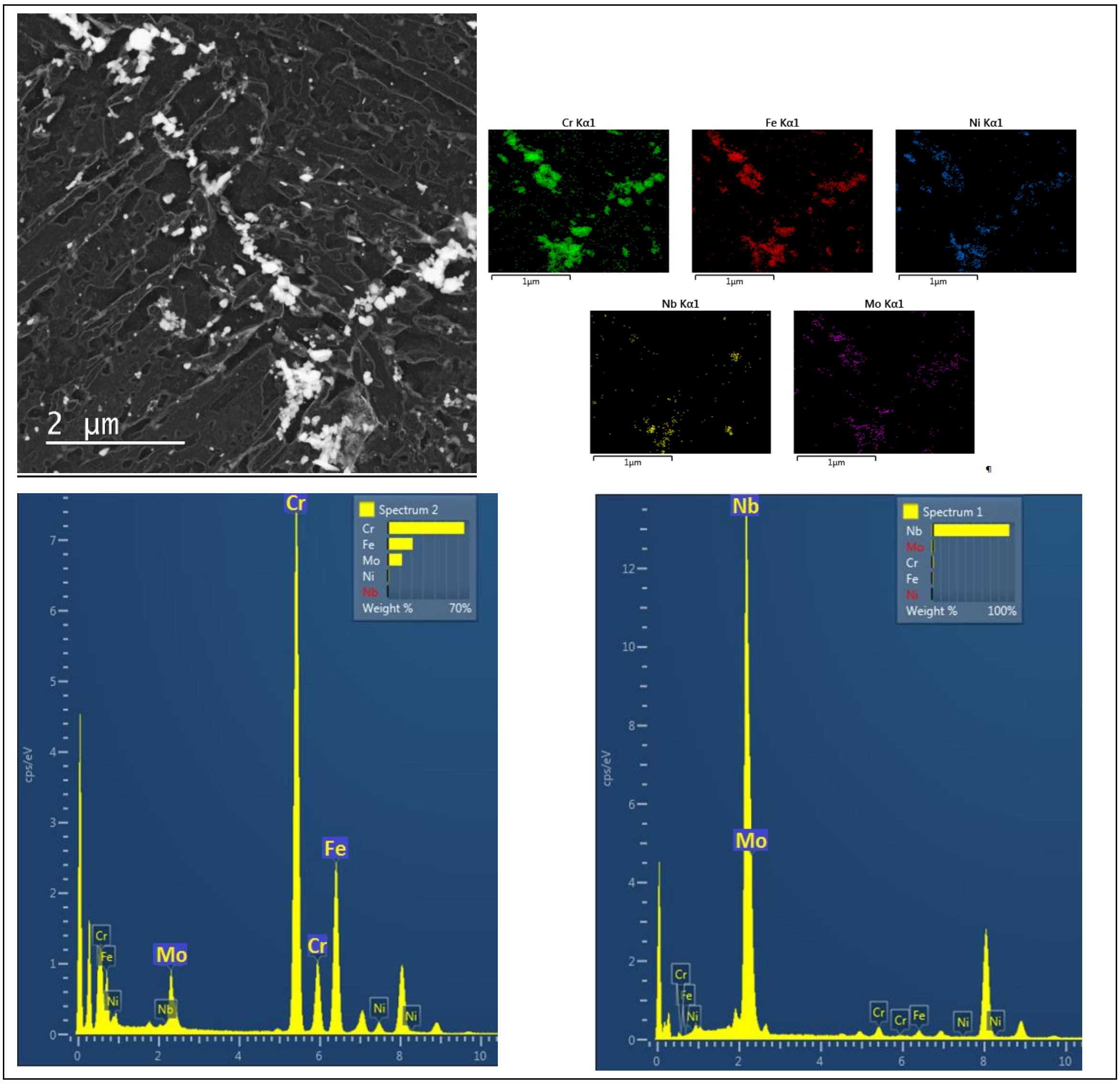

Figure 4-34: HAADF-STEM image showing precipitates and EDS spectra for S600 specimen.

4.4 Stress Corrosion Testing Results

4.4.1 SCC Susceptibility Test Results

U-bend specimens were immersed in a 3.5% sodium chloride test solution heated at 90°C. Specimens were divided into batches of six specimens each, one specimen per heat treatment condition listed in Table 4, in each batch.

4.4.1.1 Batch 1 U-bend Failures

Batch 1 was tested and monitored for indications of first crack initiation which constituted failure in accordance with ASTM G30. The time to failure results for Batch 1 can be seen in Table 9. The S430 specimen was the first to crack with crack initiation after 64 hours. This was followed by the S450 which cracked after 99 hours. The rest of the specimens cracked at staggered intervals with the crack initiation time increasing according to the specimen temper condition. As the specimen precipitation hardening temperature increased, the specimen took longer to crack.

Although the specimens produced cracks during testing, the location of the cracks was unexpected. All the specimens in Batch 1 produced cracks in the leg of the U-bend specimen at the bolt hole as seen in Figure 4-28. This was in contradiction to the anticipated crack initiation location, which was the outer surface of the curved U-bend geometry, where the tensile stress in the specimen was thought to be the maximum. The specimens were kept in the test solution until the cracks propagated completely from the bolt hole to the outer edge of the specimen to enable analysis of the fracture surface.

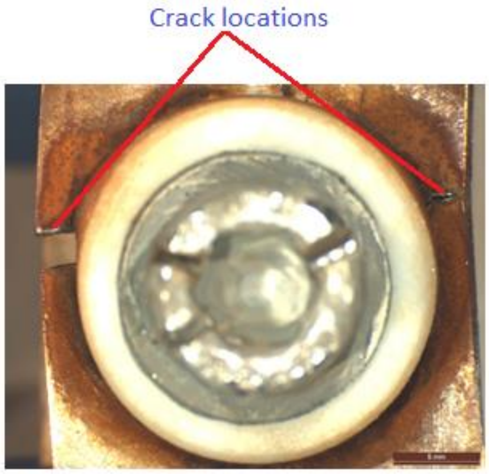

Figure 4-35: S470 U-bend specimen showing location of cracks at the bolt hole.

An investigation was conducted into why the specimens were cracking at the bolt holes and not on the curved U-bend surface as expected. Once the specimens were removed from the test environment, they were disassembled. Upon disassembly, the PTFE insulators proved difficult to remove due to an extremely tight fit in the bolt holes. While the clearance between the insulators and the bolt holes during assembly was not loose, it also wasn't tight enough to prevent their removal. This lead to the conclusion that the PTFE insulators underwent some expansion while in the hot test solution to cause them to be fastened tight inside the bolt holes of the specimen. This was thought to have created a stress concentration around the bolt hole high enough to cause cracks to initiate there instead of on the curved U-bend surface.

Cracking of the specimens at the bolt holes broke the specimen into two pieces, one large piece and one small piece consisting of part of the bolt hole and the area just below the hole. The small size of this piece enabled it to be mounted in resin, polished and viewed under the optical microscope. Under the optical microscope, fine cracks around the bolt hole could be seen. Some specimens also showed multiple deep pits in the area around the bolt hole. This was thought to be caused by the insulator-specimen interface which produced the optimal conditions for crevice corrosion to take place. These pits could then become ideal crack initiation points from which stress corrosion cracks could develop. Images of the U-bend specimens from Batch 1 can be seen in section 4.4.1.5.

4.4.1.2 Batch 2 U-bend failures

Since the specimens in Batch 1 did not crack as expected, it was decided to implement some changes to get the specimens in Batch 2 to behave as required. Two changes were made to the Batch 2 specimens. Firstly, the clearance between the PTFE insulator and the specimen was increased to create a loose fit. This would reduce the stress concentration around the bolt hole. Secondly, the insulator-specimen interface was coated with a thin layer of vinyl coating to prevent crevice corrosion around the bolt hole and consequently preventing pitting.

Batch 2 specimens were tested and monitored for crack initiation. The specimens followed a similar trend to Batch 1 in terms of times to failure and the order in which the specimens cracked, with the failure time increasing with temper temperature of the specimen. The time to failure results for Batch 2 can be seen in Table 9. The times to failure for Batch 2 were generally higher than Batch 1 except for the S500 specimen which cracked earlier than the corresponding specimen in Batch 1. The major difference was that no cracking was found in the S600 specimen in Batch 2 after more than 5000 hours in the test environment.

Although changes were made to the Batch 2 specimens before testing, cracking occurred in a similar manner to Batch 1. Cracks initiated and propagated around the bolt hole in some specimens while others showed crack initiation just above the bolt hole. This proved perplexing and prompted further investigation into the cause of the cracking around the bolt hole. Disassembly of the failed specimens showed that the insulators were loose and could be easily removed from the bolt hole. The vinyl coating applied to the insulator-specimen interface appeared to have prevented the widespread pitting around the bolt hole. Images of Batch 2 specimens can be seen in section 4.4.1.5.

The only remaining explanation for the cracking at the bolt holes was that the stress on the curved U-bend surface was not high enough to initiate cracking there and hence cracking occurred at the holes due to the stress created by the fastened bolt. This led to a review of the bending procedure used for bending the specimens into the U-shape. A review of ASTM G30 was also conducted to gain insight into the possible cause. ASTM G30 provided a possible answer to the problem. In the case of a two-stage stressing operation the first stage forms the approximate U-shape before allowing the elastic strain to relax completely. The second stage then involves applying the test stress to the specimen. The test strain applied can be a percentage of the elastic strain produced during the first stage of stressing (point X in Case A of Figure 4-36) or it can be involve additional plastic strain (point X in Case B of Figure 4-36).

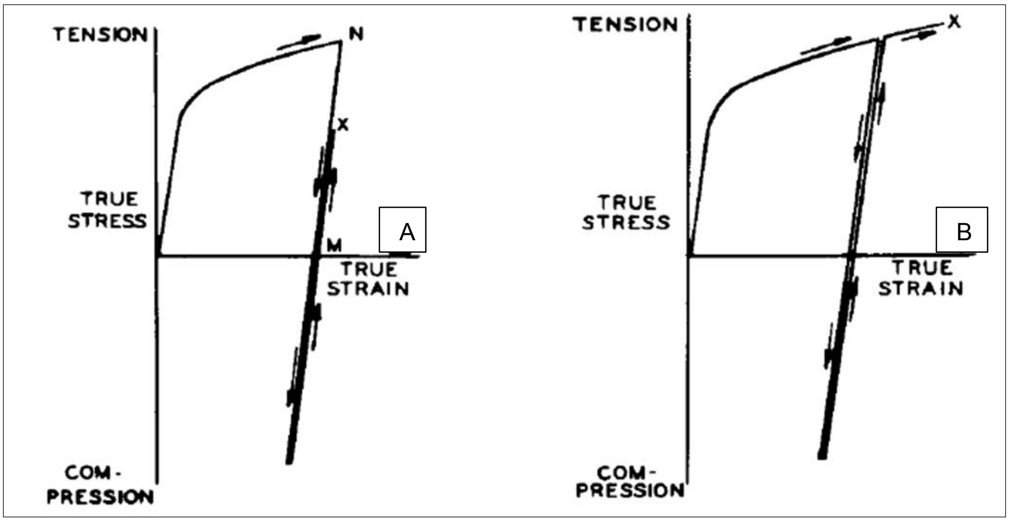

Figure 4-36: True stress-true strain relationships for U-bend specimens from ASTM G30 (69).

While stressing the specimens, it was hoped that the stress conditions in Case B of Figure 4-36 would be achieved resulting in a higher applied test stress. However, after the results of both Batch 1 and Batch 2, it was apparent that the bending procedure used produced either a very low final tensile stress or possibly even a compressive final stress at the top of the U-bend curve. This was possibly due to the amount of prestressing being too great resulting in more “springback” in the U-bend legs. This would then cause greater strain relaxation, producing very low tensile or possibly even compressive stresses in the U-bend curved surface depending on the amount of springback achieved. This was thought to be the cause of the specimens in Batch 1 and Batch 2 cracking at the bolt holes. To prove this assumption a third batch of six specimens was tested.

4.4.1.3 Modified U-bend failures

The bending procedure used to form the U-bend shape was changed to prevent excessive prestraining of the specimen before final assembly. In addition to this a new specimen geometry was adopted as seen in Figure 4-37. The new specimen geometry reduced the width of the middle section where the specimen bends. This was done to encourage cracking in the reduced width section due to the smaller ligament length. As a result of the reduced middle section, the width of the specimen around the bolt holes was increased slightly to provide adequate distance between the bolt hole and the edges of the specimen. The modified U-bend specimens were prestressed using the same rig as in Batches 1 and 2. However, the specimens were bent to a shallower angle of approximately 80° between the U-bend legs when compared to the previous batches. This resulted in significantly less strain and consequently less springback in the specimens. Stage two of the stressing procedure utilized a portable clamp. This was done to ensure that no springback would occur during the final stressing and assembly operation. The prestressed specimens were inserted into the clamp and a clamping force was exerted on the bottom of the specimen legs which caused the angle between the legs to decrease as the clamp was tightened. Once the specimen legs were a few degrees from being parallel to each other, the insulators, bolt and nut were inserted as seen in Figure 4-38. The bolt was then tightened continuously until the specimen legs were parallel and the specimen could be removed from the clamp.

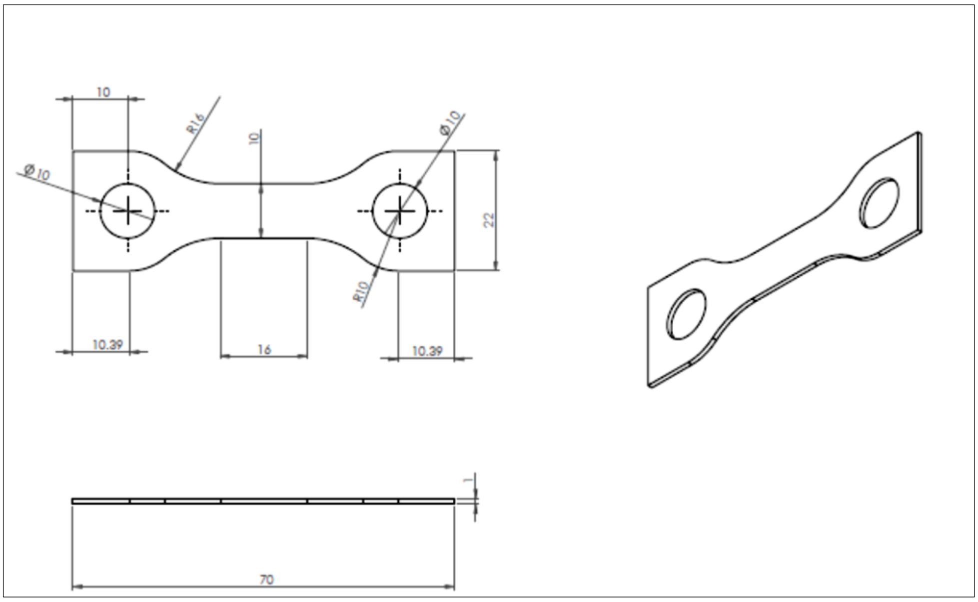

Figure 4-37: Modified U-bend specimen geometry.

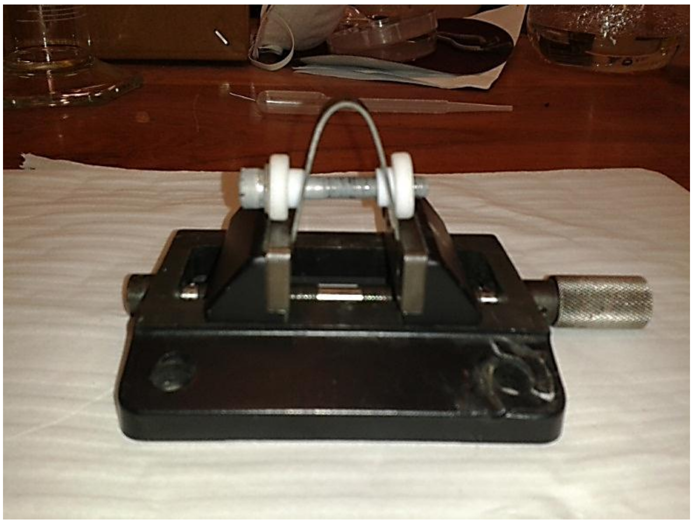

Figure 4-38: Second stage specimen bending using a portable clamp.

The modified U-bend specimens performed similarly to Batches 1 and 2 in terms of the time to failure and the order in which the specimens failed. The S430 specimen cracked earlier than in Batches 1 and 2 at 42 hours. The S450 and S470 specimens cracked in very close succession to one another while the S600 specimen showed no signs of cracking after more than 3600 hours. The results for the modified specimens can be seen in Table 9. The changes made to the specimen geometry and the bending procedure was successful in initiating cracks on the curved U-bend surface in all the modified specimens. Images of the modified specimens can be seen in section 4.4.1.5.

4.4.1.4 Time to Failure Results for Batch 1, Batch 2 and Modified U-bend specimens

Specimen	**Batch 1** **Time-to –failure (hours)**	**Batch 2** **Time-to-failure (hours)**	**Modified** **Time-to-failure (hours)**
S430	64	69	42
S450	99	143	323
S470	185	277	330
S500	489	343	474
S545	1462	2091	1615
S600	489	5177*	3629*

Table 9: Time-to-failure results for the three batches of U-bend specimens.
(* indicates no cracking)

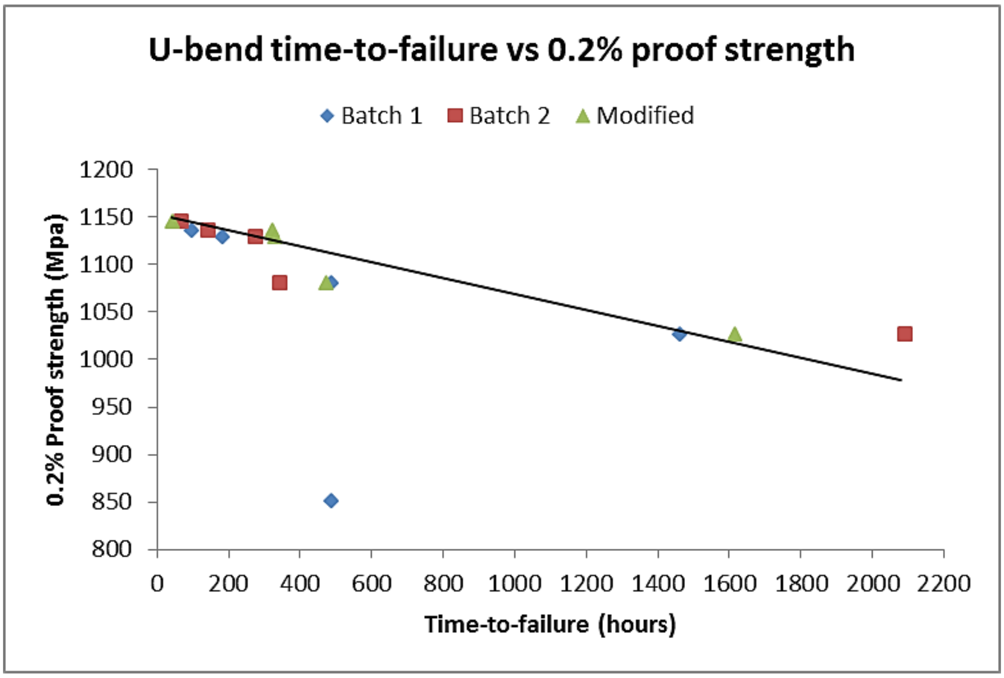

Figure 4-39: Relationship between proof strength and time-to-failure of U-bend specimens.

All three batches of U-bend specimens showed a similar trend regarding their time-to-failure. Specimens heat treated to the lower temper temperatures cracked sooner than specimens heat treated to higher temper temperatures. The S430 specimen was the most susceptible to cracking while the S600 specimen was the least susceptible. Figure 4-39 shows the relationship between the specimen 0.2% proof strength and their time-to-failure for all three batches. It can be seen that there is a definite trend of increasing time-to-failure as the proof strength of the specimens decrease. The one outlying data point which did not follow the general trend curve was for the S600 specimen from Batch 1 which failed prematurely. This was probably due to the bending operation and tight tolerance between the insulator and the bolt hole which created a high stress concentration in that area resulting in early failure.

4.4.1.5 Crack appearance and location for Batch 1, Batch 2 and Modified specimens

Batch 1 U-bends

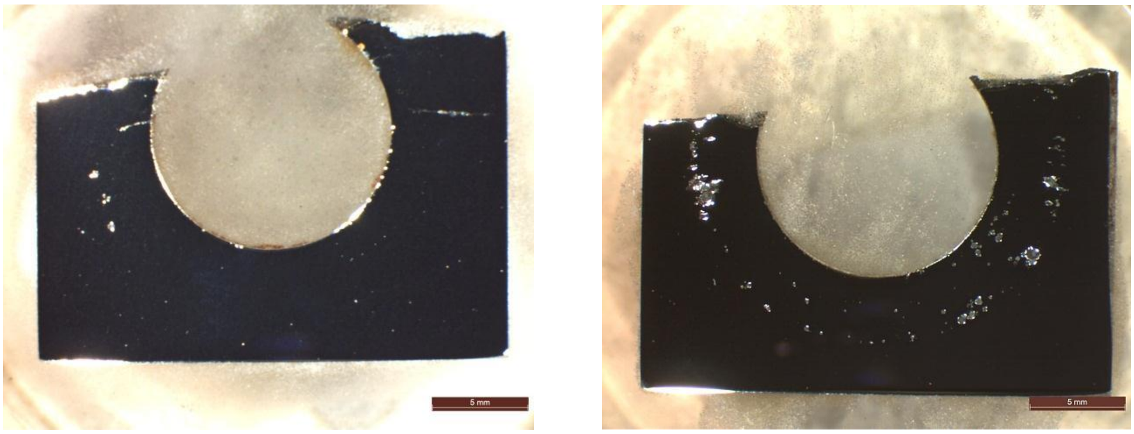

Figure 4-40: Batch 1 U-bend specimens mounted in resin and polished showing location of cracks and pitting around bolt hole. (Left) S430 specimen (Right) S450 specimen.

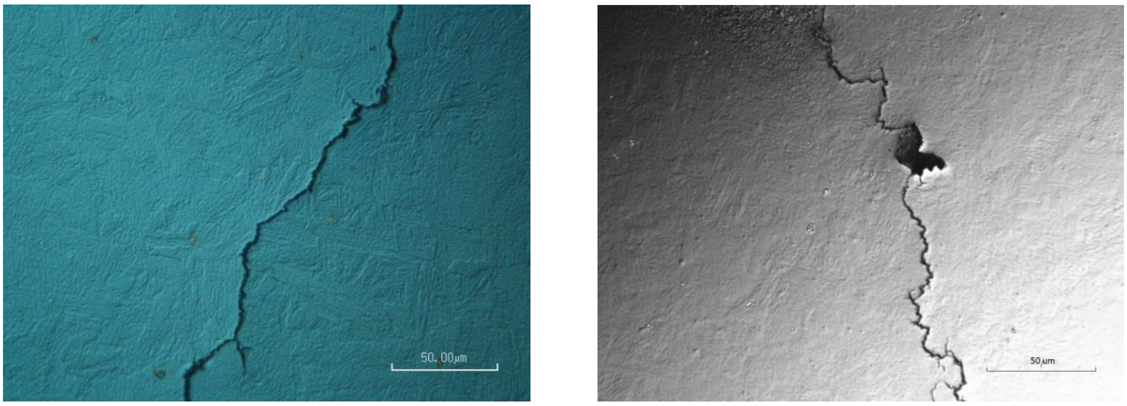

Figure 4-41: Batch 1 U-bend S430 specimen mounted and polished showing cracks around bolt hole (Left) Nomarski interference contrast mode (Right) Bright field mode showing crack initiation at a pit.

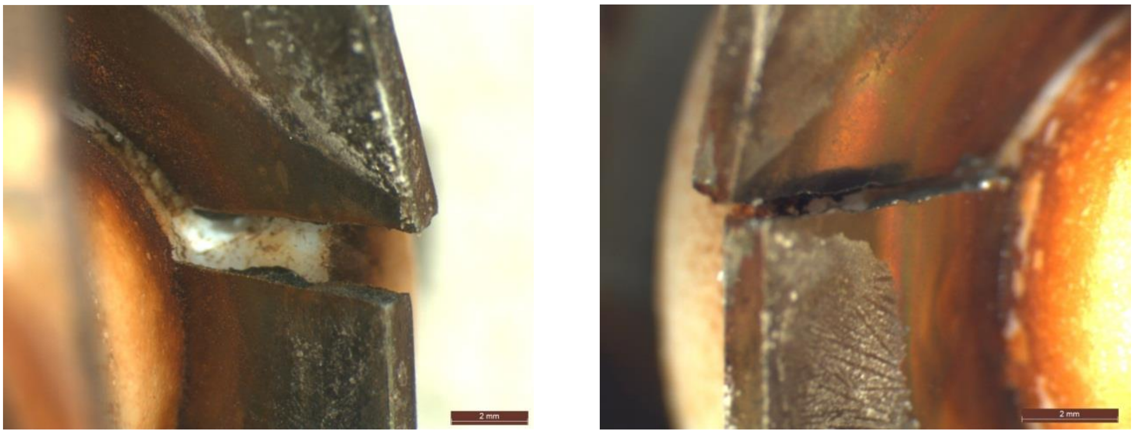

Figure 4-42: Batch 1 U-bend specimens showing cracking at bolt holes and tight clearance between specimen and insulator. (Left) S450 specimen (Right) S470 specimen.

Batch 2 U-bends

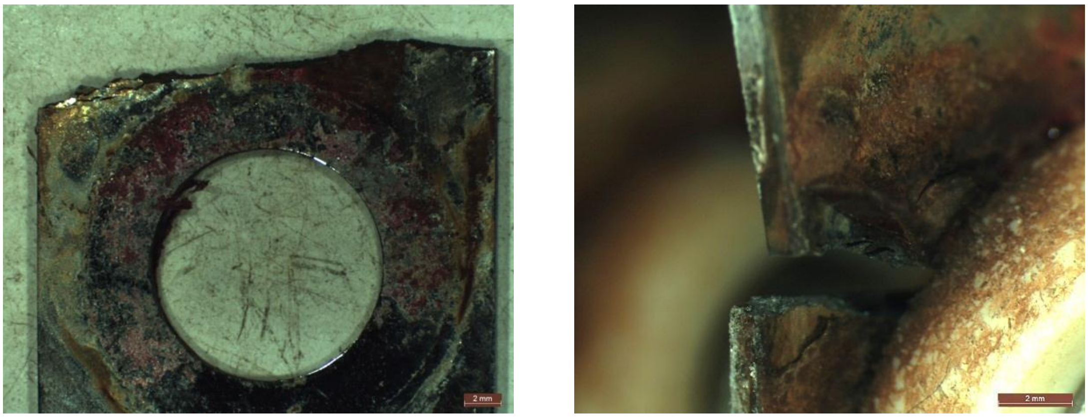

Figure 4-43: Batch 2 U-bend specimens showing locations of cracks. (Left) S430 specimen (Right) S450 specimen.

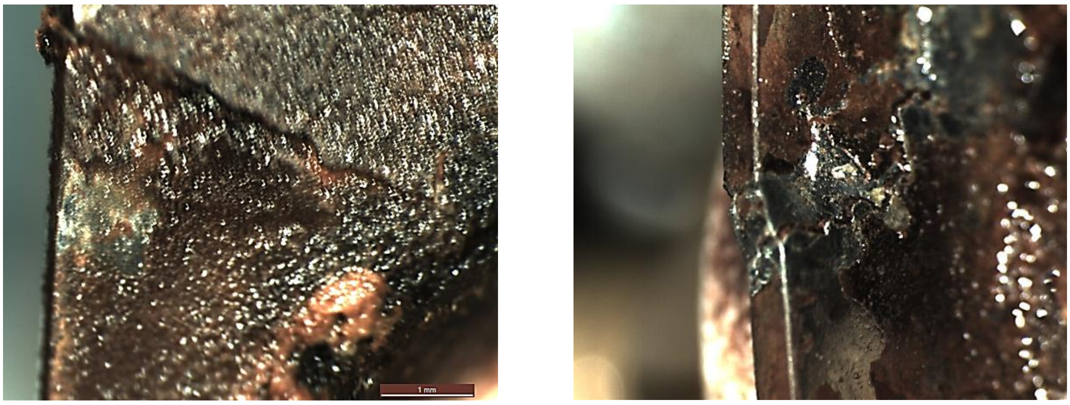

Figure 4-44: Batch 2 U-bend specimens showing locations of cracks. (Left) S500 specimen (Right) S545 specimen.

Modified U-bends

Figure 4-45: Modified U-bend specimens showing locations of cracks. (Left) S430 specimen (Right) S470 specimen.

Figure 4-46: Modified U-bend specimens. (Left) S470 specimen showing crack branching (Right) S500 specimen showing single crack on U-bend surface.

4.4.1.6 U-bend SEM Fractography

U-bend fracture surfaces were viewed in the SEM to qualitatively analyse crack growth and crack morphology. The fractography images revealed the dominant fracture mode to be intergranular stress corrosion cracking (IGSCC) along prior austenite grain boundaries. The fracture surfaces of the S545 and S600 specimens differed somewhat from the lower tempered specimens. They indicated clear signs of secondary cracks or crack bifurcation through the thickness of the specimen. The specimens that took longer to crack showed greater post-cracking corrosion deposits on the fracture surfaces which proved difficult to remove completely. The SEM images for the U-bend specimens can be seen in Figures 4-47 to 4-55.

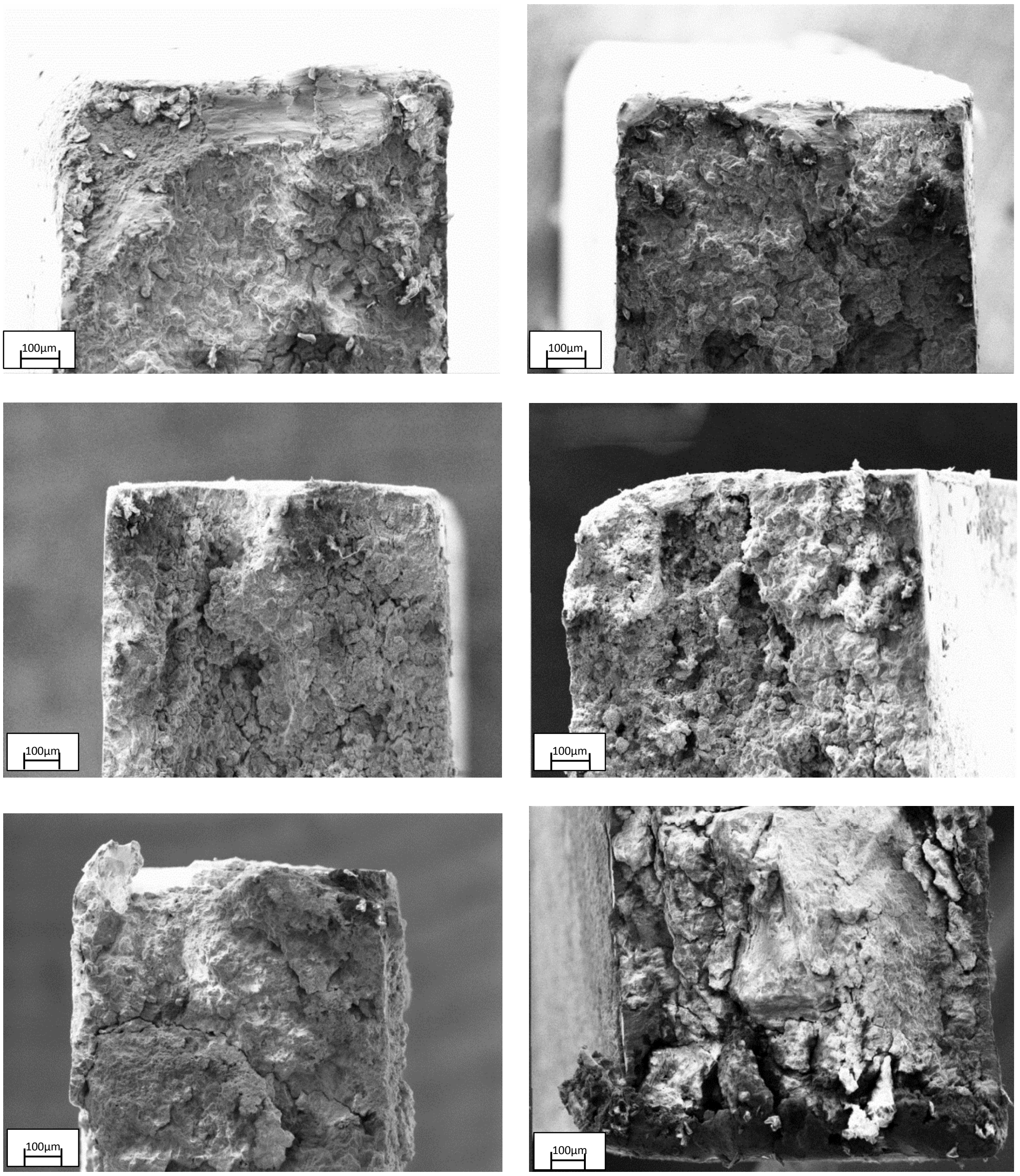

Figure 4-47: Comparison of fracture surfaces of U-bend specimens.

Clockwise from top left: S430, S450, S500, S600, S545, S470.

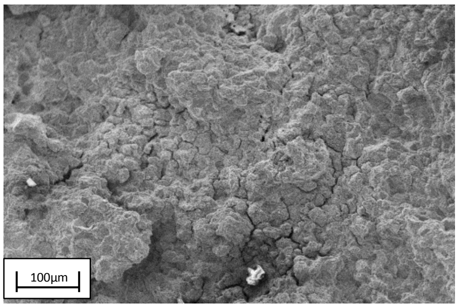

Figure 4-48: S430 U-bend specimen showing intergranular SCC on fracture surface.

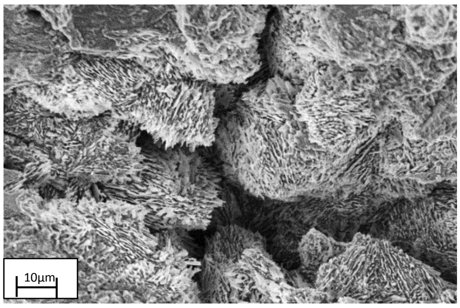

Figure 4-49: S430 U-bend specimen showing intergranular SCC on fracture surface under high magnification.

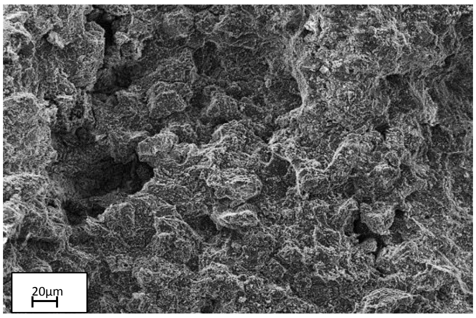

Figure 4-50: S450 U-bend specimen showing intergranular SCC on fracture surface.

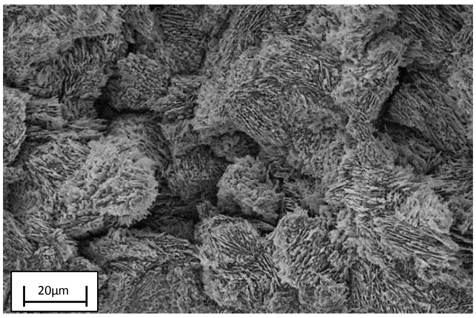

Figure 4-51: S450 U-bend specimen showing intergranular SCC on fracture surface under high magnification.

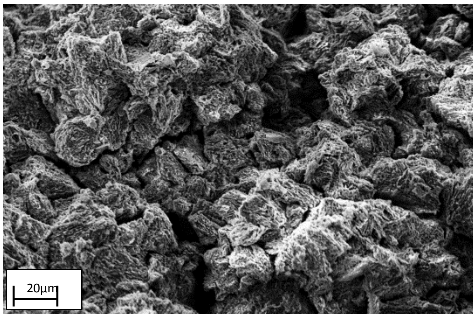

Figure 4-52: S470 U-bend specimen showing intergranular SCC on fracture surface.

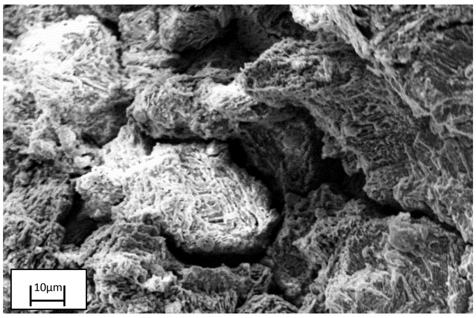

Figure 4-53: S500 U-bend specimen showing intergranular SCC on fracture surface under high magnification.

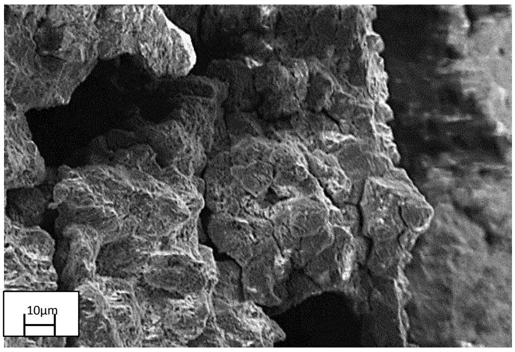

Figure 4-54: S545 U-bend specimen showing intergranular SCC on fracture surface.

Figure 4-55: S600 U-bend specimen showing intergranular SCC on fracture surface.

4.4.2 SCC Threshold Stress Intensity Results

Threshold stress intensity testing was conducted using precracked wedge open loading (WOL) specimens to determine the variation in SCC crack growth rate as a function of instantaneous stress intensity. The use of the constant deflection or crack arrest test specimen ensures that both the crack growth rate and corresponding stress intensity decrease as the crack propagates. This will continue until the crack stops propagating at which point the measured stress intensity will be the threshold stress intensity for SCC, K_{ISCC}.

WOL specimens were loaded to the initial stress intensity (K_{I0}) values which were predetermined based on the tensile strength of the heat treatment condition as well as results from tests conducted on similar materials. The K_{I0} values therefore varied according to the heat treatment condition of the test specimens. The loaded specimens were then fully immersed in the test environment (3.5% NaCl solution at 90°C) and monitored for crack growth.

Specimens were divided into batches of six specimens each, one specimen per heat treatment condition listed in Table 4, in each batch.

4.4.2.1 Batch 1 WOL Specimens

The first batch of specimens was prepared and fatigue precracked as outlined in sections 3.5.3.1 and 3.5.3.2. Loading of the specimens was initially done in a vice but problems were experienced with shearing of the bolts as they were tightened in the specimen. The bolts sheared below the bolt head before the required load could be applied to the specimen. This proved concerning as the testing could not be done if the bolts were shearing. Even if the correct load could be applied, shearing of the bolt head would have made removal of the sheared bolt from the specimen difficult at the conclusion of the test. This would have prevented the calculation of the threshold stress intensity which required unloading of the specimen. It was initially thought that the strength of the bolts was not high enough to load the heat treated specimens even though the bolts were manufactured from the same material. The bolts were subsequently heat treated to a condition that would provide higher strength. The specimens were then loaded with the heat treated bolts but shearing still occurred. This required a review of the loading procedure used in order to prevent further shearing of the bolts.

After investigating different methods of loading the specimens, it was decided to wedge the notch mouth open as the bolt was tightened into the specimen. This was expected to prevent any excessive torque on the bolt during loading. To accomplish this, a wedge was manufactured which could fit in the notch but would not prevent the bolt from being tightened against the reaction pin. The force required to wedge the notch mouth open was provided by the load cell in the ESH fatigue testing machine. The load was applied to the top of the lubricated wedge which then forced the notch mouth open. This then allowed the bolt to be tightened. Knife edges were attached to the specimen and a clip gauge was fitted to measure the crack mouth opening displacement (CMOD). Due to the wedge loading arrangement, the clip gauge had to be fitted from the side. Because of this there had to be a few cycles of loading and unloading in order to get an accurate CMOD reading with the clip gauge fitted from the top. The loading cycles were always kept to a minimum and never exceeded three cycles. Loading was also done gradually to ensure that the load applied by the bolt was always increasing and the CMOD never decreased during the unloading cycle. The loading arrangement can be seen in Figure 4-56. This loading procedure allowed the specimens to be loaded to the correct initial applied stress intensity, K_{I0}. The K_{I0} values for Batch 1 can be seen in Table 10.

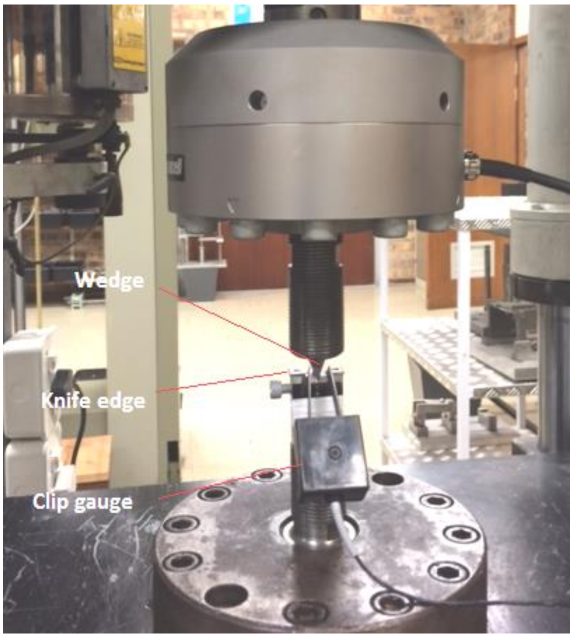

Figure 4-56: Loading of WOL specimen in the fatigue testing machine using a wedge.

Specimen	Applied Stress Intensity (K_{I0})
S430	63.5 MPa√m
S450	66.3 MPa√m
S470	71 MPa√m
S500	123 MPa√m
S545	135 MPa√m
S600	144.5 MPa√m

Table 10: Applied stress intensity values for Batch 1 WOL specimens.

Crack growth in the specimens was preceded by an incubation period. The duration of this incubation period increased with increasing temper temperature of the specimens. The S430 specimen was the first to show crack growth after an incubation period of 190 hours. The location of the crack, however, was unexpected. The crack initiated from the reaction pin-specimen interface and not from the precrack as expected. The propagation of the crack from the reaction pin was fast and reached the edge of the specimen in approximately 96 hours. There were no indications of cracking at the precrack. Figure 4-57 shows cracking from the reaction pin to the specimen edge for the S430 specimen. The S450 and S470 specimens showed similar results with crack initiation at the reaction pin and no change at the precrack. The incubation periods were longer and the crack took longer to propagate to the specimen edge hence crack propagation was dependent on temper temperature of the specimens. In all three cases the crack initiated at the interface of the reaction pin with the specimen. Due to the load being applied by the bolt against the reaction pin, a high stress concentration was generated at the reaction pin-specimen interface. It was thought that this high stress concentration was the reason for crack initiation in this region. The cracks propagated at an angle of approximately 45-55° to the load line in all three specimens. It was not clear why the cracks propagated in this fashion considering there was already a known defect in the specimen in the form of the stressed precrack at the notch tip. There was no crack propagation in the S500, S545 and S600 specimens after 1000 hours.

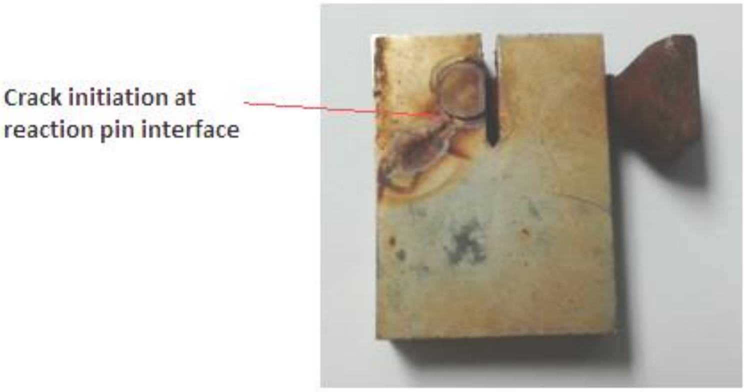

Figure 4-57: Batch 1 S430 WOL specimen showing crack propagating from reaction pin interface.

4.4.2.2 *Batch 2 WOL specimens*

A second batch of three specimens was manufactured to replace the three specimens from Batch 1 which cracked at the reaction pin. Efforts were made to understand what was causing crack initiation at the reaction pin. It was thought that the reaction pin, bolt and specimen needed to be insulated from each other during testing. This was done using a neoprene waterproof polymer-based paint. The bolts and reaction pins and specimen-reaction pin interfaces of the three new specimens were coated in neoprene paint. The specimens were wedge-loaded in the same manner as the Batch 1 specimens and immersed in the test environment. The initial applied stress intensities for the Batch 2 specimens can be seen in Table 11. The changes made to the Batch 2 WOL specimens succeeded in preventing crack initiation at the reaction pin interface. Cracks initiated from the precrack in all three specimens after an incubation period which varied between specimens.

Specimen	Applied Stress Intensity (K_{I0})
S430	55 MPa√m
S450	68.8 MPa√m
S470	67.8 MPa√m

Table 11: Applied stress intensity values for Batch 2 WOL specimens.

Batch 2 S430 WOL specimen

The S430 specimen started cracking after 115 hours in the test environment. The crack path was fairly straight and parallel to the longitudinal plane of the specimen. The crack growth rate was initially high and subsequently decreased as the crack grew longer as seen in Figure 4-62. The highest crack growth rate achieved in the S430 specimen was 0.057 mm/hr. The crack propagated longer than anticipated and reached a final length, a_f, of 25.9 mm (length of machined notch from load-line plus precrack plus crack growth). This length was calculated based on an average of five measurements taken of the specimen fracture surface (precrack and stress corrosion crack only) as seen in Figure B.1-1 in Appendix B.

The threshold stress intensity calculated for the S430 specimen based on the applied load measured during unloading was 3.84 MPa√m. The relationship between crack growth rate and stress intensity for the S430 specimen can be seen in Figure 4-65.

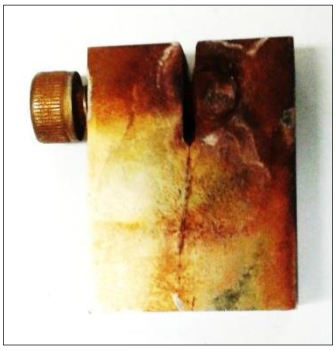

Figure 4-58: Batch 2 S430 WOL specimen showing crack path through specimen.

Batch 2 S450 WOL specimen

The crack incubation period for the S450 specimen was 255 hours. Crack initiation occurred from the precrack but the crack path was skewed at an angle of approximately 15-20° to the longitudinal plane of the specimen as seen in Figure 4-59. The crack growth rate was initially high with the highest crack growth rate of 0.07 mm/hr achieved at crack initiation. The crack growth rate subsequently decreased as the crack length increased. The crack length as a function of test time can be seen in Figure 4-63. The crack propagated to a final length, a_f, of 26.9 mm from the load line when calculated from the fracture surface seen in Figure B.1-1 in Appendix B. Due to the skew crack path, the crack length measured could have been slightly underestimated as the fracture surface was measured normal to the specimen width.

The threshold stress intensity calculated for the S450 specimen based on the applied load measured during unloading was 3.46 MPa√m. The relationship between crack growth rate and stress intensity for the S450 specimen can be seen in Figure 4-66.

Figure 4-59: Batch 2 S450 WOL specimen after fracture.

Batch 2 S470 WOL specimen

The crack incubation period for the S470 specimen was 336 hours. The crack propagated at an angle of approximately 5-7° to the longitudinal plane of the specimen. Crack growth rate was lower than in the S430 and S450 specimens with the highest crack growth rate at 0.012 mm/hr as seen in Figure 4-64. Due to the slow nature of the crack growth rate, the crack did not arrest completely before the test was concluded. Therefore a threshold stress intensity could not be determined for the S470 specimen in Batch 2.

4.4.2.3 Modified WOL specimens

Based on how the WOL specimens in Batches 1 and 2 performed, it was decided to modify the WOL specimen geometry. The specimen was modified by removing the reaction pin and corresponding slot into which the pin fits. The loading bolt would therefore be fastened directly against the face of the notch to apply the load to the specimen. By doing this, it was hoped that crack growth would initiate from the precrack and nowhere else. Removing the reaction pin, however, presented a problem with regards to growing the fatigue precrack in the specimen. Since the reaction pin was removed and the bolt was fastened directly against the notch face, the threaded hole used to grip the specimen in the fatigue testing machine also had to be removed. This was overcome by making the specimen longer above the load line and adding two additional threaded holes which would be used for gripping the specimen in the fatigue machine to grow the precrack. Once the precrack was grown, the additional holes would be removed leaving the specimen with its original dimensions.

An additional problem which needed to be overcome was the crack propagating skew through the specimen. The addition of side grooves on both faces of the specimen from the tip of the notch to the bottom edge of the specimen was made to ensure straight crack growth. The modified WOL specimen geometry can be seen in Figure 4-60.

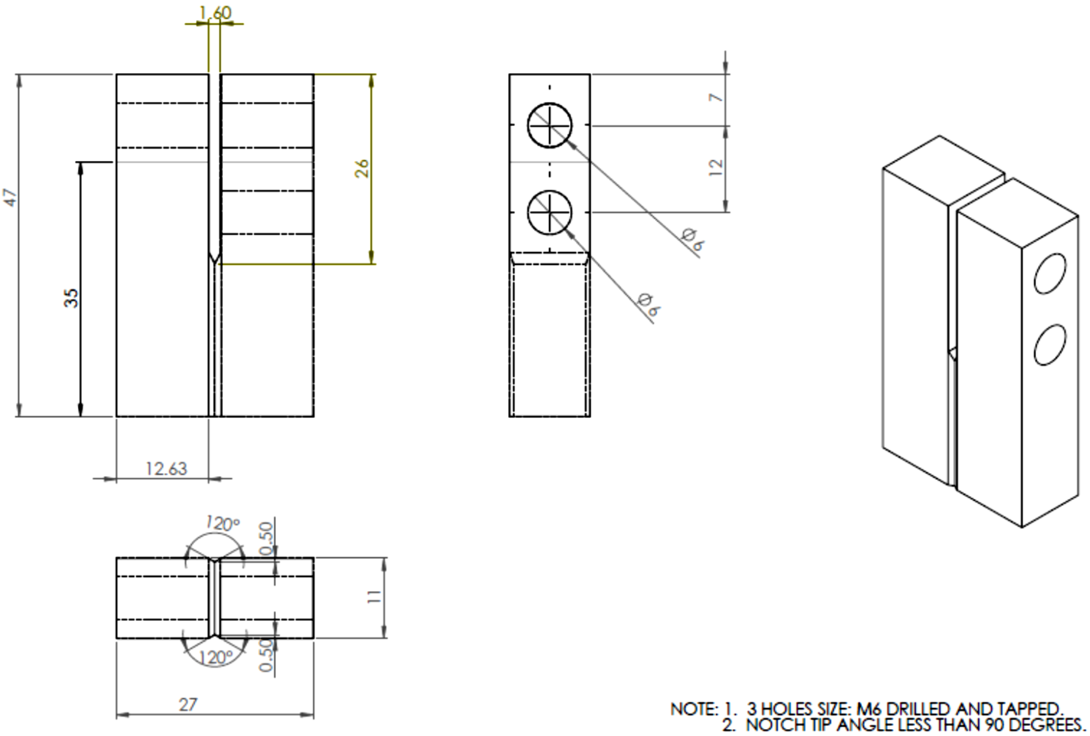

NOTE: 1. 3 HOLES SIZE: M6 DRILLED AND TAPPED.
2. NOTCH TIP ANGLE LESS THAN 90 DEGREES.

Figure 4-60: Modified WOL specimen geometry.

Only six modified WOL specimens were manufactured due to material constraints. Modified WOL specimens were wedge-loaded to the initial applied stress intensities listed in Table 12 and immersed in the test solution. After 2000 hours, only three specimens showed crack growth viz. S430, S450 and S470 specimens. The other three specimens (S500, S545 and S600) showed no indications of crack growth. This was consistent with the results achieved in the Batch 2 WOL specimens. The results of the cracked specimens will be discussed below.

Specimen	Applied Stress Intensity (K_{I0})
S430	65 MPa√m
S450	69 MPa√m
S470	73.5 MPa√m
S500	86 MPa√m
S545	104.4 MPa√m
S600	113.5 MPa√m

Table 12: Applied stress intensity values for Modified WOL specimens.

Modified S430 WOL specimen

The S430 specimen started cracking after 89 hours in the test environment. The crack path was aided by the side grooves with the crack propagating straight and parallel to the longitudinal plane of the specimen. The crack growth rate was initially high and subsequently decreased as the crack grew longer as seen in Figure 4-62. The highest crack growth rate achieved in the S430 specimen was 0.071 mm/hr. The crack propagated longer than anticipated and reached a final length, a_f, of 27.9 mm from the loadline (calculated based on an average of five measurements taken of the specimen fracture surface as seen in Figure B.1-1 in Appendix B).

The threshold stress intensity calculated for the S430 specimen based on the applied load measured during unloading was 4.62 MPa√m. The relationship between crack growth rate and stress intensity for the S430 specimen can be seen in Figure 4-65.

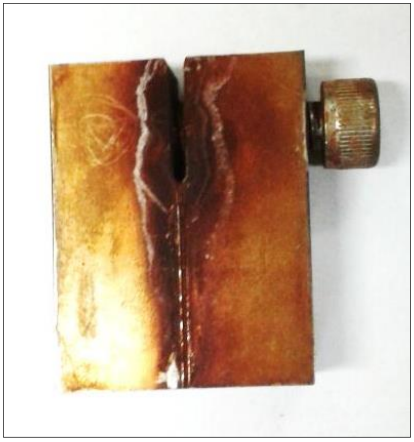

Figure 4-61: Modified S430 WOL specimen after testing.

Modified S450 WOL specimen

The S450 specimen started cracking after 183 hours in the test environment. The crack path initially followed the groove but after approximately 3 mm the crack exited the side groove and propagated at an angle of approximately 3-5° to the longitudinal plane of the specimen. The crack growth rate was initially low but increased slightly before decreasing gradually as the crack grew longer as seen in Figure 4-63. The highest crack growth rate achieved in the S450 specimen was 0.024 mm/hr. The crack propagated longer than anticipated and reached a final length, a_f, of 25.7 mm from the load line (calculated based on an average of five measurements taken of the specimen fracture surface as seen in Figure B.1-1 in Appendix B).

The threshold stress intensity calculated for the S450 specimen based on the applied load measured during unloading was 5.27 MPa√m. The relationship between crack growth rate and stress intensity for the S450 specimen can be seen in Figure 4-66.

Modified S470 WOL specimen

The crack incubation period for the S470 specimen was 170 hours although the crack growth rate was extremely slow until after approximately 1400 hours when the growth rate was sustained at a magnitude of 10 higher than at the start. This can be seen in Figure 4-64. The crack propagated at an angle of approximately 3-4° to the longitudinal plane of the specimen and out of the side groove. The crack was only seen propagating on one side of the specimen. No indication of crack growth was seen on the other side of the specimen. Crack growth rate was lower than in the S430 and S450 specimens with the highest instantaneous crack growth rate of 0.005 mm/hr achieved. Due to the slow nature of the crack growth rate, the crack did not arrest completely before the test was concluded. Therefore a threshold stress intensity could not be determined for the modified S470 WOL specimen.

4.4.2.4 Comparison of crack growth rates and stress intensities for the Batch 2 and Modified WOL specimens

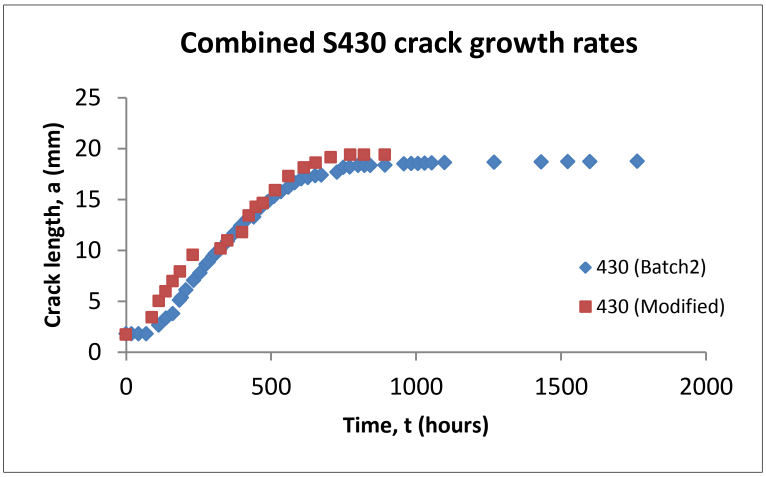

Figure 4-62: Comparison of S430 specimens crack growth rates.

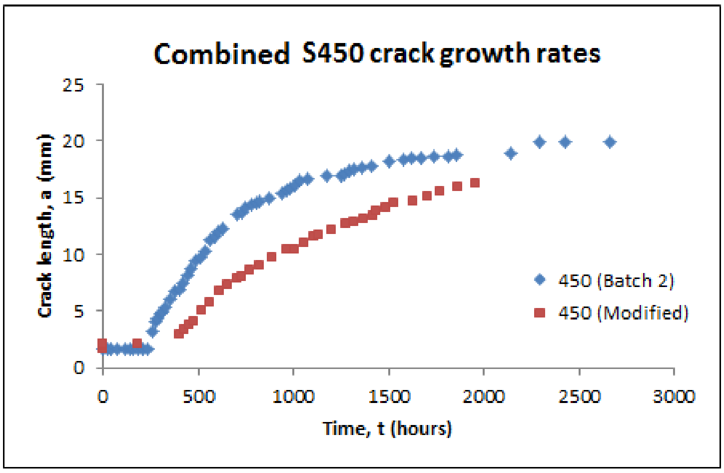

Figure 4-63: Comparison of S450 specimens crack growth rates.

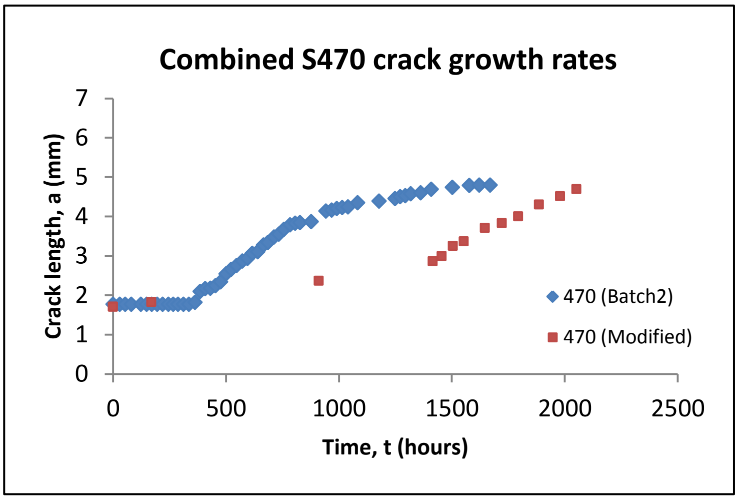

Figure 4-64: Comparison of S470 specimens crack growth rates.

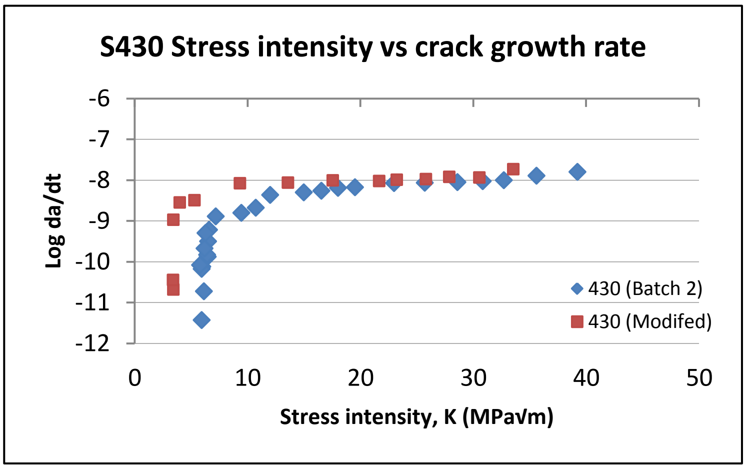

Figure 4-65: Comparison of S430 specimens stress intensity versus crack growth rate curves.

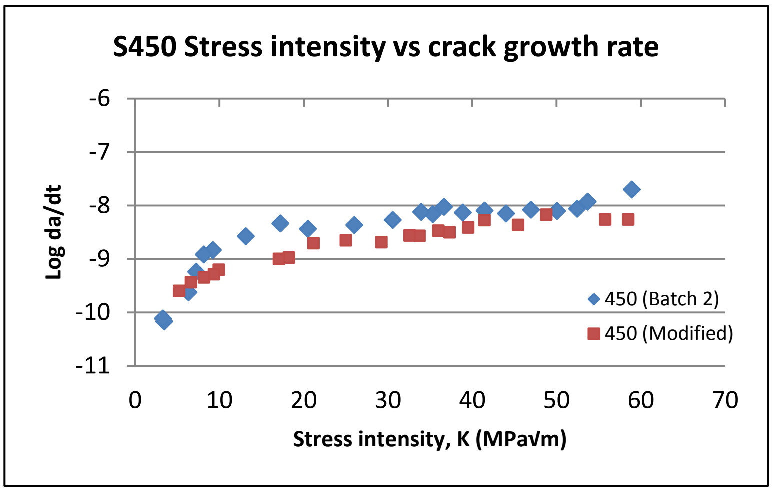

Figure 4-66: Comparison of S450 specimens stress intensity versus crack growth rate curves.

4.4.2.5 SEM Fractography of WOL specimens' fracture surfaces

Fracture surface images of the WOL specimens are displayed in Figures 4-67 to Figure 4-74 for the S430 and S450 Batch 2 specimens and in Figures B.2-1 to B.2-8 in Appendix B2 for the modified WOL specimens. The stress corrosion crack morphology for all fractured specimens followed an intergranular path along prior austenite grain boundaries as seen clearly in Figures 4-69 and Figure 4-73 for the two heat treatment conditions. A corrosion product layer was formed on the fracture surfaces due to the extended duration of the SCC tests and proved difficult to completely remove even after ultrasonic cleaning as seen in Figure 4-67. The transition from fatigue precrack to IGSCC can be distinctly seen in Figure 4-67 and Figure 4-71.

<u>S430 Batch 2 specimen</u>

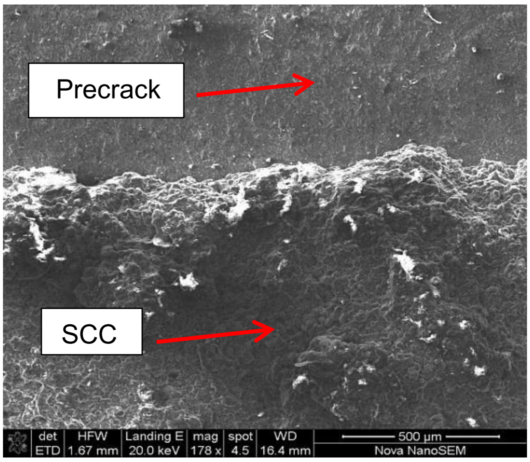

Figure 4-67: S430 Batch 2 WOL specimen showing start of SCC from precrack.

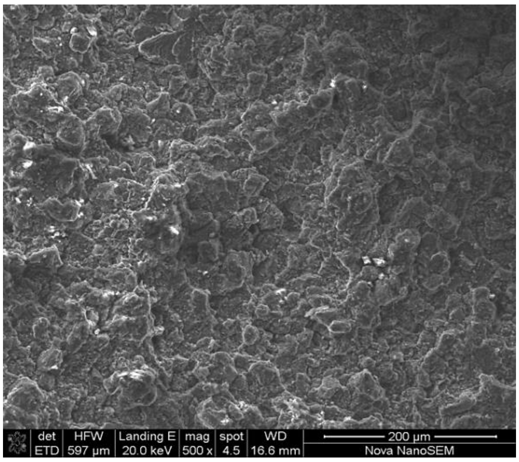

Figure 4-68: S430 Batch 2 WOL specimen showing intergranular SCC on fracture surface.

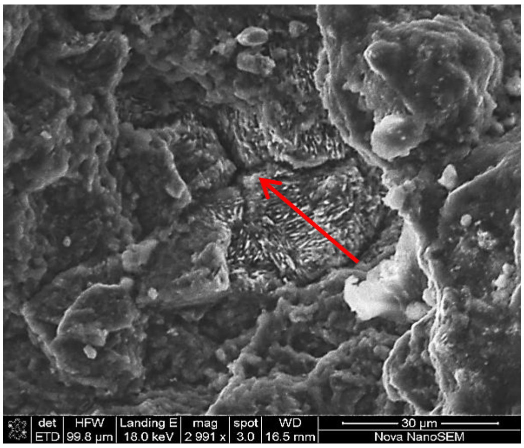

Figure 4-69: S430 Batch 2 WOL specimen showing separation along grain boundaries.

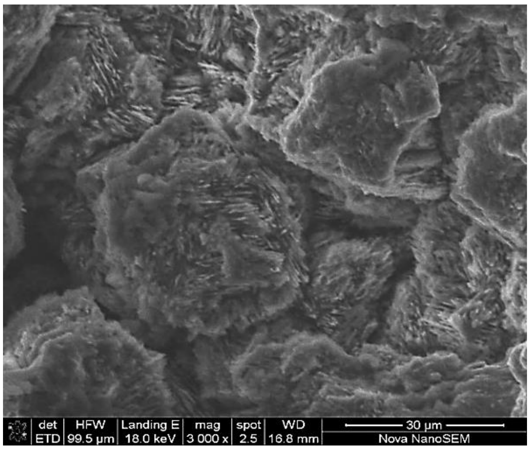

Figure 4-70: S430 Batch 2 WOL specimen showing intergranular SCC in high magnification.

S450 Batch 2 specimen

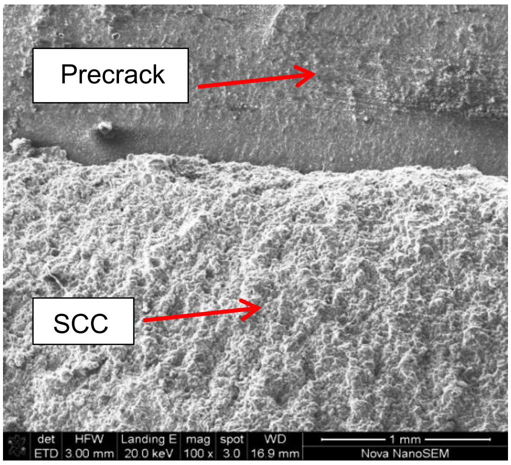

Figure 4-71: S450 Batch 2 WOL specimen showing start of SCC from precrack.

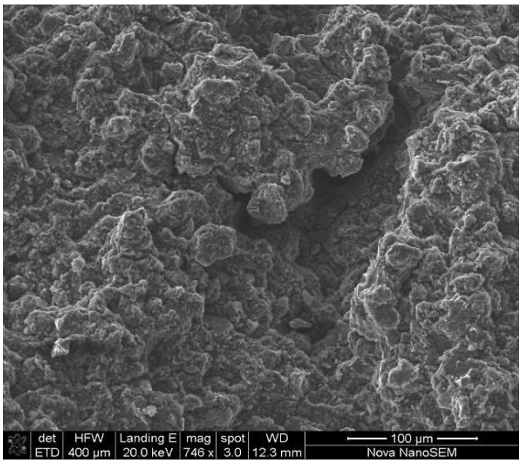

Figure 4-72: S450 Batch 2 WOL specimen showing intergranular SCC.

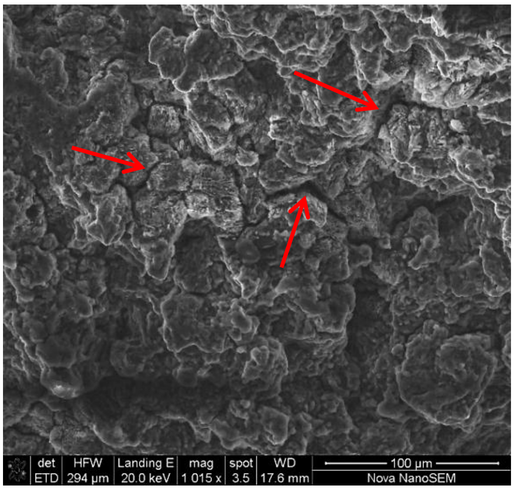

Figure 4-73: S450 Batch 2 WOL specimen showing separation along grain boundaries.

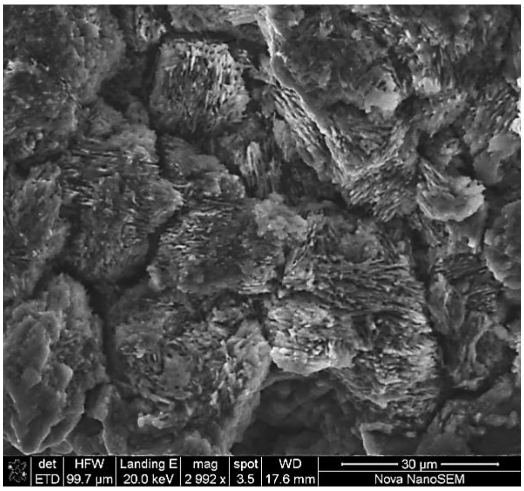

Figure 4-74: S430 Batch 2 WOL specimen showing intergranular SCC in high magnification.

5 Discussion

5.1 Influence of Heat Treatment on Material Microstructure

Six different heat treatment conditions of FV520B were tested. The distinction in the six heat treatment conditions resulted from the variation in precipitation hardening (PH) temperature during the heat treatment cycle as seen in Table 4. Light microscopy and electron microscopy (SEM and TEM) revealed the presence of Cr-rich precipitates along prior austenite grain boundaries in all six heat treatment conditions. The Cr-rich precipitates are most probably of the Cr_7C_3 or $Cr_{23}C_6$ (which replaces Cr_7C_3 at higher PH temperatures) variety based on elemental analysis although precipitate crystal structure was not investigated. The propensity, quantity and size of the Cr-rich precipitates found along the prior austenite grain boundaries increased as the specimen PH temperature increased as seen in the TEM results of section 4.3.6. which confirmed the results in earlier light micrographs in section 4.3.1. It must be noted that these TEM results were obtained from a limited number of specimens of limited specimen size.

SEM and TEM results for the different heat treatment conditions also revealed the presence of niobium carbide (NbC) precipitates in the material matrix. These precipitates appear to have formed during the Solution Treatment step in the heat treatment regime at 790°C. They were observed as rod-like particles orientated at preferred crystallographic planes and dispersed throughout the microstructure. The presence of NbC precipitates contributed to the high strength levels through dispersion strengthening as seen in the hardness and tensile test results in section 4.2.

Dilatometry and x-ray diffraction (XRD) results showed the presence of reverted austenite in the microstructures of the S545 and S600 specimens. This was due to the PH temperature for these specimens being very close to the Ac_1 temperature of 600°C obtained through dilatometry. Quantitative phase analysis of the XRD spectra in section 4.3.5.1. revealed that the S545 specimen contained 4.2% and the S600 specimen contained 20.8% of reverted austenite by volume fraction respectively. This led to the conclusion that tempering at a temperature above approximately 500°C increases the amount of reverted austenite in the microstructure upon cooling which is consistent with the close proximity to the Ac_1 temperature. The fact that the austenite does not transform to martensite during cooling is due to the enrichment of austenite stabilising elements that occurs during element partitioning associated with the diffusion-controlled austenite reversion reaction. Reverted austenite is a lower strength phase than lath martensite therefore a greater quantity of reverted austenite within the microstructure will result in a reduction in strength.

5.2 Mechanical Testing

Hardness and tensile test results for the six heat treatment conditions revealed a clear correlation between PH temperature and material hardness and strength. It was seen that increasing the PH temperature reduces the hardness and strength as seen in Figure 4-4 and Figure 4-6. This decrease is due to the effects of over-ageing which occurs during the PH heat treatment stage. During this stage, solid solution strengthening is replaced by precipitation strengthening at the lower temperatures. However, as the PH temperature increases, the precipitates coarsen and become ineffective in strengthening which leads to a softening of the matrix and a decrease in hardness and strength. It is also quite evident that the reduction in hardness and strength is greater when the PH temperature is above 500°C. This correlates well with the XRD quantitative phase analysis results which showed that the amount of reverted austenite increased as the PH temperature increased above 500°C. The presence of reverted austenite, therefore, was shown to significantly reduce the hardness and strength in FV520B. There was, however, a good correlation between hardness and UTS with the relationship being linear for the range of PH temperatures tested as seen in Figure 4-7.

The reduction in strength as PH temperature increased resulted in a corresponding increase in ductility as seen in Table 7. The increase in ductility is due to the greater quantity of the softer phase, reverted austenite, in the microstructure as well as the increase in the number and size of Cr-rich precipitates at the higher PH temperatures.

Speidel et al. (19) have investigated the effect of yield strength on the crack growth rates in steam turbine materials. They identified two different yield strength ranges in which the crack growth rates behave differently. Below a yield strength of 1100 MPa, the stress corrosion crack growth rates are moderate, while above 1100 MPa there is a strong increase in crack growth rates with increasing yield strength. This behaviour was evident in the failure of the U-bend specimens where cracks grew much faster in the lower tempered specimens with a yield strength greater than 1100MPa and took much longer to propagate in the higher tempered specimens whose yield strength was below 1100 MPa. This would indicate the benefit of overaging provided that the strength requirements of the application can be met.

5.3 Stress Corrosion Testing

5.3.1 SCC Test Environment

The test environment used for both the U-bend and threshold stress intensity testing was the same i.e. a 3.5% NaCl solution heated at 90°C. The solution pH and temperature were monitored on a daily basis. The solution pH was measured to be the range 6.5 to 7.5 for the duration of the SCC testing. The variation in pH was due to the accumulation of corrosion products in the test solution. The test solution was therefore changed weekly No attempts to change the solution pH were made.

The solution temperature was maintained to within ±2°C during testing. Excursions in temperature occurred when the test solution was refreshed with new solution at room temperature but this transient duration until the solution reached the test temperature was insignificant considering the total duration of the SCC tests. A more significant temperature excursion occurred when the test equipment was shut off due to an unavoidable closure of the laboratory. During this period of approximately 72 hours the specimens were left in the test solution at room temperature. The specimens were then inspected before the heating mantle was switched back on. The specimens showed no signs of crack growth during the time that they were in solution at room temperature. This indicated that the stress corrosion cracking of the test specimens was heavily influenced by temperature of the test environment. This was proven previously (78) for high-strength 4340 and 300M steels where the crack growth rate varied exponentially with temperature and an activation energy of approximately 9000 cal/mole was observed for the failure process.

5.3.2 U-bend Testing

5.3.2.1 U-bend Test Specimen and Test Technique

The U-bend test specimen provides an easy and cost effective method for determining a materials resistance to SCC. The specimen is plastically deformed into a U-shape and the legs held parallel to each other by means of a bolt creating a tensile stress on the outer surface of the U-bend. The first two batches of U-bend specimens experienced cracking at the bolt holes instead of on the outer U-bend surface as seen in section 4.4.1. This was found to be due to the initial bending procedure used which deformed the specimen too much and allowed for springback in the legs of the U-bend specimen and a possible compressive stress to be developed on the U-bend curved surface. The subsequent tightening of the bolt was not enough to produce a tensile stress on the U-bend surface high enough to initiate cracking here.

Subsequent modifications to the U-bend specimen geometry and bend procedure were made to prevent the formation of a compressive stress on the U-bend surface. The specimen geometry was changed to produce a reduced width in the curved section of the specimen as seen in Figure 4-37. The bend procedure was changed to reduce the initial deformation during bending and have more deformation during the final assembly with the tightening of the bolt to ensure that a tensile stress is created on the curved U-bend surface. These modifications produced better results in terms of the location of cracks and were therefore successful in their implementation. The specimen geometry, however, would not need to be modified if the bend procedure was performed correctly and was only done to provide an additional level of confidence in the results. It is therefore very important to ensure that the bending of the test specimen is done in a manner that would ensure a tensile stress being developed on the curved U-bend surface.

5.3.2.2 *U-bend Test Results*

The U-bend specimens were tested to determine their time-to-failure which, according to ASTM G30 (69), was taken as the time at which cracks are first visible. The three batches of U-bend specimens showed a similar trend in their time-to-failure results as seen in Table 9. The susceptibility of the test specimens decreased with increasing PH temperature. The S430 specimen was the most susceptible with failure occurring after an average of 58 hours for the three batches. The S600 specimen was the least susceptible with failure in only one of the three specimen batches. This was, however, due to the way the specimen was bent and assembled and can therefore be considered an anomaly. There was no failure in the S600 specimen in the other two batches after 5177 hours and 3629 hours respectively. There was a clear correlation between the time-to-failure and the 0.2% proof strength of the specimens as seen in Figure 4-39. The specimens with the higher proof strength failed sooner and failure times increased as the specimen proof strength decreased. The presence of reverted austenite at higher precipitation hardening temperatures thus improved the SCC susceptibility of FV520B.

Schleithoff et al. (18) investigated the SCC behaviour of 13% Cr-steels used for turbine blades. Cylindrical tensile test specimens were spring loaded and immersed in various mediums. For X22CrMoV121, a stainless steel containing molybdenum and vanadium, specimens were immersed in an aerated boiling 3% NaCl solution after a quench and temper heat treatment. Specimens tempered at 420°C and 480°C failed within 2 hours while specimens tempered at 600°C failed after 100 hours. The X20Cr13 steel tested in the same environment performed better with the 420°C and 480°C tempered specimens failing after 4 hours and 2 hours respectively while the specimen tempered at 600°C failed after more than 4000 hours. The general trend in the performance of 13% Cr-steels can be seen in Figure 5-1 which shows a schematic of the relationships between the time-to-failure, temper temperature and tensile strength for 13% Cr-steels. It can be seen that the two conditions with the lowest resistance to SCC are the hardened but not tempered condition and the temper temperature range of ±450-500°C which correspond to the conditions with highest tensile strength.

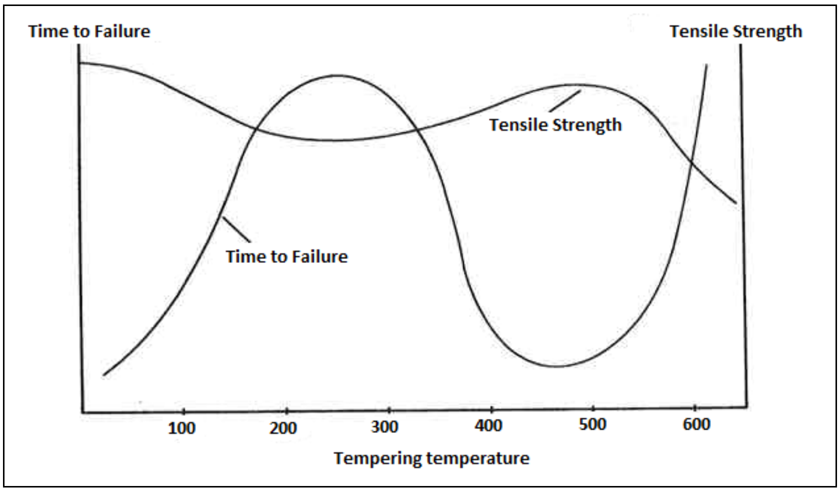

Figure 5-1: Schematic showing the relationship between time-to-failure and tensile strength for SCC of 13% Cr steels (18).

Bloom (14) investigated the stress corrosion cracking of two precipitation hardened stainless steels, 17-4 PH and 17-7 PH using U-bend specimens. In a severe marine environment, the effect of varying ageing temperature was investigated for both materials. The results showed that between ageing temperatures of 800 F (427°C) and 1000 F (538°C), which correspond to the high strength heat treatments, the 17-4 PH specimens showed decreasing susceptibility with increasing ageing temperature. The 17-7 PH specimens showed a similar trend between 850 F (454°C) and 1000 F (538°C) ageing temperatures. No cracking was observed in both materials aged above 1000 F (538°C). It can therefore be concluded that heat treatments which produce higher strength levels in the material increases its susceptibility to SCC in a corrosive environment known to cause SCC for the material.

Although U-bend tests are relatively simple to conduct, they suffer from two noteworthy limitations (78). Firstly, they cannot be used to quantitatively predict service performance, and hence can only be considered as screening tests to determine whether one material is superior to another or in this case which heat treatment condition performs better. The second limitation involves the SCC failure sequence in relation to the surface condition of the specimen. The typical SCC failure sequence involves pitting of the surface which develops into a crack. The crack then propagates to a critical length when pure mechanical fracture ruptures the remaining ligament. When smooth specimens are used, the major portion of the failure time involves the formation of the defect which leads to the initiation of the crack. This can often give misleadingly conservative results as actual service components often already contain crack initiating surface defects due to the manufacturing processes used.

5.3.3 Threshold Stress Intensity Testing

5.3.3.1 WOL Test Specimen and Test Technique

Threshold stress intensity testing was performed using precracked WOL specimens manufactured according to ASTM 1681-03 to the dimensions seen in Figure 3-13. Specimens were loaded to the initial applied stress intensity (K_{I0}) and fully immersed in the test solution.

Loading of the specimens

Difficulties were initially experienced in loading the specimens to the required K_{I0} levels. Loading bolts were shearing below the bolt head when they were tightened into the specimen. This posed a major problem as the specimens could not be loaded to the correct K_{I0} levels and unloading of the sheared bolts at the conclusion of the test would prove difficult, affecting the measurement of the CMOD.

Different methods of loading the specimens were investigated before it was decided to wedge the notch mouth open as the bolt was tightened into the specimen. A triangular wedge manufactured from high strength steel was inserted into the specimen notch mouth and a load was applied to the top face of the wedge using the load cell of the fatigue testing machine as seen in Figure 4-56. The loading bolt was then tightened as the load on the wedge increased which prevented any excessive torque on the bolt leading to shearing. The only drawback of this loading method was that the clip gauge used to measure the CMOD had to be fitted from the side of the specimen which meant that an accurate CMOD reading could not be taken. The load on the wedge had to therefore be removed to allow the clip gauge to be fitted from the top to take the CMOD reading. If the reading was too low a higher load had to be applied. This meant that the specimen was being subjected to loading cycles in the process of getting an accurate CMOD reading.

Although the loading bolt was tightened as much as possible before the load on the wedge was removed, it is possible that the removal and reapplication of the wedge load affected the stress state of the specimen at the precrack. This is discussed further in section 5.3.3.3. with respect to the crack incubation period.

Modification of the WOL specimen geometry

The first batch of WOL specimens tested experienced cracking in an unexpected fashion. Figure 4-57 shows that the crack initiated from the specimen-reaction pin interface and not at the precrack as expected. This was seen in the S430, S450 and S470 WOL specimens. The cracks propagated from the reaction pin to the edge of the specimen at an angle of 45-55°. The crack growth rates varied and were dependent on the heat treatment condition with the S430 specimen crack propagating the fastest followed by the S450 and S470 specimens respectively. This was consistent with results from the U-bend tests which showed that the SCC susceptibility increased with increasing strength and hence decreasing PH temperature.

This begs the question of why the cracks initiated at the reaction pin and not at the precrack. The interface between the reaction pin and the specimen is an area of high stress concentration due to the load applied by the bolt on the reaction pin. Additionally, the reaction pin was not heat treated and was installed in the as received material condition. Differing metallurgical conditions between the pin and the specimen could therefore have resulted in differences in corrosion potential and the formation of a local galvanic couple since the entire specimen was immersed in the test solution during testing. The occluded environment at the reaction pin-specimen interface would have then promoted the conditions necessary for pitting and the initiation and growth of the crack at this location instead of at the precrack, where the applied stress intensity would have likely been lower.

The WOL specimen geometry was subsequently changed to remove the reaction pin and have the loading bolt strike the inside face of the notch directly. This modification was successful in initiating cracking at the precrack. The addition of side grooves was another change made to promote straight crack growth normal to the load line. This modification was successful in the S430 WOL specimen where the crack grew completely in the groove, and partly successful in the S450 specimen where the crack started in the groove but propagated out at a slight angle. The S470 specimen had a crack path that was also at a small angle to the side groove. Overall, the modifications were able to rectify the problems experienced in the specimens previously.

5.3.3.2 *Selecting the Applied Stress Intensity*

The selection of the appropriate applied stress intensity, K_{I0}, is an important task and careful consideration should be given to the various factors affecting it. The ideal situation would involve knowing what the expected threshold stress intensity (K_{ISCC}) value is likely to be from previous data and loading the specimen to a higher K_{I0} value thereby controlling crack growth until K_{ISCC} is reached. This was not possible due to the limited available literature for FV520B. Therefore, the factors affecting K_{I0} were evaluated in order to select appropriate values. Metallurgical conditions are known to influence K_{ISCC} therefore it was known that K_{I0} will differ for different material conditions. Threshold stress intensity values for materials with a similar chemical composition to FV520B were found in literature. The K_{ISCC} value for FV520S (79) was 66 MPa√m at a PH temperature of 450°C while K_{ISCC} for 17-4 PH (68) varied from 51 MPa√m at the lower PH temperature to 132 MPa√m at the higher PH temperature (overaged condition).

Another factor taken into consideration was the difference between the applied stress intensity and the threshold stress intensity i.e. $\Delta K = K_{I0} - K_{ISCC}$. A larger ΔK would allow for greater crack growth but there is a danger of the crack growing to the end of the specimen making it impossible to determine K_{ISCC}. Crack incubation time is also affected by ΔK. A larger ΔK would usually lead to a shorter incubation time in most cases (80) thereby shortening the duration of the overall test which is always desirable. The threshold stress intensity, K_{ISCC}, should also meet the conditions for plane strain in the specimen. This is discussed further in section 5.3.4.

Taking the above factors into account, the K_{I0} values in Tables 10, 11 and 12 were selected with the values increasing with increasing PH temperature. From the results of the testing, it is apparent that the K_{I0} values chosen were too high in the S430 and S450 specimens. The ΔK in these specimens allowed for greater crack growth with the cracks propagating almost to the end of the specimen. The S470 specimens were still showing crack propagation when the test was ended therefore it is not known if the applied K_{I0} was too high or not. Due to zero crack propagation in the higher tempered specimens before the tests were terminated, it is unclear if the selected K_{I0} values were adequate (i.e. above K_{ISCC}) or if the specimens were simply immune to SCC. Fracture toughness tests could provide some clarity by producing K_{IC}, the plane strain fracture toughness in air. If K_{IC} is higher than the applied K_{I0}, applying K_{IC} as the applied K_{I0} in an SCC test could then prove immunity to SCC if no cracking occurs. The K_{ISCC} would then be the same as K_{IC}. Fracture toughness tests were not performed due to a limitation in test material for further test specimens.

5.3.3.3 *Crack Incubation*

The initiation of stable crack growth was preceded by a period of crack incubation in the WOL specimens which produced SCC cracks. Table 13 shows the crack incubation periods for the WOL specimens which produced SCC cracks. It can be seen that the crack incubation period extended to longer times as the PH temperature of the specimens increased. There are two possible reasons to explain this trend. Firstly, it could be due to the materials resistance to SCC increasing with increasing PH temperature and the corresponding decrease in mechanical strength. The other reason for extended crack incubation times could be due to a small ΔK as explained in the previous section. This would be due to the initial applied stress intensity, K_{I0}, being low. The fatigue crack tip surfaces are protected from the corrosive environment by a protective passive oxide layer. If the stress at the crack tip is not high enough to rupture the film and allow access of the environment to the crack tip, increased incubation times will result until such time as the film is ruptured by some other means, usually due to chemical degradation by the environment. The combination of both the materials increased resistance to SCC and the small ΔK are very likely contributing factors to the increased crack incubation times experienced during testing.

Specimens	**Batch 2 WOL crack incubation period (hours)**	**Modified WOL crack incubation period (hours)**
S430	115	89
S450	255	183
S470	336	1400

Table 13: Crack incubation periods for WOL specimens.

The wedge-loading of the WOL specimens was also thought to play a role in the crack incubation period. The application and removal of the load is comparable to the process of prestressing the specimen. Prestressing refers to the application and subsequent removal of a load on the specimen before actual testing. The specimen is thereafter loaded to the desired starting stress intensity, K_{I0}, normally. During removal of the prestress load, the crack-tip plastic zone experiences compressive stresses which will then reduce the magnitude of the crack-tip stresses upon reloading (81) thereby reducing the ΔK of the specimen. Prestressing has been shown to greatly influence crack incubation times with an increase in prestress load leading to longer incubation times (82). The difference between prestressing and wedge-loading, however, is the fact that the loading bolt was tightened during wedge-loading, and not after as in prestressing, therefore the stress state around the crack-tip should not have been radically affected by the wedge-loading process.

5.3.3.4 Threshold Stress Intensity Test Results

Cracking in the WOL specimens was only observed in the S430, S450 and S470 specimens after 2000 hours in the test environment. The crack incubation times increased with increasing specimen PH temperature as seen in Table 13. While it is clear that material susceptibility decreases as the specimen PH temperature increases, it is not apparent if the higher tempered specimens would have exhibited cracking had the test duration been extended. SCC tests conducted by Turnbull et al. (10) showed for FV566 tempered at 650°C for 4 hours, that testing times can extend well beyond 10000 hours for high tempered specimens. This, of course, would be dependent on the K_{I0} level of the specimen as well as the corrosivity of the environment. It was shown, however, that if no crack growth is observed after a given time period, gradual increases in stress intensity can be made until crack growth is seen.

The crack growth rates of the S430, S450 and S470 specimens were initially high and subsequently decreased as the crack grew longer. The highest crack growth rate observed in both the S430 and S450 specimens was approximately 0.07 mm/hr dropping to 0.012 mm/hr for the S470 specimen. Figures 4-62 to 4-64 show the change in the crack length over time for all three specimens with a comparison between batches for each one. The curves of the S430 specimens showed a distinctly similar fit while there was relatively more variation between batches for the S450 and S470 specimens' curves. It can be seen in Figure 4-64 the large difference in crack incubation times between Batch 2 and the Modified specimens for the S470 condition. The reason for the longer incubation time in the Modified specimen is unclear.

The relationship between stress intensity and crack growth rate can be seen in Figure 4-65 and Figure 4-66 for the S430 and S450 specimens respectively. It can be seen that when the crack growth rate data is plotted on a log scale, the shape of the curves resemble the curve in Figure 2-24 depicting the three distinct stages associated with SCC kinetics in precracked specimens. Figure 4-65 for the S430 specimens shows the prominence of the "plateau velocity" i.e. stage II growth after which there is a decrease in crack growth rate with very little to no change in stress intensity (stage I). Stage II cracking also takes precedence in Figure 4-66 for the S450 specimens where the plateau velocity can clearly be seen. The Batch 2 specimen shows a greater dependence of crack growth rate on stress intensity in stage I while the Modified specimen does not show a defined stage I. The presence of a plateau velocity in stage II in both material conditions indicates that the crack growth rate here is constant and independent of stress intensity due to a combination of known variables (material, environment, electrochemistry and stress) to achieve a steady state condition which will persist as long as the interaction of these variables is maintained (3).

The threshold stress intensities, K_{ISCC}, for the S430 and S450 WOL specimens can be seen in Table 14. It can be seen that the calculated values are quite low. This was, however, expected based on the results of the susceptibility U-bend tests which showed that these two material conditions are the most susceptible to SCC in the test environment. The threshold stress intensity for the S450 Batch 2 specimen was lower than for the S450 Modified specimen. However, crack propagation in the Batch 2 specimen was significantly skew, as seen in Figure 4-59, and this would have undoubtedly affected the calculation of the threshold stress intensity. Therefore the S450 Batch 2 threshold stress intensity result would not be considered valid due to the crack propagating at an angle greater than 10° to the machined notch.

The threshold stress intensities were also checked against the plane strain validity criteria:

$$B,\ a,\ (W-a) \geq 2.5\left(\frac{\quad}{\quad}\right)$$

and all four specimens were found to have met this criteria as seen in Table 14. This was further verified by examination of the specimen fracture surfaces as discussed in section 5.3.4.2.

Parameter	S430 (Batch 2)	S430 (Modified)	S450 (Batch 2)	S450 (Modified)
B [mm]	11.08	11.03	11.05	11.07
a_f [mm]	25.9	27.9	26.9	25.7
$W-a_f$ [mm]	2.1	0.1	1.1	2.3
K_{ISCC} [MPa√m]	3.84	4.62	3.46	5.27
$2.5\left(\frac{KISCC}{\sigma y}\right)^2$ [mm]	0.0282	0.0408	0.0189	0.0438

Table 14: Threshold stress intensities and plane strain validity.

Turnbull et al. (10) reported threshold stress intensities for two turbine blade steels, FV566 and PH 13-8 both tested in a 35 ppm chloride solution at 90°C. For FV566 tempered at 650°C, K_{ISCC} was in the region of 16-20 MPa√m while for the PH 13-8 material the threshold was approximately 21-25 MPa√m. Although being higher than the calculated stress intensities for FV520B, it must be mentioned that the test environment used by Turnbull et al. was significantly less corrosive than that used in this project. The metallurgical conditions tested also differed significantly making a direct comparison difficult.

The effect of heat treatment condition on threshold stress intensity for 17-4 PH in a 20% NaCl environment was investigated previously (83). It was seen that in the H900 condition (tempered at 480°C) the K_{ISCC} was 40.3 MPa√m compared to 100 MPa√m in the H1150 condition (tempered at 620°C). This indicates that over-ageing greatly improves the stress corrosion performance of precipitation hardened stainless steels in chloride environments.

5.3.4 Fracture Surfaces and Crack Morphology

5.3.4.1 Crack Branching

Crack branching from the primary crack was only observed in the S450, S470, S500 and S545 U-bend specimens. Macrobranching, i.e. the macroscopic crack separation into two or more diverging elements, was observed in all cases. The degree of crack branching was found to decrease as the specimen PH temperature increased. The two factors postulated by Carter (54) as being necessary for crack branching to occur are constant crack velocity and a critical stress intensity. Rapid acceleration during the initial stages of crack growth will prevent branching however once the crack velocity approaches a constant value, the stress distribution around the crack tip favours crack propagation in planes inclined at approximately 60° to the normal crack plane resulting in the crack branching into these inclined planes. It was also found experimentally (54) that a critical stress intensity for crack branching exists whose value is two to four times greater than the threshold stress intensity, K_{ISCC}.

No crack branching was observed in any of the WOL specimens.

5.3.4.2 *Specimen Fracture Surfaces*

Examination of both the U-bend and WOL specimen fracture surfaces revealed quite convincingly that the cracks propagated along prior austenite grain boundaries in an intergranular fashion. The higher temperature tempered U-bend specimens were exposed to the corrosive environment for extended periods resulting in the formation of corrosion products on the fracture surface. The presence of corrosion products on the fracture surface can influence the crack tip chemistry and crack propagation kinetics. Corrosion products were also formed on the fracture surfaces of the WOL specimens which cracked, but to a lesser extent. The S545 and S600 U-bend specimens revealed prominent secondary cracks through the thickness of the specimen fracture surface as seen in Figure 4-47. It is unclear why secondary cracks were more noticeable in these higher tempered specimens than in the lower tempered specimens.

Inspection of the WOL fracture surfaces was also conducted to investigate the crack front. It was observed that the crack front was fairly uniform and propagated normal to the notched surfaces of the specimen as seen in Figure B.1-1 in Appendix B. The absence of crack tunnelling and shear lips in all the fractured WOL specimens implies that the specimens were in a state of plane strain.

5.3.4.3 *Crack Morphology*

Crack morphology is dependent on the interaction between the material and the environment. The typical “rock candy” fracture surface synonymous with intergranular stress corrosion cracking (IGSCC) was seen in both U-bend and WOL specimens. It is generally accepted that intergranular crack propagation requires less energy with cracks preferentially following grain boundaries instead of propagating through the grain in a transgranular fashion, which would require a greater energy input. High resolution SEM fractography also revealed crack separation along grain boundaries as seen in Figure 4-69 and Figure 4-73. This type of fracture surface would be indicative of a brittle failure and is fairly common in high strength steels exposed to chloride environments.

5.3.5 SCC Mechanisms

The light micrographs seen in Figure 4-8 showed distinct grain boundary precipitation of varying degrees in the different heat treatment conditions tested. These results alluded to the possibility of chromium depletion in the areas adjacent to the prior austenite grain boundaries (also known as sensitization) as a likely mechanism contributing to the SCC experienced. Sensitization in stainless steels occurs when the precipitation of carbides depletes the matrix of chromium adjacent to the grain boundaries resulting in the depleted zones becoming susceptible to anodic dissolution and having a higher corrosion rate than the matrix. This would then lead to crack initiation and propagation along the grain boundaries. The effect of tensile stress would be to open the crack further exposing the crack tip to the corrosive environment. The fractography results in Figures 4-48 to 4-55 and 4-67 to 4-74 clearly show the crack morphology as intergranular in nature, further enhancing the case for sensitization due to anodic dissolution as the likely SCC mechanism.

The issue of decreasing SCC susceptibility with increasing temper temperature could be explained with the diffusion process. The precipitation of carbides occurs through diffusion which is a temperature controlled process therefore the diffusion rate would be higher at the higher temper temperatures leading to the greater carbide precipitation which was observed. The increasing accumulation of carbide precipitates at the grain boundaries at higher temper temperatures could be seen as favouring the conditions for localised active anodic sites to be created thereby providing the active paths for increased SCC initiation and propagation to occur along the grain boundaries. However, the greater carbide precipitation does not lead to greater SCC susceptibility. The converse is in fact true – higher temper temperatures are less susceptible to SCC. This can again probably be explained with the diffusion rate which, due to being higher at the higher temper temperatures, will ensure that a greater degree of healing will occur at the higher temper temperatures resulting in a more balanced distribution of chromium across the grain boundaries. High oxygen concentrations tend to promote healing and retard pit initiation (39) thereby preventing cracking. Since the test environment was aerated, the required oxygen levels to promote healing would have been available.

For this hypothesis to be proven, it would have had to be demonstrated that chromium depletion was indeed occurring in the areas adjacent to the grain boundaries. The hi-resolution TEM results in section 4.3.6., however, showed no signs of chromium depletion in the areas adjacent to the grain boundaries. The most susceptible material condition (S430) was also analysed using the JEOL Double Cs-corrected Atomic Resolution Microscope to further zoom into the grain boundary area to check for chromium depletion. The results showed no indication of chromium depletion in the areas adjacent to the grain boundaries. It is therefore unclear if a Cr-depletion zone exists or not. There are a number of factors which could have contributed to the Cr-depletion zone not being seen in the EDS results. Firstly, the size of the Cr-depletion zone in martensitic stainless steels is in the region of 10 to 15 nm which is considerably smaller than in austenitic stainless steels (77). Therefore, in order to see any change in Cr content in this zone, the grain boundary should be orientated precisely perpendicular to the beam of the microscope. Any angular orientation would result in a distorted view and could affect the EDS linescan result. The inherent scatter in the point-to-point EDS scan could also have contributed to the minute Cr-depletion zone not being seen. Further work would therefore be required to confirm if a Cr-depletion zone exists or not.

The confirmation of the absence of chromium depletion would imply that another SCC mechanism was prevalent. SCC of high-strength steels has often been attributed to the mechanism of hydrogen embrittlement (HE). The presence of hydrogen, either in the alloy (internal HE), or exposed to the alloy through the environment (external HE), is therefore necessary. In this case, hydrogen is generated in the 3.5% NaCl test solution through the cathodic reaction taking place during the dissociation of water seen in Equation-11. Since the test solution was aerated, the high oxygen levels would favour the cathodic reaction (39). The concentration of hydrogen required to cause HE need not be large and is also influenced by the material's yield strength (43) with HE susceptibility increasing with material yield strength.

The transportation of hydrogen to the corrosion site is facilitated by the size of the hydrogen atom which is small enough to diffuse into interstitial lattice sites in the metal ahead of the crack tip and accumulate at preferred trap sites such as carbides, dislocations, grain boundaries, inclusions and voids. The density of trap sites plays an important role in hydrogen diffusivity. Increasing the density of irreversible trap sites and the binding energy of hydrogen to these traps decreases the occurrence of HE (43). The increased size and quantity of grain boundary carbide precipitates with increasing temper temperature would function as strong hydrogen trap sites, reducing hydrogen diffusivity and decreasing the SCC susceptibility. The presence of reverted austenite in the matrix is also known to act as irreversible trap sites. Tsay et al. (84) have shown that the quantity of irreversible trap sites increased with increasing temper temperature in a PH 13-8 Mo stainless steel. The increase in these irreversible trap sites was directly attributed to the increase in reverted austenite at the higher temper temperatures. This had the effect of retarding the hydrogen diffusivity. Tsay et al. (84) also found that hydrogen permeation was greater at the lower temper temperatures which contained less reverted austenite. At these lower temper temperatures, rapid diffusion of hydrogen to the area of local triaxial stresses ahead of the crack tip increased the susceptibility to HE. This could explain the lower susceptibility of higher tempered specimens of FV520B to SCC in which the quantity of reverted austenite and carbide precipitates was greater. The increased density of irreversible trap sites made these material conditions less susceptible to cracking. The lower temper specimens of FV520B, in which hydrogen permeation is likely to be greater due to less irreversible trap sites being present, was more susceptible to cracking.

The contribution of material strength level to the HE process could possibly be to influence the creation of fresh crack surfaces under sustained loading (85). The specimens heat treated to low temper temperatures thus producing high strength would possess a greater driving force for the creation of new crack surfaces than the low strength high temper temperature specimens. These freshly produced crack surfaces would act as the points of adsorption and entry for hydrogen generated in the environment into the metal matrix leading to embrittlement. High strength low temper temperature specimens would therefore have an increased susceptibility to hydrogen embrittlement than low strength high temper temperature specimens.

Both Schleithoff et al. (18) and Turnbull et al. (10) have attributed the SCC of stainless steel turbine blade materials, X20Cr13, X22CrMoV121 and FV566, PH 13-8 Mo respectively, to hydrogen embrittlement. In both cases, the fracture surfaces exhibited intergranular features consistent with those found in this study. It was also apparent in both cases that material susceptibility decreased with increasing temper temperature as was found for FV520B in this study.

If the confirmation of a Cr-depletion zone is made, SCC due to anodic dissolution and sensitization would be the likely mechanism in FV520B. However, the absence of chromium depletion would imply that hydrogen embrittlement is the dominant SCC mechanism in the different material conditions of FV520B.

6 Conclusions and Recommendations

6.1 Findings and Conclusions

6.1.1. Light microscopy and electron microscopy (SEM and TEM) revealed the presence of Cr-rich (Cr_7C_3 and $Cr_{23}C_6$) precipitates along prior austenite grain boundaries in all six heat treatment conditions tested. The propensity, quantity and size of the Cr-rich precipitates found along the prior austenite grain boundaries increased as the specimen temper temperature increased.

6.1.2. Niobium carbide (NbC) precipitates were observed as rod-like particles orientated at preferred crystallographic planes and dispersed throughout the microstructure. The presence of NbC precipitates thus contributed to the overall high strength levels measured through dispersion strengthening.

6.1.3. X-ray diffraction (XRD) results showed the presence of reverted austenite in the microstructures of the S545 and S600 specimens. The reverted austenite quantities measured were 4.2% in the S545 specimen and 20.8% in the S600 specimen by volume fraction respectively. This indicates that tempering at a temperature above approximately 500°C increases the amount of reverted austenite in the microstructure upon cooling.

6.1.4. Mechanical hardness and tensile tests revealed that an increase in temper temperature above 430°C reduced hardness and tensile strength while increasing ductility. The reduction in hardness and strength is greater when the temper temperature is above 500°C. This correlated well to the measured quantities of reverted austenite which increased in the same temper temperature range. The presence of reverted austenite, therefore, significantly reduces hardness and tensile strength in FV520B.

6.1.5. SCC susceptibility in FV520B was shown to decrease with increasing temper temperature above 430°C in a 3.5% NaCl solution at 90°C. The S430 condition was the most susceptible while the S600 condition showed no failure after 5177 hours and 3629 hours respectively in the test solution. There was a clear correlation between time-to-failure and the 0.2% proof strength of the specimens. The specimens with the higher proof strength failed sooner and failure times increased as the specimen proof strength decreased as observed in previous research on similar materials. The presence of reverted austenite at higher precipitation hardening temperatures thus improved the SCC susceptibility of FV520B. It is thus clear that the high strength at the low PH temperatures makes them more susceptible to SCC.

6.1.6. Crack incubation times were seen to increase with increasing temper temperature indicating an inverse relationship between SCC susceptibility and crack incubation time.

6.1.7. Crack growth rates were seen to decrease with increasing temper temperature indicating a dependence on yield strength.

6.1.8. WOL testing produced cracking in only three material conditions viz. S430, S450 and S470 after 2000 hours in the test environment. The prominence of a plateau velocity in stage II in the S430 and S450 conditions indicated an independence of crack growth rate to stress intensity during most of the crack propagation duration.

6.1.9. Threshold stress intensities (K_{ISCC}) calculated for the S430 and S450 conditions were between 3.8 and 5.3 MPa√m. The low calculated K_{ISCC} values indicated that high yield strengths (greater than 1000 MPa) adversely affect the threshold stress intensities reducing them to low levels.

6.1.10. The crack path was along prior austenite grain boundaries indicating that intergranular stress corrosion cracking (IGSCC) was dominant in all material conditions tested.

6.1.11. Chromium depletion was not evident in the areas adjacent to the prior austenite grain boundaries although this was not conclusively proven. The SCC mechanism would therefore depend on the presence or absence of a Cr-depletion zone. If chromium depletion does occur, the SCC mechanism is likely to be anodic dissolution. If there is no Cr-depletion zone, hydrogen embrittlement would be the dominant SCC mechanism.

6.2 Recommendations for Further Research

6.2.1. Further SCC testing using WOL specimens should be conducted for longer durations exceeding 10 000 hours in order to obtain crack growth and threshold stress intensity results in the higher temper temperature specimens due to their greater immunity to SCC. Fracture toughness tests should also be conducted to be able to better select the applied stress intensities (K_{I0}) for the WOL specimens.

6.2.2. SCC testing in an environment more accurately simulating conditions in the turbine should be conducted to determine material susceptibility. Different heat treatment conditions with variations in both homogenisation and solution treatment temperatures should be investigated to determine the effect of improper heat treatment on SCC.

6.2.3. A study investigating whether a Cr-depletion zone exists should be conducted. Precautions to ensure that the specimen orientation is correct should be taken during the analysis due to the limited size of the Cr-depletion zone on either side of the grain boundaries. Quantitative estimation of the Cr-depletion zone should also be done.

6.2.2. Electrochemcial tests should be conducted to determine the effect of electrochemical potential on the SCC susceptibility of FV520B.

7 References

1. Low-Pressure Steam Turbine Corrosion Mechanisms and Interactions:State of Knowledge 2010. Palo Alto, CA: EPRI; 2010. Report No.: 1020671.

2. Brown BF. Stress-Corrosion Cracking in High Strength Steels and in Titanium and Aluminum Alloys. 1972.

3. Lisagor BW. Environmental Cracking - Stress corrosion. In: Corrosion Tests and Standards Manual. ASTM; 2005. p. 289-301.

4. Hartmann K, Pershad S. Stress Corrosion Cracking of Turbine Blade Steels. South Africa: Eskom; 2005. Report No.: Eskom Internal Report RES/P /04/25227.

5. Clark A. Fatigue Mechamisms in FV520B, A Turbine Blade Steel [dissertation]. United Kingdom: Sheffield Hallam University; 1999.

6. Fan J, Guo X, Wu C, Crupi V, Guglielmino E. Influence of Heat Treatments on Mechanical Behavior of FV520B Steel. Experimental Techniques. 2013.

7. Chu Q, Zhang M, Li J. Failure Analysis of Impeller Made of FV520B Martensitic Precipitated Hardening Stainless Steel. Eng Failure Anal. 2013 12;34:501-10.

8. Firth Vickers Data Handbook. Sheffield: Sheffield Forgemasters Limited Publishing; 1988.

9. Morley JI. FV520(B) STEEL - Resistance to Stress Corrosion. Corrosion Technology. 1964:69.

10. Turnbull A, Zhou S. Comparative Evaluation of Environment Induced Cracking of Conventional and Advanced Steam Turbine Blade Steels. Part 1: Stress Corrosion Cracking. Corros Sci. 2010;52(9):2936-44.

11. Gonzalez-Rodriguez J, Bahena-Martinez G, Salinas-Bravo V. Effect of Heat Treatment on the Stress Corrosion Cracking Behaviour of 403 Stainless Steel in NaCl at 95° C. Mater Lett. 2000;43(4):208-14.

12. Gonzalez-Rodriguez J, Salinas-Bravo V, Martinez-Villafañe A. Hydrogen Embrittlement of Type 410 Stainless Steel in Sodium Chloride, Sodium Sulfate, and Sodium Hydroxide Environments at 90°C. Corrosion. 1997;53(6):499-504.

13. Gonzalez-Rodriguez J, Salinas-Bravo V, Martinez-Villafañe A. Stress Corrosion Cracking of Type 403 Stainless Steel in Sodium Chloride at 95 C Under Different Heat Treatment Conditions. Corrosion. 1999;55(10):991-6.

14. Bloom FK. Stress Corrosion Cracking Of Hardenable Stainless Steels. Corrosion.1955 11(8):39-49.

15. Isfahany AN, Saghafian H, Borhani G. The Effect of Heat Treatment on Mechanical Properties and Corrosion Behavior of AISI420 Martensitic Stainless Steel. J Alloys Compounds. 2011;509(9):3931-6.

16. Doig P, Chastell D, Flewitt P. The Stress Corrosion Susceptibility of a Quenched and Tempered 12 pct CrMoV Martensitic Stainless Steel. Metallurgical Transactions A. 1982;13(5):913-21.

17. Seumangal N. Influence of the Heat Treatment Procedure on the Stress Corrosion Cracking Behaviour of Low Pressure Turbine Blade Steel FV566 [dissertation]. South Africa: University of Cape Town; 2016.

18. Schleitoff K, Schmitz F. Stress Corrosion Cracking Tests on Turbine Blade Material. Corrosion Fatigue of Steam Turbine Blade Materials; Palo Alto, California. EPRI; 1981.

19. Speidel MO. Major Influences on the Growth Rates of Stress Corrosion Cracks in Steam Turbine Rotor and Blade Materials. EPRI Steam Turbine Stress Corrosion Workshop; 1997; Baltimore, USA. United States of America: EPRI; 1997.

20. Honeycombe RWK, Bhadeshia HKDH. Steels: Microstructure and Properties. 2nd Edition ed. Great Britain: Gray Publishing; 1995.

21. Embrittlement of Power Plant Steels. Palo Alto, CA: EPRI; 2013. Report No.: 3002001474.

22. Higgins RA. Engineering Metallurgy, Part 1. 5th Edition ed. Melbourne, Florida: Robert E Kreiger Publishing Company; 1983.

23. Irvine KJ, Llewellyn DT, Pickering FB. Controlled-Transformation Stainless Steels. Journal of The Iron and Steel Institute. July 1959;192:218-38.

24. Brooks CR. Heat Treatment of Ferrous Alloys. United States of America: Hemisphere Publishing Corporation; 1979.

25. Pickering FB. The Metallurgical Evolution of Stainless Steels. In: The Metallurgical Evolution of Stainless Steels: A Discrimative Selection of Outstanding Articles and Papers from the Scientific Literature. United States of America: American Society for Metals; 1979. p. 1-14.

26. Askeland DR. The Science and Engineering of Materials. Third Edition ed. United States of America: PWS Publishing Company; 1994.

27. Ravichandran KS, Vasudevan AK. Fracture Resistance of Structural Alloys. In: ASM Handbook Volume 19, Fatigue And Fracture. United States of America: ASM International; 1996. p. 381-92.

28. Slunder C, Hoenie A, Hall A. Thermal and Mechanical Treatment for Precipitation-Hardening Stainless Steels. NASA SP-5089. NASA Special Publication. 1967;5089.

29. Bhambroo R, Roychowdhury S, Kain V, Raja VS. Effect of Reverted Austenite on Mechanical Properties of Precipitation Hardenable 17-4 Stainless Steel. Materials Science and Engineering: A. 2013;568(0):127-33.

30. Park ES, Yoo DK, Sung JH, Kang CY, Lee JH, Sung JH. Formation of Reversed Austenite during Tempering of 14Cr-7Ni-0.3Nb-0.7Mo-0.03C Super Martensitic Stainless Steel. 2004(6):- 521-525.

31. Schnitzer R, Radis R, Nöhrer M, Schober M, Hochfellner R, Zinner S, et al. Reverted Austenite in PH 13-8 Mo Maraging Steels. Mater Chem Phys. 2010;122(1):138-45.

32. Schnitzer R, Zickler GA, Lach E, Clemens H, Zinner S, Lippmann T, et al. Influence of Reverted Austenite on Static and Dynamic Mechanical Properties of a PH 13-8 Mo Maraging Steel. Materials Science and Engineering: A. 2010;527(7–8):2065-70.

33. International Organisation for Standardization. DIN ISO 8044:1999 Corrosion of Metals and Alloys - Basic Terms and Definitions. Switzerland: International Organisation for Standardization; 1999.

34. Anderson TL. Fracture Mechanics: Fundamentals and Applications. Third Edition ed. United States of America: Taylor & Francis Group; 2005.

35. Williams G, McMurray H. Pitting Corrosion of Steam Turbine Blading Steels: The Influence of Chromium Content, Temperature, and Chloride Ion Concentration. Corrosion. 2006;62(3):231-42.

36. Shimahashi N, Muto I, Sugawara Y, Hara N. Effects of Corrosion and Cracking of Sulfide Inclusions on Pit Initiation in Stainless Steel. J Electrochem Soc. 2014;161(10):C494-500.

37. Turnbull A, Zhou S. Pit to Crack Transition in Stress Corrosion Cracking of a Steam Turbine Disc Steel. Corros Sci. 2004;46(5):1239-64.

38. Speidel MO. Corrosion Fatigue in Fe-Ni-Cr Alloys. NACE. 1977(5):1071-94.

39. ASM International. ASM Handook: Volume 13 Corrosion. United States of America: ASM International; 1987.

40. Lynch S, Raja V, Shoji T. Mechanistic and Fractographic Aspects of Stress-Corrosion Cracking (SCC). Stress Corrosion Cracking: Theory and Practice. 2011:1.

41. Fontana MG. General Theory of Stress Corrosion. Stress Corrosion Cracking in Aircraft Structural Materials; 1967; Turin, Italy. United States of America: AGARD.

42. Uhlig HH. An Evaluation of Stress Corrosion Cracking Mechanisms. Proceedings of Conference on Fundamental Aspects of Stress Corrosion Cracking; 1969; Houston, Texas. United States of America: NACE.

43. Ramamurthy S, Atrens A. Stress Corrosion Cracking of High-Strength Steels. Corr Rev. 2013;31(1):1-31.

44. Thompson RS. The Stress Corrosion Cracking of Corrosion-Abrasion Resistant Development Steels [dissertation]. South Africa: University of Cape Town; 1991.

45. Procter R, Paxton H. The Effect of Prior-Austenite Grain-Size on the Stress-Corrosion Cracking Suscpetibility OF AISI 4340 Steel. 1969.

46. Banerji SK, McMahon CJ, Feng HC. Intergranular Fracture in 4340-type Steels: Effects of Impurities and Hydrogen. Metallurgical Transactions A. 1978;9(2):237-47.

47. Rosario D, Viswanathan R, Wells C, Licina G. Stress Corrosion Cracking of Steam Turbine Rotors. Corrosion. 1998;54(7):531-45.

48. Turnbull A. Current Understanding of Environment-Induced Cracking of Steam Turbine Steels. Corrosion. 2008(5):420.

49. Zhou S, Turnbull A. Steam Turbine Operating Conditions, Chemistry of Condensates, and Environment Assisted Cracking: A Critical Review. National Physical Laboratory; 2002.

50. Proceedings: Workshop on Corrosion of Steam Turbine Blading and Disks in the Phase Transition Zone; 1998; TR-111340. Palo Alto, C: EPRI.

51. Turbine Steam, Chemistry, and Corrosion, Experimental Turbine Tests. Palo, Alto, CA: EPRI; 1997. Report No.: TR-108185.

52. Povarov O, Semenov V, Troitsky A. Generation of Liquid Films and Corrosive Solutions on Blades and Discs of Turbine Stages. Specialist Workshop on Corrosion of Steam Turbine LP Blades and Discs; 1998; Palo, Alto, CA: EPRI.

53. Gilbert W. Steam Purity. EPRI Workshop Proceedings: Low Pressure Steam Turbine Blade Failures; 1980; Michigan, USA. United States of America: EPRI.

54. Carter C. Stress Corrosion Crack Branching in High-Strength Steels. Eng Fract Mech. 1971;3(1):1-13.

55. Clark A, Irwin G. Crack-Propagation Behaviors. Exp Mech. 1966;6(6):321-30.

56. Bezuidenhout M. Private Communication. 2014.

57. Stainless Steel Thermal Properties [Internet]. United Kingdom: University of Manchester; c2011 [updated 2011 Aug 23; cited 2015 Mar 30]. Available from: http://www.mace.manchester.ac.uk/project/research/structures/strucfire/materialInFire/Steel/StainlessSteel/thermalProperties.htm.

58. ASTM International. ASTM E92-82: Standard Test Method for Vickers Hardness of Metallic Materials. ASTM International; 2003.

59. BSI. BS EN 10002-1:2001 Tensile Testing of Metallic Materials. Method of Test at Ambient Temperature. United Kingdom: BSI; 2001.

60. MEE. Handbook of Analytical Methods for Materials. United States of America: Materials Evaluation & Engineering Inc.

61. Cullity BD. Elements of X-ray Diffraction. United States of America: Addison-Westley Publiching Company; 1956.

62. Monecke T, Köhler S, Kleeberg R, Herzig PM, Gemmell JB. Quantitative Phase-Analysis by the Rietveld Method using X-Ray Powder-Diffraction Data: Application to the Study of Alteration Halos Associated with Volcanic-Rock-Hosted Massive Sulfide Deposits. The Canadian Mineralogist. 2001;39(6):1617-33.

63. Energy-Filtered Transmission Electron Microscopy (EFTEM) [Internet]. USA: Gatan,Inc.; 2016 [updated 2016 Jul 12; cited 2016 Jul 12]. Available from: http://www.gatan.com/techniques/eftem.

64. Otten MT. High-Angle Annular Dark-Field Imaging on a TEM/STEM System. J Electron Microsc Tech. 1991;17(2):221-30.

65. Eliaz N, Shachar A, Tal B, Eliezer D. Characteristics of Hydrogen Embrittlement, Stress Corrosion Cracking and Tempered Martensite Embrittlement in High-Strength Steels. Eng Failure Anal. 2002 4;9(2):167-84.

66. Wilde BE. - Mechanism of Cracking of High Strength Martensltic Stainless Steels in Sodium Chloride Solutions. - Corrosion. 1971(8):326-33.

67. Speidel MO. Stress Corrosion Cracking of Stainless Steels in NaCl Solutions. Metallurgical transactions A. 1981;12(5):779-89.

68. Carter CS, Farwick DG, Ross AM, Uchida JM. Stress Corrosion Properties of High Strength Precipitation Hardening Stainless Steels. Corrosion. 1971;27(5):190-7.

69. ASTM International. ASTM G30-97: Standard Practice for Making and Using U-Bend Stress-Corrosion Test Specimens. United States of America: ASTM International; 2009.

70. ASTM International. ASTM E1681-03 - Standard Test Method for Determining Threshold Stress Intensity Factor for Environment-Assisted Cracking of Metallic Materials. ASTM International; 2008.

71. ASTM International. ASTM E647-13a - Standard Test Method for Measurement of Fatigue Crack Growth Rates. ASTM International; 2013.

72. Wei RP, Novak SR. Interlaboratory Evaluation of KISCC and da/dt Measurement Procedures for High-Strength Steels. Journal of Testing and Evaluation. 1987;15:38-75.

73. Ma XP, Wang LJ, Liu CM, Subramanian SV. Role of Nb in Low Interstitial 13Cr Super Martensitic Stainless Steel. Materials Science and Engineering: A. 2011;528(22–23):6812-8.

74. Garcí C, Caballero F, Capdevila C, Alvarez L. Application of Dilatometric Analysis to the Study of Solid–Solid Phase Transformations in Steels. Mater Charact. 2002;48(1):101-11.

75. Kumar VA, Gupta R, Karthikeyan M, Prasad KN, Sinha P, Rao MN. Processing and Characterization of Thin Sheets of 17-4PH Stainless Steel for Aerospace Application. International Conference on Advanced Materials and Composites (ICAMC-2007); 2007.

76. Sahlaoui H, Makhlouf K, Sidhom H, Philibert J. Effects of Ageing Conditions on the Precipitates Evolution, Chromium Depletion and Intergranular Corrosion Susceptibility of AISI 316L: Experimental and Modeling Results. Materials Science and Engineering: A. 2004;372(1):98-108.

77. Nakamichi H, Sato K, Miyata Y, Kimura M, Masamura K. Quantitative Analysis of Cr-Depleted Zone Morphology in Low Carbon Martensitic Stainless Steel using FE-(S) TEM. Corros Sci. 2008;50(2):309-15.

78. Steigerwald EA. Engineering Aspects of Stress Corrosion Failure in Martensitic Steels. Stress Corrosion Cracking in Aircraft Structural Materials; Turin, Italy. AGARD; 1967.

79. Gooch T. Stress Corrosion Cracking of Welded Joints in High Strength Steels. Welding journal. 1974;53(7):287.

80. Nibur KA. Measurement and Interpretation of Threshold Stress Intensity Factors for Steels in High-Pressure Hydrogen Gas. Sandia National Laboratories; 2010. Report No.: SAND2010-8036C.

81. Carter CS. Effect of Prestressing on the Stress-Corrosion Resistance of Two High-Strength Steels. Metallurgical and Materials Transactions B. 1972;3(2):588-90.

82. Hanisch A, Burck L. Effects of Overloads on the Incubation Time for Stress Corrosion Cracking of 7075 Aluminum. Corrosion. 1982;38(6):330-5.

83. Freedman AH. Development of an Accelerated Stress-Corrosion Test for Ferrous and Nickel Alloys. NASA; 1968. Report No.: NOR 68-58.

84. Tsay L, Chi M, Chen H, Chen C. Investigation of Hydrogen Sulfide Stress Corrosion Cracking of PH 13-8 Mo Stainless Steel. Materials Science and Engineering: A. 2006;416(1):155-60.

85. Wei RP, Klier K, Simmons GW, Chou YT. Fracture Mechanics and Surface Chemistry Investigations of Environment-Assisted Crack Growth. In: Gibala R, Hehemann RF, editors. Hydrogen Embrittlement and Stress Corrosion Cracking. United States of America: American Society for Metals; 1984. p. 103-33.

Appendix A TEM Results of S500 specimen

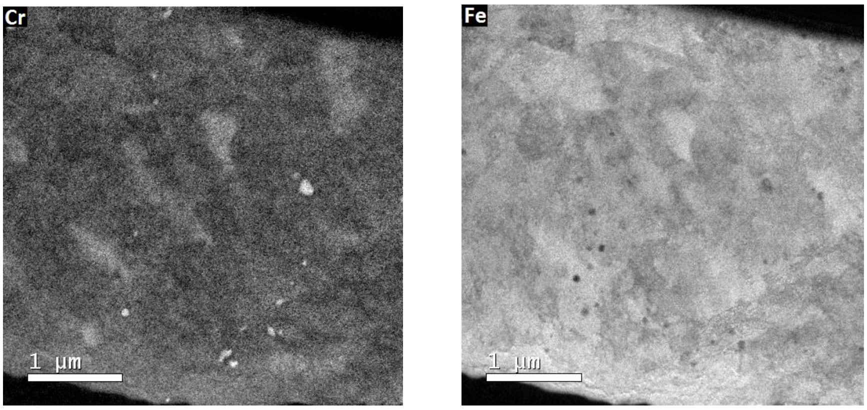

Figure A-1: EFTEM elemental maps showing location of Cr-rich precipitates for S500 specimen.

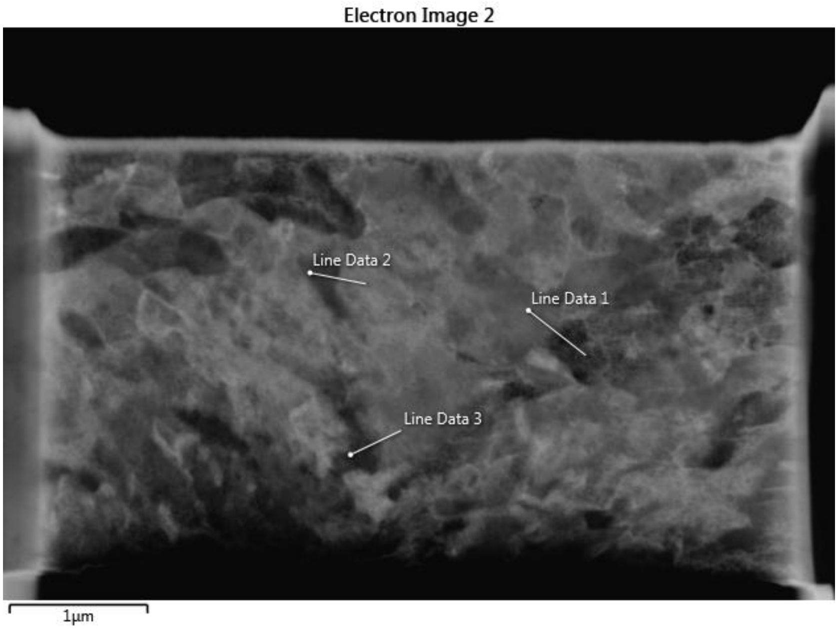

	Line Data 1	Line Data 2	Line Data 3
Cr	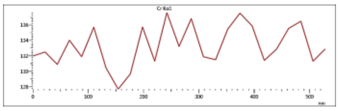	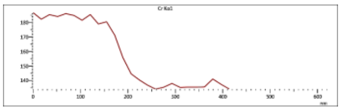	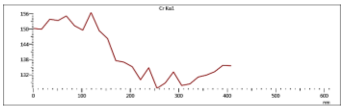
Fe	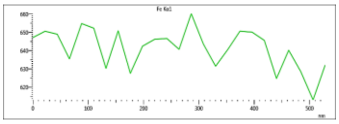	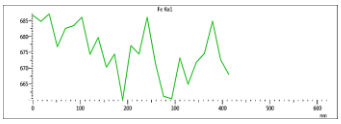	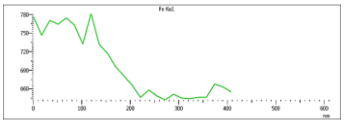
Ni	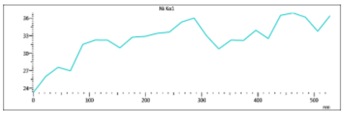	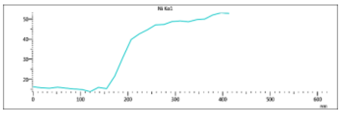	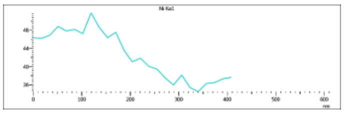

Figure A-2: HAADF-STEM image and EDS results for S500 specimen.

Appendix B Supplementary WOL Test Results

B.1: WOL Fracture Surfaces and Crack Length Measurements

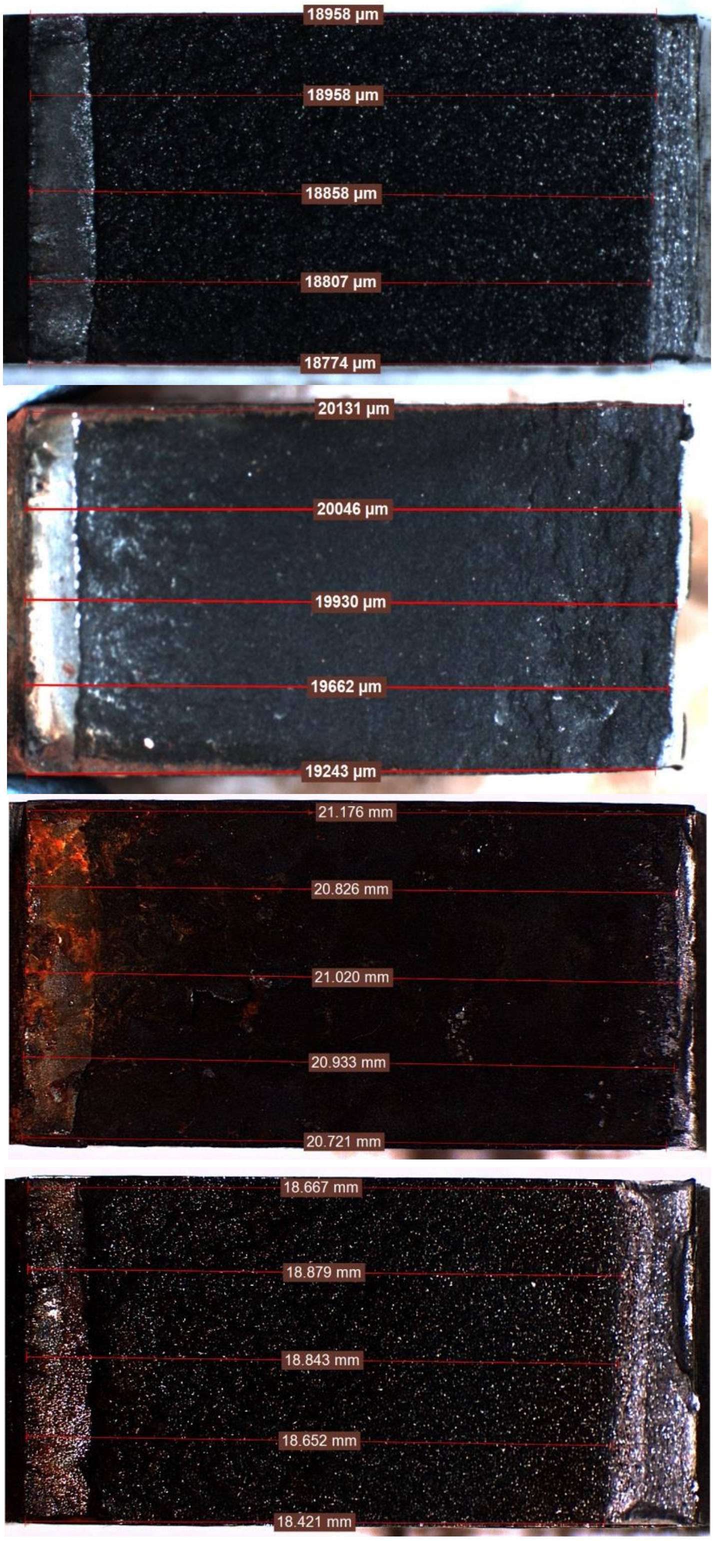

Figure B.1-1: WOL specimens' crack length measurements.

Top to bottom: S430 (Batch 2), S450 (Batch 2), S430 (Modified), S450 (Modified).

B.2: WOL Fracture Surfaces of Modified S430 and S450 Specimens

S430 Modified specimen

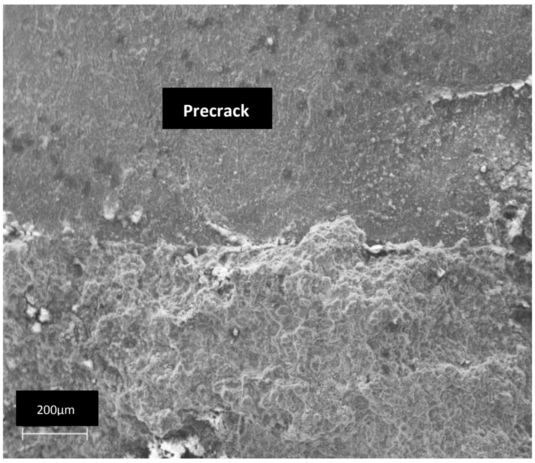

Figure B.2-1: S430 Modified WOL specimen showing start of SCC from precrack.

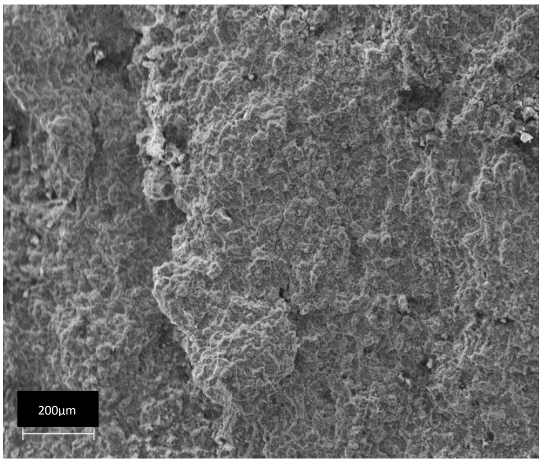

Figure B.2-2: S430 Modified WOL specimen showing intergranular SCC on fracture surface.

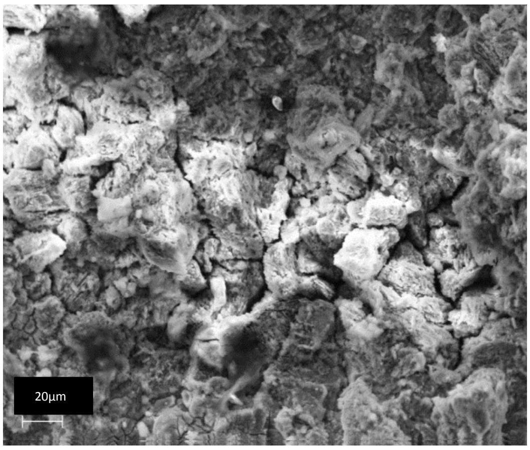

Figure B.2-3: S430 Modified WOL specimen showing separation along grain boundaries.

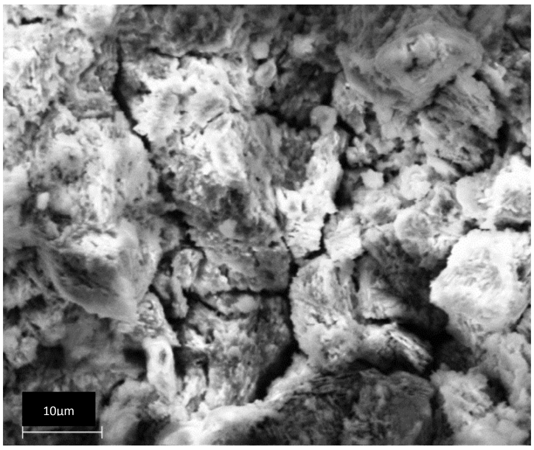

Figure B.2-4: S430 Modified WOL specimen showing intergranular SCC in high magnification.

S450 Modified specimen

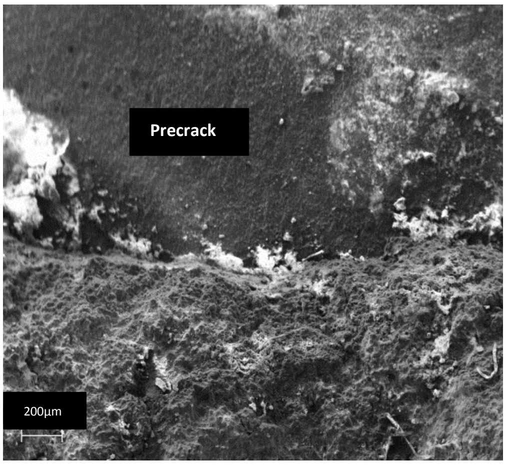

Figure B.2-5: S450 Modified WOL specimen showing start of SCC from precrack.

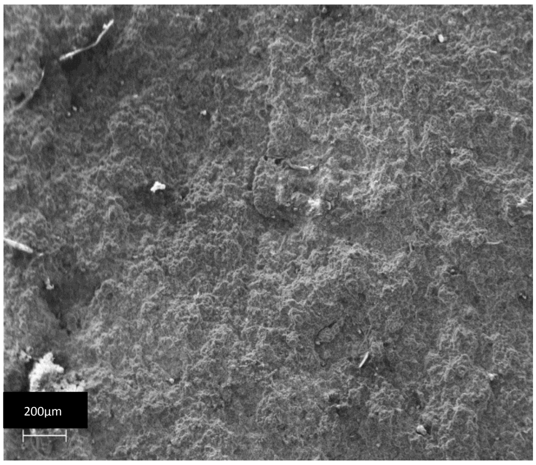

Figure B.2-6: S450 Modified WOL specimen showing intergranular SCC.

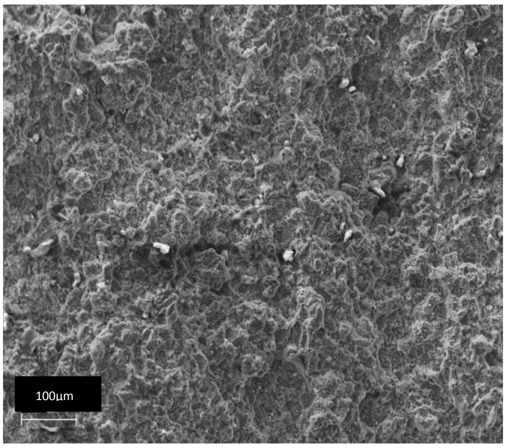

Figure B.2-7: S450 Modified WOL specimen showing SCC propagation along grain boundaries.

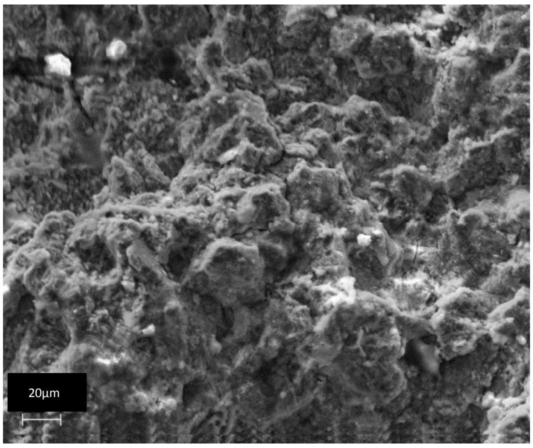

Figure B.2-8: S430 Modified WOL specimen showing intergranular SCC in high magnification.

B.2: WOL Specimen Applied CMOD measurements

	Applied CMOD measurements (mm)		
Specimen	**Batch 1**	**Batch 2**	**Modified**
S430	0.239	0.206	0.244
S450	0.248	0.257	0.258
S470	0.267	0.255	0.275
S500	0.47		0.324
S545	0.516		0.391
S600	0.541		0.424

Table B.2: WOL specimen CMOD measurements.

EBE Faculty: Assessment of Ethics in Research Projects

Any person planning to undertake research in the Faculty of Engineering and the Built Environment at the University of Cape Town is required to complete this form before collecting or analysing data. When completed it should be submitted to the supervisor (where applicable) and from there to the Head of Department. If any of the questions below have been answered YES, and the applicant is NOT a fourth year student, the Head should forward this form for approval by the Faculty EIR committee: submit to Ms Zulpha Geyer (Zulpha.Geyer@uct.ac.za; Chem Eng Building, Ph 021 650 4791). Students must include a copy of the completed form with the thesis when it is submitted for examination.

Name of Principal Researcher/Student: LEE NAICKER Department: CME

If a Student: Degree: MSc Eng (Materials) Supervisor: Prof. R. Knutsen

If a Research Contract indicate source of funding/sponsorship:

Research Project Title: Influence of heat treatment on SCC properties of LP turbine blade steel - FV520B

Overview of ethics issues in your research project:

Question 1: Is there a possibility that your research could cause harm to a third party (i.e. a person not involved in your project)?	YES	[✓ NO]
Question 2: Is your research making use of human subjects as sources of data? If your answer is YES, please complete Addendum 2.	YES	[✓ NO]
Question 3: Does your research involve the participation of or provision of services to communities? If your answer is YES, please complete Addendum 3.	YES	[✓ NO]
Question 4: If your research is sponsored, is there any potential for conflicts of interest? If your answer is YES, please complete Addendum 4.	YES	[✓ NO]

If you have answered YES to any of the above questions, please append a copy of your research proposal, as well as any interview schedules or questionnaires (Addendum 1) and please complete further addenda as appropriate.

I hereby undertake to carry out my research in such a way that

- there is no apparent legal objection to the nature or the method of research; and
- the research will not compromise staff or students or the other responsibilities of the University;
- the stated objective will be achieved, and the findings will have a high degree of validity;
- limitations and alternative interpretations will be considered;
- the findings could be subject to peer review and publicly available; and
- I will comply with the conventions of copyright and avoid any practice that would constitute plagiarism.

Signed by:

	Full name and signature	Date
Principal Researcher/Student: LEE NAICKER	Signed by candidate	23/01/2015

This application is approved by:

Supervisor (if applicable):	Signed by candidate	30/01/2015
HOD (or delegated nominee) Final authority for all assessments with NO to all questions and for all undergraduate research.	Signed by candidate	30/01/2015
Chair: Faculty EIR Committee For applicants other than undergraduate students who have answered YES to any of the above questions.		